

Fall 2014

Piston / Cylinder Interface Of Axial Piston Machines – Effect Of Piston Micro-Surface Shaping

Ashley M. Wondergem

Follow this and additional works at: https://docs.lib.purdue.edu/open_access_theses



Part of the [Mechanical Engineering Commons](#)

Recommended Citation

Wondergem, Ashley M., "Piston / Cylinder Interface Of Axial Piston Machines – Effect Of Piston Micro-Surface Shaping" (2014). *Open Access Theses*. 395.

https://docs.lib.purdue.edu/open_access_theses/395

This document has been made available through Purdue e-Pubs, a service of the Purdue University Libraries. Please contact epubs@purdue.edu for additional information.

**PURDUE UNIVERSITY
GRADUATE SCHOOL
Thesis/Dissertation Acceptance**

This is to certify that the thesis/dissertation prepared

By Ashley Wondergem

Entitled

Piston / Cylinder Interface of Axial Piston Machines - Effect of Piston Micro-Surface Shaping

For the degree of Master of Science in Mechanical Engineering

Is approved by the final examining committee:

Monika Ivantysynova

Andrea Vacca

Farshid Sadeghi

To the best of my knowledge and as understood by the student in the Thesis/Dissertation Agreement, Publication Delay, and Certification/Disclaimer (Graduate School Form 32), this thesis/dissertation adheres to the provisions of Purdue University's "Policy on Integrity in Research" and the use of copyrighted material.

Monika Ivantysynova

Approved by Major Professor(s): _____

Approved by: Ganesh Subbarayan

12/08/2014

Head of the Department Graduate Program

Date

PISTON / CYLINDER INTERFACE OF AXIAL PISTON MACHINES – EFFECT OF
PISTON MICRO-SURFACE SHAPING

A Thesis
Submitted to the Faculty
of
Purdue University
by
Ashley Wondergem

In Partial Fulfillment of the
Requirements for the Degree
of
Master of Science in Mechanical Engineering

December 2014
Purdue University
West Lafayette, Indiana

To my family

ACKNOWLEDGEMENTS

First, I would like to thank my advisor Dr. Monika Ivantysynova for the chance to pursue my Master's degree and further my knowledge in fluid power here at the Maha Fluid Power Research Center. Under your guidance I was able to challenge myself and achieve goals that may have not been possible elsewhere. I thank you greatly for that.

Next, I would like to thank my family and friends. Without their unconditional support, love, and encouragement to continue on I would never have made it as far as I have and none of this would be possible.

I would also like to thank all of my colleagues which have become my friends throughout my two and a half years here. A special thank you to Dan Mizell as he has mentored me and taught me so much about the piston/cylinder interface. I also send many thanks to Andrew Schenk as he has helped me many times with my multiple computer problems. And to my many lifelong friends that I have made here at Maha that make my work days that much more enjoyable – Enrique, Jule, Rene, Matteo, Nils, Taeho, Lizhi, Paul, and many more. I will never forget the experiences and memories made.

Of course, I would also like to thank the staff here at Maha. Connie, thank you for all the help that you have given me when it comes to traveling. To Anthony for all the help in the lab, including the work with the steady state test rig. Especially to Susan who has helped me so much in both my professional career along with being comforting in some difficult personal times, you are such a beautiful and caring person.

TABLE OF CONTENTS

	Page
LIST OF TABLES	vii
NOMENCLATURE	xviii
LIST OF ABBREVIATIONS	xxi
ABSTRACT	xxii
CHAPTER 1. INTRODUCTION.....	1
1.1 Main Tribological Interfaces	1
1.2 State of the Art	2
1.3 Aims and Goals of Work.....	5
CHAPTER 2. THE PISTON / CYLINDER INTERFACE.....	7
2.1 Introduction to Axial Piston Machines.....	7
2.2 Axial Piston Machine Kinematics.....	8
2.3 Function of the Piston / Cylinder Interface	9
2.4 Dynamic Loading Conditions of the Piston / Cylinder Interface.....	10
2.5 Piston / Cylinder Fluid Film Geometry.....	12
CHAPTER 3. NUMERICAL MODEL.....	15
3.1 Overview of the Numerical Model.....	15
3.1.1 Reynolds Equation	15
3.1.2 Energy Equation	16
3.1.3 Energy Dissipation and Leakage.....	17
3.2 Fluid Structure Thermal Interaction Model	18
CHAPTER 4. BASELINE SIMULATION AND MEASUREMENTS	21
4.1 Steady State Measurements.....	21
4.1.1 Pumping Mode	24

	Page
4.1.2	Motoring Mode27
4.2	Piston/Cylinder Surface Wear Measurements.....29
4.3	Baseline Simulation.....32
4.3.1	Boundary conditions32
4.3.1.1	Pressure Boundary Conditions 33
4.3.1.2	Pressure Profiles..... 34
4.3.1.3	Thermal Boundary Conditions..... 39
4.3.2	Simulation Baseline Results.....40
4.4	Code Verification56
4.4.1	Tribo Test Rig56
4.4.2	Input Parameters.....58
4.4.3	Comparison of Simulation and Measurement Results60
CHAPTER 5.	NOVEL PISTON DESIGNS 63
5.1	Sinusoidal Wave Surface Profile (Sine Wave)63
5.2	Flat Sinusoidal Wave Surface Profile (Flat)64
5.3	Barrel Surface Profile (Barrel).....65
5.4	Sinusoidal Waved Barrel Surface Profile (Waved Barrel).....66
5.5	Circumferential Sinusoidal Wave Surface Profile68
5.5.1	In Combination with Flat Sinusoidal Wave Surface Profile68
5.5.2	In Combination with Cylindrical Surface Profile69
CHAPTER 6.	PISTON MICRO-SURFACE SHAPING DESIGN
	PARAMETER STUDY..... 71
6.1	Sinusoidal Wave Piston Surface Profile Design Parameters Study71
6.1.1	Vary Amplitude.....78
6.1.2	Vary Number of Waves.....80
6.2	Flat Sinusoidal Wave Piston Surface Profile Design Parameters Study.....82
6.2.1	Vary Amplitude at Ends.....84
6.3	Barrel Piston Surface Profile Design Parameters Study86

	Page
6.3.1 Vary Radius.....	92
6.3.2 Vary Apex Location.....	95
CHAPTER 7. INVESTIGATION OF PISTON MICRO-SURFACE SHAPING.....	98
7.1 Pumping, Full Displacement.....	100
7.2 Pumping, Partial Displacement.....	108
7.3 Motoring, Full Displacement.....	111
7.4 Conclusion.....	114
CHAPTER 8. CONCLUSIONS.....	115
LIST OF REFERENCES.....	117
APPENDICES	
Appendix A: Material Properties.....	120
Appendix B: Baseline Measurement Results.....	121
LIST OF PUBLICATIONS.....	124

LIST OF TABLES

Table	Page
4.1. ISO measurement accuracy class B.	22
4.2. Steady-state measurement data acquisition.	23
4.3. Steady-state measurement sensors.	23
4.4. Baseline pumping mode test procedure.	25
4.5. Baseline pumping mode measured temperature results; common operating conditions.	26
4.6. Baseline pumping mode measured temperature results; high pressure operating conditions.	26
4.7. Baseline motoring mode test procedure.	28
4.8. Baseline motoring mode measured results.	28
4.9. Profilometer specifications.	29
4.10. Piston/cylinder interface boundary conditions defined.	39
4.11. Tribo measured and simulated operating conditions.	58
6.1. Design parameter study operating conditions.	71
6.2. Complete combination list of design parameters for sine wave design parameter study.	72
6.3. Complete combination list of design parameters for barrel design study.	87
7.1. Investigation of piston micro-surface shaping operating conditions.	98
7.2. Investigation of piston micro-surface shaping design parameters.	99
A.A1. Material properties.	120
A.B1. Baseline pumping mode complete measured results –common operating conditions.	143

Table	Page
A.B2. Baseline pumping mode complete measured results – high pressure operating conditions.....	144
A.B3. Baseline motoring mode complete measured results.....	145

LIST OF FIGURES

Figure	Page
1.1. Axial piston machine.	2
1.2. Half barrel like piston surface shape (Lassar, 2003).....	5
1.3. Sine wave piston surface shape (Garrett, 2009).....	5
2.1. Axial piston machine and reference system (Pelosi, 2012).	7
2.2. Piston/Cylinder showing DC pressure change.....	9
2.3. Forces acting on the piston/cylinder interface.	10
2.4. Eccentric position of the piston in the cylinder bore (Pelosi, 2012).....	13
2.5. Unwrapped fluid film geometry (Pelosi, 2012).	14
3.1. Fluid film geometry (Pelosi, 2012).....	16
3.2. Fluid structure thermal interaction model (Pelosi, 2012).	19
4.1. Steady-state measurement test rig.....	22
4.2. Baseline pumping mode test set up.....	24
4.3. Baseline motoring mode test set up.	27
4.4. Profilometer.	29
4.5. Piston wear profile measurement procedure.....	30
4.6. Bushing wear profile measurement procedure.	30
4.7. Piston/bushing wear profiles.....	31
4.8. Piston/cylinder interface pressure boundary conditions to define IMs.....	33
4.9. Baseline simulated instantaneous displacement chamber pressure for operating condition 1; pumping, 1000 rpm, 100 bar, 100%.	34
4.10. Baseline simulated instantaneous displacement chamber pressure for operating condition 2; pumping, 1000 rpm, 300 bar, 100%.	34
4.11. Baseline simulated instantaneous displacement chamber pressure for operating condition 3; pumping, 2000 rpm, 100 bar, 100%.	35

Figure	Page
4.12. Baseline simulated instantaneous displacement chamber pressure for operating condition 4; pumping, 2000 rpm, 300 bar, 100%.	35
4.13. Baseline simulated instantaneous displacement chamber pressure for operating condition 5; pumping, 1000 rpm, 100 bar, 20%.	35
4.14. Baseline simulated instantaneous displacement chamber pressure for operating condition 7; pumping, 2000 rpm, 100 bar, 20%.	36
4.15. Baseline simulated instantaneous displacement chamber pressure for operating condition 8; pumping, 2000 rpm, 300 bar, 20%.	36
4.16. Baseline simulated instantaneous displacement chamber pressure for operating condition 9; pumping, 1000 rpm, 400 bar, 100%.	36
4.17. Baseline simulated instantaneous displacement chamber pressure for operating condition 10; pumping, 2000 rpm, 400 bar, 100%.	37
4.18. Baseline simulated instantaneous displacement chamber pressure for operating condition 11; pumping, 2800 rpm, 400 bar, 100%.	37
4.19. Baseline simulated instantaneous displacement chamber pressure for operating condition 12; motoring, 1000 rpm, 100 bar, 100%.	37
4.20. Baseline simulated instantaneous displacement chamber pressure for operating condition 13; motoring, 1000 rpm, 225 bar, 100%.	38
4.21. Baseline simulated instantaneous displacement chamber pressure for operating condition 14; motoring, 2000 rpm, 100 bar, 100%.	38
4.22. Baseline simulated instantaneous displacement chamber pressure for operating condition 15; motoring, 2000 rpm, 225 bar, 100%.	38
4.23. Piston/cylinder interface thermal boundaries conditions.	40
4.24. Measured wear profile of a used piston and cylinder.	40
4.25. Baseline energy dissipation; piston/cylinder interface.	41
4.26. Baseline leakage; piston/cylinder interface.	42
4.27. Baseline multi-plot, operating condition 3; 2000 rpm, 100 bar, 100%.	43
4.28. Baseline multi-plot, operating condition 4; 2000 rpm, 300 bar, 100%.	44
4.29. Baseline mulitplot, operating condition 8; 2000 rpm, 300 bar, 20%.	45

Figure	Page
4.30. Baseline mulitplot, operating condition 11; 2800 rpm, 400 bar, 100%.....	46
4.31. Baseline multi-plot, operating condition 15; motoring, 2000 rpm, 225 bar, 100%.....	47
4.32. Baseline piston axial friction, operating condition 3; 2000 rpm, 100 bar, 100%.....	48
4.33. Baseline piston axial friction, operating condition 4; 2000 rpm, 300 bar, 100%.....	48
4.34. Baseline piston axial friction, operating condition 8; 2000 rpm, 300 bar, 20%.....	49
4.35. Baseline piston axial friction, operating condition 11; 2800 rpm, 400 bar, 100%.....	49
4.36. Baseline piston axial friction, operating condition 15; motoring, 2000 rpm, 225 bar, 100%.....	50
4.37. Baseline piston/cylinder deformation, operating condition 3; 2000 rpm, 100 bar, 100%.....	51
4.38. Baseline piston/cylinder deformation, operating condition 4; 2000 rpm, 300 bar, 100%.....	51
4.39. Baseline piston/cylinder deformation, operating condition 8; 2000 rpm, 300 bar, 20%.....	52
4.40. Baseline piston/cylinder deformation, operating condition 11; 2800 rpm, 400 bar, 100%.....	52
4.41. Baseline piston/cylinder deformation, operating condition 15; motoring, 2000 rpm, 225 bar, 100%.....	53
4.42. Inclination angle description.....	53
4.43. Baseline inclination angle, operating condition 3; 2000 rpm, 100 bar, 100%.....	54
4.44. Baseline inclination angle, operating condition 4; 2000 rpm, 300 bar, 100%.....	54
4.45. Baseline inclination angle, operating condition 8; 2000 rpm, 300 bar, 20%.....	55
4.46. Baseline inclination angle, operating condition 11; 2800 rpm, 400 bar, 100%.....	55

Figure	Page
4.47. Baseline inclination angle, operating condition 15; motoring, 2000 rpm, 225 bar, 100%.	56
4.48. The tribo test rig	57
4.49. The tribo test rig pump assembly	57
4.50. Standard surface wear profile of the tribo piston and cylinder.	58
4.51. Tribo test rig piston and cylinder boundary conditions.	59
4.52. Tribo test rig measured instantaneous displacement chamber pressure for operating condition 1; 800 rpm, 60 bar.	59
4.53. Tribo test rig measured instantaneous displacement chamber pressure for operating condition 2; 800 rpm, 100 bar.	60
4.54. Tribo test rig measured instantaneous displacement chamber pressure for operating condition 3; 800 rpm, 130 bar.	60
4.55. Axial friction force comparison for operating condition 1; 800 rpm, 60 bar.	61
4.56. Axial friction force comparison for operating condition 2; 800 rpm, 100 bar.	61
4.57. Axial friction force comparison for operating condition 3; 800 rpm, bar.	62
5.1. Sinusoidal wave piston surface profile.	63
5.2. Flat sinusoidal wave piston surface profile.	64
5.3. Barrel piston surface profile.	65
5.4. Sinusoidal wave barrel piston surface profile.	67
5.5. Circumferential sinusoidal wave in combination with the flat sinusoidal wave piston surface profile.	68
5.6. Circumferential sinusoidal wave in combination with the cylindrical piston surface profile.	70
6.1. Varying amplitude of the sine wave piston surface profile.	72
6.2. Varying number of waves of the sine wave piston surface profile.	72
6.3. Decrease in energy dissipation due to varying the design parameters of the sine wave piston surface profile; operating condition 1 - 1000 rpm, 100 bar, 100%.	73

Figure	Page
6.4. Decrease in energy dissipation due to the design parameters of the sine wave piston surface profile; operating condition 2 - 1000 rpm, 300 bar, 100%.....	74
6.5. Decrease in energy dissipation due to varying the design parameters of the sine wave piston surface profile; operating condition 3 - 2000 rpm 100 bar, 100%.	74
6.6. Decrease in energy dissipation due to varying the design parameters of the sine wave piston surface profile; operating condition 4 - 2000 rpm, 300 bar, 100%.	75
6.7. Decrease in leakage due to varying the design parameters of the sinusoidal wave piston surface profile; operating condition 1 - 1000 rpm, 100 bar, 100%.....	76
6.8. Decrease in leakage due to the design parameters of the sinusoidal wave piston surface profile; operating condition 2 - 1000 rpm, 300 bar, 100%.....	76
6.9. Decrease in leakage due to varying the design parameters of the sinusoidal wave piston surface profile; operating condition 3 - 2000 rpm, 100 bar, 100%.....	77
6.10. Decrease in leakage due to varying the design parameters of the sinusoidal wave piston surface profile; operating condition 4 - 2000 rpm, 300 bar, 100%.....	77
6.11. Varying amplitude of the sine wave piston surface profile mulitplots, operating condition 4; 2000 rpm, 300 bar, 100%.	78
6.12. Varying amplitude of the sine wave piston surface profile piston axial friction forces, operating condition 4; 2000 rpm, 300 bar, 100%.....	79
6.13. Varying amplitude of the sine wave piston surface profile correction forces normalized to external force, operating condition 4; 2000 rpm, 300 bar, 100%	79
6.14. Varying amplitude of the sine wave piston surface profile inclination angles, operating condition 4; 2000 rpm, 300 bar, 100%.	80
6.15. Varying the number of waves of the sine wave piston surface profile mulitplots, operating condition 4; 2000 rpm, 300 bar, 100%.	81

Figure	Page
6.16. Varying the number of waves of the sine wave piston surface profile piston axial friction forces, operating condition 4; 2000 rpm, 300 bar, 100%.	81
6.17. Varying the number of waves of the sine wave piston surface profile correction forces normalized to external force, operating condition 4; 2000 rpm, 300 bar, 100%.....	82
6.18. Varying the number of waves of the sine wave piston surface profile inclination angles, operating condition 4; 2000 rpm, 300 bar, 100%.	82
6.19. Varying end amplitude of the flat sinusoidal wave piston surface profile	83
6.20. Decrease in energy dissipation due to varying the design parameters of the flat piston surface profile; (operating condition 1-4).	83
6.21. Decrease in leakage due to varying the design parameters of the flat piston surface profile; (operating condition 1-4).	84
6.22. Varying the amplitude at the ends of the flat piston surface profile mulitplots, operating condition 4; 2000 rpm, 300 bar, 100%.	85
6.23. Varying the amplitude at the ends of the flat piston surface profile piston axial friction forces, operating condition 4; 2000 rpm, 300 bar, 100%.	85
6.24. Varying the amplitude at the ends of the flat piston surface profile correction forces normalized to external force, operating condition 4; 2000 rpm, 300 bar, 100%	85
6.25. Varying the amplitude at the ends of the flat piston surface profile inclination angles, operating condition 4; 2000 rpm, 300 bar, 100%.	85
6.26. Varying radii of the barrel piston surface profile.....	86
6.27. Varying apex location of the barrel piston surface profile.	87
6.28. Decrease in energy dissipation due to varying the design parameters of the barrel piston surface profile; operating condition 1 - 1000 rpm, 100 bar, 100%	88
6.29. Decrease in energy dissipation due to the design parameters of the barrel piston surface profile; operating condition 2 - 1000 rpm, 300 bar, 100%.	88

Figure	Page
6.30. Decrease in energy dissipation due to varying the design parameters of the barrel piston surface profile; operating condition 3 - 2000 rpm, 100 bar, 100%	89
6.31. Decrease in energy dissipation due to varying the design parameters of the barrel piston surface profile; operating condition 4 - 2000 rpm, 300 bar, 100%	89
6.32. Decrease in leakage due to varying the design parameters of the barrel piston surface profile; operating condition 1 - 1000 rpm, 100 bar, 100%.	90
6.33. Decrease in leakage due to the design parameters of the barrel piston surface profile; operating condition 2 - 1000 rpm, 300 bar, 100%.	91
6.34. Decrease in leakage due to varying the design parameters of the barrel piston surface profile; operating condition 3 - 2000 rpm, 100 bar, 100%.	91
6.35. Decrease in leakage due to varying the design parameters of the barrel piston surface profile; operating condition 4 - 2000 rpm, 300 bar, 100%.	92
6.36. Varying radii of the barrel piston surface profile mulitplots, operating condition 4; 2000 rpm, 300 bar, 100%.	93
6.37. Varying radii of the barrel piston surface profile piston axial friction forces, operating condition 4; 2000 rpm, 300 bar, 100%.	93
6.38. Varying radii of the barrel piston surface profile correction forces normalized to external force, operating condition 4; 2000 rpm, 300 bar, 100%	94
6.39. Varying radii of the barrel piston surface profile inclination angles, operating condition 4; 2000 rpm, 300 bar, 100%.	94
6.40. Varying apex location of the barrel piston surface profile mulitplots, operating condition 4; 2000 rpm, 300 bar, 100%.	95
6.41. Varying apex location of the barrel piston surface profile piston axial friction forces, operating condition 4; 2000 rpm, 300 bar, 100%.	96

Figure	Page
6.42. Varying apex location of the barrel piston surface profile correction forces normalized to external force, operating condition 4; 2000 rpm, 300 bar, 100%.	96
6.43. Varying apex location of the barrel piston surface profile inclination angles, operating condition 4; 2000 rpm, 300 bar, 100%.	97
7.1. Decrease in energy dissipation due to micro-surface shaping of the piston; pumping, full displacement (operating conditions 1-4, 9-11).....	100
7.2. Decrease in leakage due to micro-surface shaping of the piston; pumping, full displacement (operating conditions 1-4, 9-11).....	101
7.3. Flat vs. baseline piston axial friction, operating condition 3; pumping, 2000 rpm, 100 bar, 100%......	102
7.4. Flat vs. baseline deformations, operating condition 3; pumping, 2000 rpm, 100 bar, 100%.	103
7.5. Flat vs. baseline piston axial friction, operating condition 1; pumping, 1000 rpm, 100 bar, 100%......	103
7.6. Flat vs. baseline deformations, operating condition 1; pumping, 1000 rpm, 100 bar, 100%.	104
7.7. Barrel vs. baseline piston axial friction, operating condition 1; pumping, 1000 rpm, 100 bar, 100%......	104
7.8. Barrel vs. baseline deformations, operating condition 1; pumping, 1000 rpm, 100 bar, 100%.	105
7.9. Barrel vs. baseline piston axial friction, operating condition 11; pumping, 2800 rpm, 400 bar, 100%......	105
7.10. Barrel vs. baseline deformations, operating condition 11; pumping, 2800 rpm, 400 bar, 100%......	106
7.11. Waved barrel vs. circ sine wave piston axial friction, operating condition 11; pumping, 2800 rpm, 400 bar, 100%.	106
7.12. Waved barrel vs. circ sine wave deformations, operating condition 11; pumping, 2800 rpm, 400 bar, 100%.	107

Figure	Page
7.13. Waved barrel vs. barrel piston axial friction, operating condition 1; pumping, 1000 rpm, 100 bar, 100%.	107
7.14. Waved barrel vs. barrel vs. corrections, operating condition 11; pumping, 2800 rpm, 400 bar, 100%.....	108
7.15. Decrease in energy dissipation due to micro-surface shaping of the piston; pumping, partial displacement (operating conditions 5-8).	109
7.16. Decrease in leakage due to micro-surface shaping of the piston; pumping, partial displacement (operating conditions 5-8).	109
7.17. Baseline vs. barrel vs. flat piston axial friction, operating condition 8; pumping, 1000 rpm, 300 bar, 20%.	110
7.18. Baseline vs. barrel vs. flat multiplots, operating condition 8; pumping, 1000 rpm, 300 bar, 20%.....	110
7.19. Baseline vs. barrel vs. flat deformations, operating condition 8; pumping, 1000 rpm, 300 bar, 20%.....	111
7.20. Decrease in energy dissipation due to micro-surface shaping of the piston; motoring, full displacement (operating conditions 12-15).	112
7.21. Decrease in leakage due to micro-surface shaping of the piston; motoring, full displacement (operating conditions 12-15).	112
7.22. Baseline vs. waved barrel piston axial friction, operating condition 15; motoring, 2000 rpm, 225 bar, 100%.	113
7.23. Baseline vs. waved barrel deformations, operating condition 15; motoring, 1000 rpm, 225 bar, 100%.....	114

NOMENCLATURE

Symbol	Description	Units
a	Acceleration	[m/s ²]
A	Area	[m ²]
C	Constant	[-]
c_p	Fluid heat capacity	[J/kgK]
d_{Gin}	Slipper inner diameter	[m]
d_{Gout}	Slipper outer diameter	[m]
d_K	Piston diameter	[m]
E	Young's Modulus	[Pa]
E'	Effective stiffness	[Pa]
F	Force	[N]
F_{ak}	Piston axial inertia force	[N]
F_{Ak}	Piston total force	[N]
F_{ck}	Piston correction force	[N]
F_{Dk}	Displacement chamber pressure force	[N]
F_{Sk}	Swash plate reaction force	[N]
F_{TG}	Slipper friction force	[N]
F_{Tk}	Piston viscous friction force	[N]
F_{Sk}	Swash plate reaction force	[N]
$F_{\omega k}$	Piston/slipper centrifugal force	[N]
H_K	Piston stroke	[m]
h	Gap height	[m]
h_G	Slipper fluid film thickness	[m]
h_{min}	Minimum fluid film thickness	[m]
i	Axial index	[-]

Symbol	Description	Units
\bar{i}	Unit vector in x direction	[-]
j	Circumferential index	[-]
\bar{j}	Unit vector in y direction	[-]
L_{apex}	Location of barrel apex	[m]
l_F	Gap length	[m]
$L_{piston\ length}$	Length of piston gap surface	[m]
l_{Sk}	Distance from piston head to center of mass	[m]
l_{var}	Instantaneous gap length	[m]
M	Torque	[Nm]
\mathbf{M}	Columns in fluid film length	[-]
M_{cK}	Piston Correction moment	[Nm]
m_G	Slipper mass	[kg]
m_k	Piston mass	[kg]
MRC	Minimum radial clearance	[m]
N	Volumes in fluid film circumference	[-]
n	Rotational speed	[rpm]
\bar{n}	Surface normal unit vector	
p	Pressure	[bar]
p_{DC}	Displacement chamber pressure	[bar]
Δp	Pressure differential	[bar]
P	Power	[W]
P_L	Power loss	[W]
pc	User specified maximum contact area	
Q	Flow rate	[m ³ /s]
Q_e	Effective flow rate	[m ³ /s]
q_s	Surface thermal flux	[J/m ²]
R_1	Bottom radius – displacement chamber side	[m]
R_2	Apex radius	[m]
R_3	Top radius – case side	[m]

Symbol	Description	Units
R_b	Cylinder block pitch radius	[m]
R_k	Piston radius	[m]
R_z	Cylinder bore radius	[m]
RC	Normalized relative clearance	[-]
s_K	Piston stroke	[m]
T	Temperature	[°C]
t	Time	[s]
u	Fluid velocity	[m/s]
V	Volume	[m ³]
V_i	Derived displacement volume	[m ³]
\mathbf{V}	Fluid velocity vector	[m/s]
v	Fluid velocity	[m/s]
v_k	Piston velocity	[m/s]
z_{Rk}	Distance from piston head to interface beginning	[m]
(x,y,z)	Cartesian coordinate system	[-]
(x_k,y_k,z_k)	Piston Cartesian coordinate system	[-]
$(\hat{x}, \hat{y}, \hat{z})$	Piston unwrapped Cartesian coordinate system	[m]
$\{e_1, e_2, e_3, e_4\}$	Piston eccentricities	[m]
α	Convection Coefficient	[W/m ² K]
β	Swash plate angle	[°]
λ	Thermal conductivity	[W/mK]
μ	Dynamic viscosity	[Pa s]
ρ	Oil density	[kg/m ³]
σ	Contact stress	[Pa]
τ	Viscous sheer stress	[Pa]
Φ_D	Viscous dissipation	[W]
φ	Shaft angular position	[°]
ω	Angular velocity	[rad/s]

LIST OF ABBREVIATIONS

Abbreviation	Description
B	Bushing
CB	Cylinder Block
DC	Displacement Chamber
FEM	Finite Element Method
FSI	Fluid Structure Interaction
FSTI	Fluid Structure Thermal Interaction Model
G	Slipper
HP	High Pressure
IDC	Inner Dead Center
k	Piston
LP	Low pressure
m	Measured
ODC	Outer Dead Center
s	Surface
TH	Thermal
VP	Valve plate
Z	Cylinder Bore
Δ	Change
∇	Gradient
$\nabla \cdot$	Divergence

ABSTRACT

Wondergem, Ashley. M.S.M.E., Purdue University, December 2014. Piston / Cylinder Interface of Axial Piston Machines – Effect of Piston Micro-Surface Shaping. Major Professor: Monika Ivantysynova, School of Mechanical Engineering.

Axial piston machines are widely used in current industries such as aerospace, agriculture, automotive, heavy machinery, military, etc. Thus new cost-effective and highly efficient designs with better performance and reliability are needed. These new, high efficient pumps and motors will also aid in new applications such as hybrid hydrostatic transmissions and displacement controlled actuation. The aim of this work is to study how to reduce the energy dissipation (increase efficiency) while also improving the load carrying ability of the fluid film between the piston and the cylinder through surface shaping of the piston over a wide range of operating conditions. The impacts of this study also include the utilization of modern manufacturing technologies as low tolerances are necessary such that this could affect the overall efficiency of the machine drastically. This study could also open up ways to use water as a lubricating fluid in order to significantly reduce costs. In doing so, a comprehensive understanding of the phenomena occurring between the piston and cylinder will also be achieved in order to find a balance between the viscous friction of the fluid, while reducing any contact occurring, and the leakage. In order to verify the code used in this surface shaping study, a comprehensive study was conducted on the baseline and then compared to measurements.

CHAPTER 1. INTRODUCTION

Axial piston machines are positive displacement machines that convert mechanical and hydraulic energy, mechanical to hydraulic in pumping mode and hydraulic to mechanical in motoring mode. Axial piston machines are widely used in industry due to their compactness and high power density as they are capable of working at very high pressures while still maintaining a high overall efficiency. Examples of such industry use include aeronautical, automotive, agriculture, heavy machinery, construction, robotics, etc. Due to the wide use of such machines and recent developments, it is very important for them to be cost-effective and highly efficient. This study focuses on the design on the piston/cylinder interface of swash plate type machines.

1.1 Main Tribological Interfaces

Axial piston machines of swash plate type have three main tribological interfaces: the piston/cylinder, slipper/swash plate, and the cylinder block/valve plate shown in Figure 1.1. These three lubricating gaps must fulfill simultaneously a bearing and a sealing function; the lubricating film is fundamental to supporting the external loads in order to prevent metal to metal contact that could lead to wear and eventually failure of the unit. The problem that arises is that this same supporting fluid film is also subject to leakages and energy dissipation due to viscous friction associated with the fluid flow.

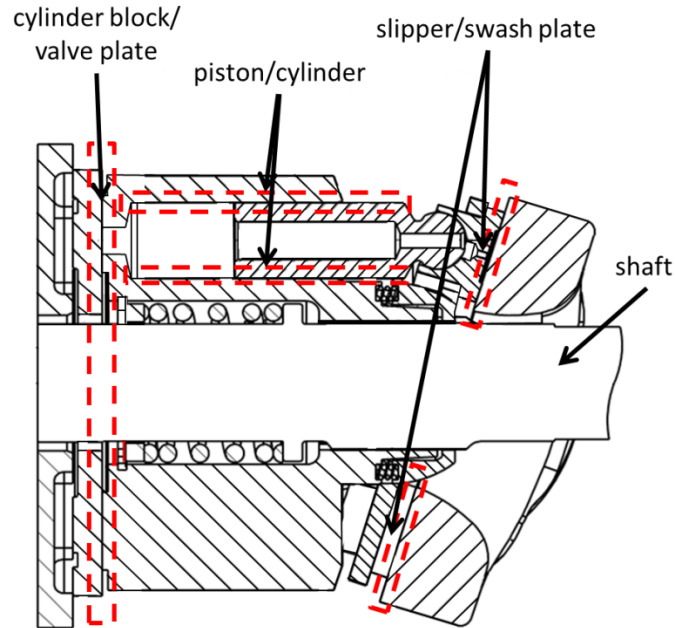


Figure 1.1. Axial piston machine.

1.2 State of the Art

The piston cylinder interface has been the focus of many studies over the past 40 years. In order to verify models along with getting a better understanding of the phenomena occurring in the gap, experimental investigations were conducted using a single piston and inverse kinematics. Van der Kolk (1972) utilized a test rig that did not allow for axial piston motion followed by Renius (1974) who accounted in his test rig for a more complex motion of the piston including axial and spin motion and measured piston friction forces. In 1975, Dowd and Barwell built a test rig to study the impact of material properties and surface roughness on the performance of the piston and cylinder. Then, in 1976, Yamaguchi built a single piston test rig to study the motion and fluid film conditions. Ivantysynova (1983) measured the pressure distribution and temperature distribution within the fluid film between the piston and cylinder in a modified axial piston unit utilizing inverse kinematics, e.g. using a rotating swash plate. This work was followed by several researchers who built test rigs measuring the piston friction force – Ezato and Ikeya (1986), Donders (1998), Manring (1999), Ivantysynova and Lasaar (2000). The test rig of Ivantysynova and Lasaar (2000) allowed for measurements of the piston friction forces on a swash plate machine under conditions comparable to standard

designs over a wide range of operating conditions. In 2002, Oberem used Donders test rig to study the piston friction forces of different piston design and studied the effect of the clearance between the piston and the cylinder. Along with the study of piston friction forces, studies were also done on the temperature field and pressure field between the piston and cylinder – Ivantysynova (1983, 1985), Olems (2001), Ivantysynova, Huang, Behr (2005).

Analytical models were also developed early in conjunction with the experimental work mentioned above. The earliest model was presented by Gerber (1968) in which the gap flow and the friction between the piston and cylinder, not taking into account for hydrodynamic pressure, was calculated. This model was followed by a numerical investigation by Van der Kolk (1972) in which the pressure field was calculated solving for Reynolds equation but neglecting the axial piston motion and only considering the spin motion and inclined position of the piston. Because of the limitation of the computing power at this point, early numerical models were extremely simplified and calculated using a very coarse grid. So, in this case, the models provided only general information and basic guidelines in the design process, yet they opened the door for more involved and advanced computational tools based on the need for such.

As computer speed progressed over the years more advanced models were possible and new phenomena were introduced such as dynamics, non-isothermal flow and heat exchange, and force balance and micro-motion. Yamaguchi (1976) was able to take modeling a step further and consider the dynamic motion of the piston based on hydrodynamic lubrication solving for the Reynolds equation; also considering the change in gap height and the changing of the pressure in the displacement chamber as the machine operates. From his studies, he was the first to conclude that a tapered piston shape may be beneficial in stabilizing the motion of the piston by achieving force equilibrium. From there, Ivantysynova (1983, 1985) presented a non-isothermal model where not only the Reynolds equation was solved for, but the energy equation was also taken into account in order to consider the change in fluid properties due to the change in temperature and pressure. Fang and Shirakashi (1995) for the first time proposed a method to determine the location of the piston considering the force balance with the

assumption of contact forces. Olems (2002) furthered this study by using a non-isothermal model in combination with Newton Raphson's approach to solve for the force balance to determine the micro motion and resulting load carrying capacity. Wieczorek (2002) implemented Olem's method into CASPAR, a simulation model that solves for the three lubricating gaps of a swash plate type axial piston machine.

Through research done in the tribology field, the importance of elastohydrodynamic effects was realized in the piston cylinder interface and even further advanced numerical analysis models. Ivantysynova and Huang (2002) for the first time proposed a model considering the deformation of the piston and the cylinder. The change in the fluid film thickness due to this phenomenon was first calculated using an influence matrix approach solved for using ANSYS. Then, Ivantysynova and Pelosi (2009) presented a huge breakthrough with the fully coupled fluid-structure thermal and multi-body dynamics simulation model for the piston/cylinder interface of swashplate type machines. This model not only considered the elastic deformation due to pressure, but also the thermal expansion of solid parts due to the thermal loading. This model was verified through comparison of measured and calculated piston friction forces as well as calculated and measured temperature fields.

Throughout the research both experimentally and numerically, it has been demonstrated that altering the shape and material of the piston and cylinder can lead to lower energy dissipation and improved load carrying ability of the fluid film between the piston and the cylinder. As previously stated, Yamaguchi (1976) was the first to conclude that micro- shaping of the piston surface may be beneficial in the load carrying ability of the fluid film. Ivantysynova (1983) proposed a barrel like piston with a large curvature radius and diameter reduction at both ends of the piston. Lasaar (2003) and Fredrickson (2008) continued this work on optimizing the piston shape to minimize energy dissipation with a half barrel like piston (Figure 1.2) and a sine waved barrel micro-surface piston shape; both demonstrating a reduction in energy dissipation along with friction work for the piston cylinder interface, but these simulations were done with a model that neglected the material deformation on the energy dissipation in the gap which was later found to be crucial to the predicted fluid behavior. Ivantysynova and Garrett (2009) file a patent for a

sine wave (Figure 1.3) in which up to a 60% decrease in total power loss was achieved in simulations. Kleist (1997) also concluded through simulation that different shaped pistons showed lower friction and comparable leakage to a cylindrical piston. Murrenhoff (2010) not only studied the shape of the piston and bushing, but also studied various coatings and surface textures leading to the conclusion through measurements that friction was only reduced for the low pressure/suction stroke.

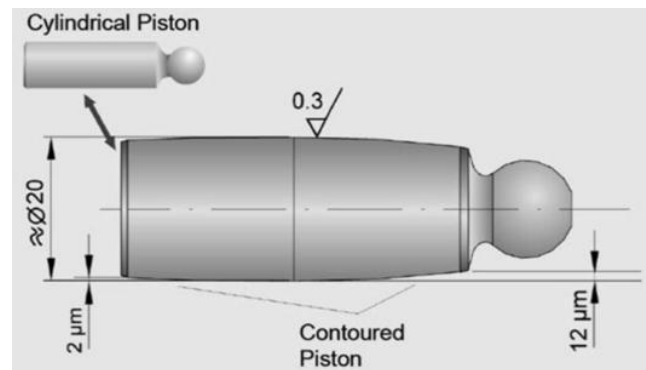


Figure 1.2. Half barrel like piston surface shape (Lassar, 2003).

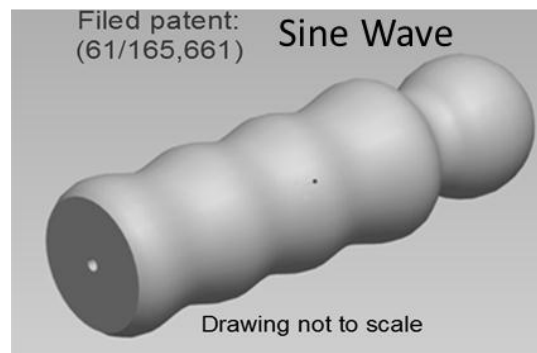


Figure 1.3. Sine wave piston surface shape (Garrett, 2009).

1.3 Aims and Goals of Work

The aim of the work presented in this thesis is to investigate the effects of micro-surface shaping on the piston utilizing the fluid structure interaction model developed by Pelosi. The investigation has to be done over a comprehensive range of operating conditions, in order to understand the effect of the design principles on the load carrying ability, performance and reliability, of the interface along with the total energy

dissipation of the lubricating gap. Also included is the verification of the code in order to better understand the physical phenomena occurring in the fluid lubricating gap. The trends found in this work will be useful for future design of this lubricating interface.

CHAPTER 2. THE PISTON / CYLINDER INTERFACE

2.1 Introduction to Axial Piston Machines

Axial piston machines of swash plate type are commonly comprised of a fixed number of piston slipper pairs arranged at a certain pitch diameter centered around the shaft of the block. These piston/slipper assemblies are pressed against the stationary inclined swash plate by pressure forces acting during the high pressure stroke and are held on the swash plate during low pressure stroke and/or low pressure operation by a fixed hold down or a spring system. The stroke of the piston depends on the angle of inclination of the swash plate. As the piston moves from the inner dead center (IDC) (shown in Figure 2.1), the displacement volume increases as the suction stroke takes in fluid from the machine inlet port. As the piston moves from it outer dead center (ODC) (shown in Figure 2.1), the displacement volume is decreased as fluid is displaced to the discharge port.

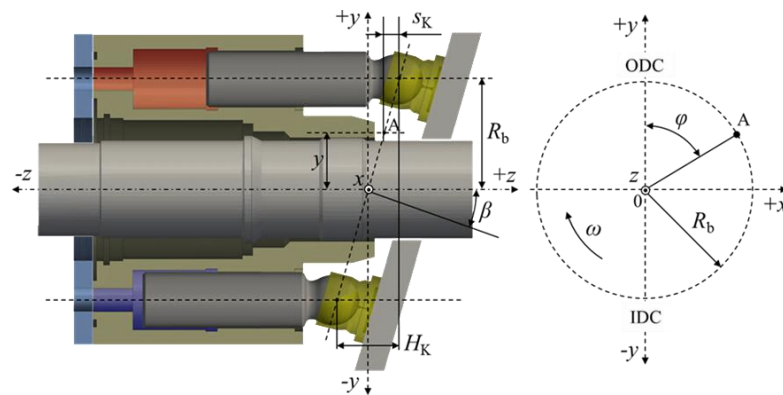


Figure 2.1. Axial piston machine and reference system (Pelosi, 2012).

Axial piston machines of swash plate type are capable of working in both pumping and motoring mode. In pumping mode, low pressure fluid is drawn from the inlet and discharged during delivery stroke to the outlet; in other words, the pump converts

mechanical power into fluid power. In the case of motoring mode, high pressure fluid enters through the inlet and generates high forces on each piston and consequently results in fluid power being converted into mechanical power.

2.2 Axial Piston Machine Kinematics

The kinematics of an axial piston machine is very important to characterize correctly in order to study and reach a better understanding of the piston/cylinder performance. Figure 2.1 shows the machine with the reference system used to determine the kinematics and in turn the motion of the piston within the cylinder.

The center point O references the origin of the coordinate system. The origin is determined by the intersection of the center axis of the shaft and the parallel plane to the swash plate that intersects the center of the ball joint of the piston/slipper assembly. In Figure 2.1, ODC (+y axis) is where the transition from suction stroke to delivery stroke occurs while vice versa at IDC (-y axis).

The position of the piston during the stroke with respect to the z axis is defined by Ivantysyn and Ivantysynova (2001)

$$s_k = -z. \quad (2.1)$$

From Figure 2.1 it follows that

$$z = (R_b - y) \tan \beta \quad \text{and} \quad (2.2)$$

$$y = R_b \cos \varphi. \quad (2.3)$$

Therefore,

$$s_k = -R_b \tan \beta (1 - \cos \varphi). \quad (2.4)$$

The piston displacement, s_k , is dependent on the pitch radius of the block, R_b , the changing angular position of the swash plate due to variable displacement, β , and the angular position of the piston with respect to the center axis of the shaft (z axis), φ .

The larger the swash plate angle, β , the larger the displacement of the machine due to the larger stroke of the piston. The stroke of the piston is defined as

$$H_k = 2R_b \tan \beta. \quad (2.5)$$

The piston velocity and acceleration are respectively defined as

$$v_k = \frac{ds_k}{d\phi} \omega = -\frac{1}{2} \omega H_k \sin \varphi, \quad (2.6)$$

$$a_k = \frac{dv_k}{d\phi} \omega = -\frac{1}{2} \omega^2 H_k \cos \varphi. \quad (2.7)$$

Under the assumption that the ball joint connection between the piston and the slipper is rigid and does not allow for relative motion, relative motion occurs between the piston and the cylinder in a rotational direction as well as in an axial direction.

2.3 Function of the Piston / Cylinder Interface

Since the piston/cylinder interface cannot be hydrostatically balanced, unlike the other two main interfaces, it must be balanced by a hydrodynamic load generated by the pressure in the fluid film. This load bearing function along with a simultaneous sealing function of the piston/cylinder interface is crucial to reliable operation of the machine.

Adequate hydrodynamic pressure to support the external loads is generated through different phenomena including the macro and micro motion of the piston creating a squeeze effect, the deformation of the surface due to pressure and thermal loading, the self-adjusted eccentric position of the piston, with the sliding and rotational motion of the piston in reference to the stationary block. In other words, the hydrodynamic pressure is strongly dependent on the fluid film geometry and the change in geometry with respect to motion. This is strongly dependent on the change in displacement chamber (DC) pressure, shown in Figure 2.2 resulting in oscillating loads exerted on the piston.

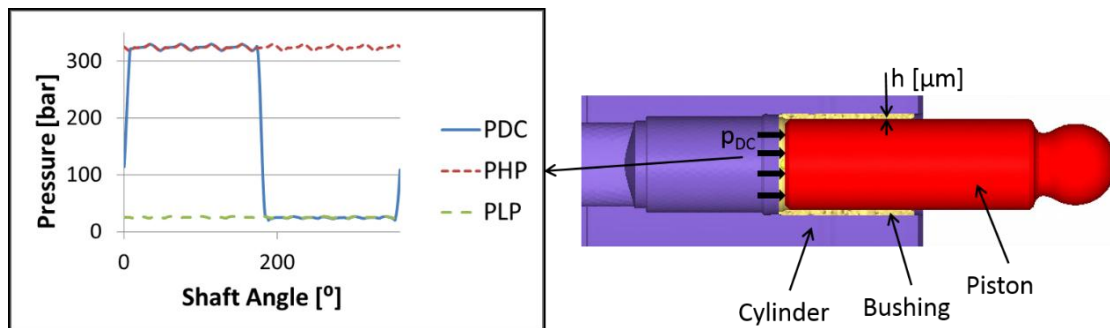


Figure 2.2. Piston/Cylinder showing DC pressure change.

Therefore, one of the main functions of the piston/cylinder interface is to bear the dynamic external loads and transfer forces to the cylinder block through a sufficiently stable fluid film.

The significant difference in pressure between ambient and the DC results in a leakage flow of the fluid. For this reason, another important function of the piston/cylinder interface is to simultaneously seal the pressurized fluid in the displacement chamber through a thin fluid film. The leakage flow between the piston and the cylinder along with the viscous friction in the fluid results in the total energy dissipation of the interface. In order to increase overall efficiency of a machine, the energy dissipation of each interface must be minimized, but this presents a dilemma: to reduce leakage, the fluid film must be minimal, however, to reduce viscous friction, the fluid film must be generous.

2.4 Dynamic Loading Conditions of the Piston / Cylinder Interface

In order to understand the challenges of the lubricating film between the piston and the cylinder and to better predict the performance of the machine, it is imperative to correctly define the various forces that interact with the piston/cylinder interface. All of these external forces are contingent on the geometry and operating condition of the machine. These forces are represented in Figure 2.3 and further described in this section.

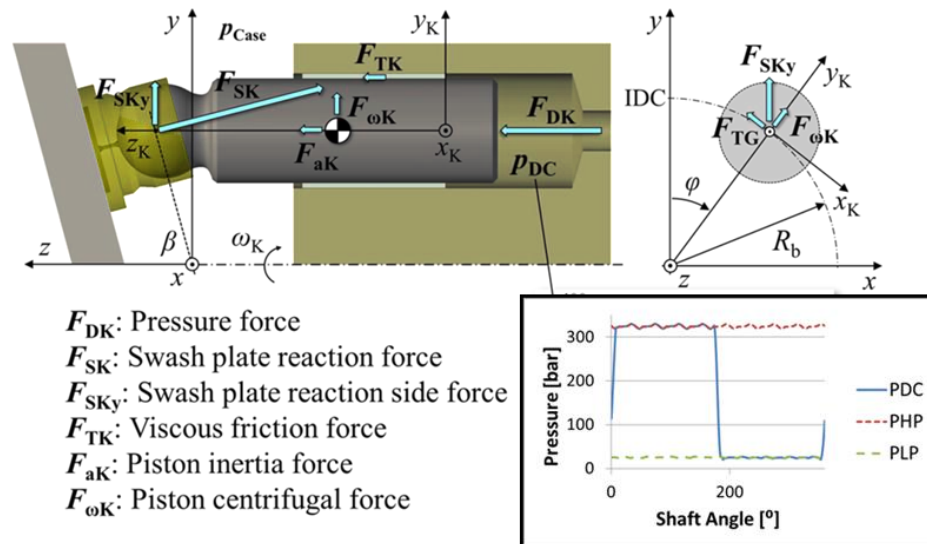


Figure 2.3. Forces acting on the piston/cylinder interface.

It is necessary to apply a Cartesian coordinate system, (x_k, y_k, z_k) , to the piston with respect to deriving and representing the forces acting on the piston body as can be seen in Figure 2.3 also. This coordinate system rotates with the block and therefore the y_k axis is always represented as pointing outward in the direction of rotation while the z_k axis always lies through the center axis of the cylinder bore. The origin of the coordinate system remains at the beginning of the gap surface on the DC side; this is not always located at the end of the piston guide and can vary throughout a revolution as the piston moves axially in the cylinder bore.

The largest force acting on the piston is the pressure force from the displacement chamber pressure, F_{Dk} indicated by

$$F_{DK} = \frac{\pi d_k^2}{4} (p_{DC} - p_{Case}). \quad (2.8)$$

Other contributing external forces acting on the piston along the piston axis z_k include the piston axial inertia force, F_{ak} , due to the acceleration of the piston a_k

$$F_{ak} = -m_k a_k = m_k \omega^2 R_b \tan \beta \cos \varphi. \quad (2.9)$$

The viscous friction forces due to the viscosity of the fluid, F_{Tk} , over a shaft revolution are given by

$$F_{Tk}(\varphi) = \int_A \tau(\varphi) dA. \quad (2.10)$$

The comprehensive external forces acting on the piston along the piston axis z_k is

$$F_{Ak} = +F_{ak} + F_{Tk}. \quad (2.11)$$

This comprehensive force is transferred through the piston to the attached slipper and onto the swashplate in which the reaction force from the swash plate, F_{Sk} , including the swash plate reaction side force, F_{Sky} , are reciprocated by

$$F_{Sk} = -\frac{F_{Ak}}{\cos \beta} \text{ and} \quad (2.12)$$

$$F_{Sky} = F_{Ak} \tan \beta. \quad (2.13)$$

The centrifugal force due to the rotation of the mass of the piston and slipper around the shaft, $F_{\omega k}$ is calculated

$$F_{\omega k} = (m_k + m_G)\omega^2 R_b. \quad (2.14)$$

And finally, a minor external load coming from the viscous friction force between the slipper and the swash plate, F_{TG} is considered as

$$F_{TG} = \mu \frac{\omega R_b}{h_G} \left[\frac{\pi}{4} (d_{Gout}^2 - d_{Gin}^2) \right]. \quad (2.15)$$

All of these forces can be condensed into

$$F_{kx} = -F_{Sky} \sin \varphi + F_{TG} \quad \text{and} \quad (2.16)$$

$$F_{ky} = F_{Sky} \cos \varphi + F_{\omega k} \quad (2.17)$$

with the external moments

$$M_{kx} = -z_{Rk} F_{Sky} \cos \varphi - (z_{Rk} - l_{Sk}) F_{\omega k} \quad \text{and} \quad (2.18)$$

$$M_{ky} = z_{Rk} F_{kx}. \quad (2.19)$$

Under full film lubrication, no contact between the piston and the cylinder, these forces and moments are fully supported by the load carrying ability of the fluid film; the hydrodynamic pressure balances the external forces and moments produced.

2.5 Piston / Cylinder Fluid Film Geometry

For a better understanding of the phenomena occurring in the fluid film gap along with a comprehensive analysis of the performance of the piston/cylinder interface, it is essential to correctly define the fluid film geometry. Figure 2.4 presents a fluid film between the piston and the cylinder; shown in yellow and represented as h . It is assumed that the cylindrical sleeve is wrapped around the piston that moves axially and circumferentially in time.

The motion of the piston in reference to cylinder axis is described as the eccentric position, $\{e_1, e_2, e_3, e_4\}$, and changes over a shaft revolution in a defined periodic time. The definition of the eccentric position of the piston is shown in Figure 2.4 in which the fluid

film thickness, h , is defined base on each eccentric position of the piston as developed by Wieczorek and Ivantysynova (2002).

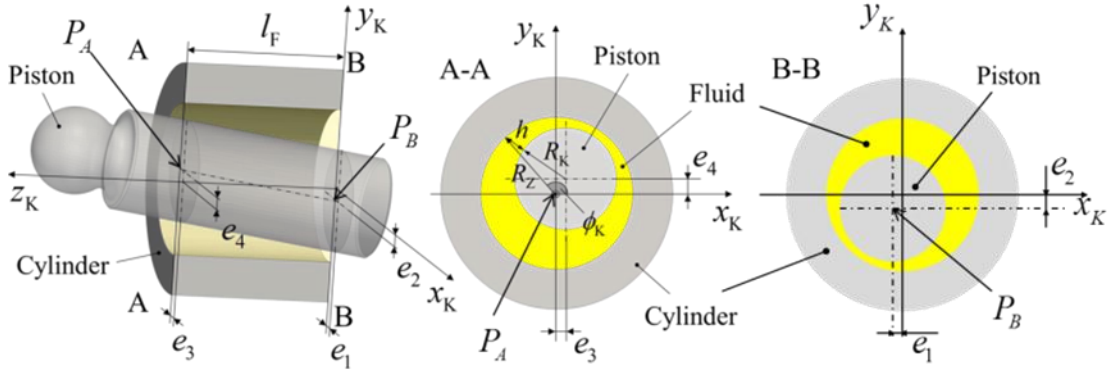


Figure 2.4. Eccentric position of the piston in the cylinder bore (Pelosi, 2012).

The eccentricity of the piston with respect to the piston Cartesian system is as

$$x_m(z_k) = \frac{e_3 - e_1}{l_F} z_k + e_1 \quad \text{and} \quad (2.20)$$

$$y_m(z_k) = \frac{e_4 - e_2}{l_F} z_k + e_2. \quad (2.21)$$

From these equations, the fluid film thickness between the inclined piston and the cylinder bore can be determined by

$$h(z_k, \varphi_k) = \sqrt{(R_Z \cos \varphi_k - x_m(z_k))^2 + (R_Z \sin \varphi_k - y_m(z_k))^2} - R_k + \Delta h. \quad (2.22)$$

The effect of the surface elastic deformations of the piston and the cylinder due to pressure and thermal effects are captured in the Δh term. Figure 2.5 shows a typical unwrapped fluid film geometry on the right based on the depicted piston position on the left. The unwrapped film is based on the following coordinates:

$$\text{Piston Circumference } (2\pi R_k): \quad \hat{x} = \varphi_k R_k \quad (2.23)$$

$$\text{Gap length } (l_F): \quad \hat{y} = z_k \quad (2.24)$$

$$\text{Fluid film thickness:} \quad \hat{z} = h \quad (2.25)$$

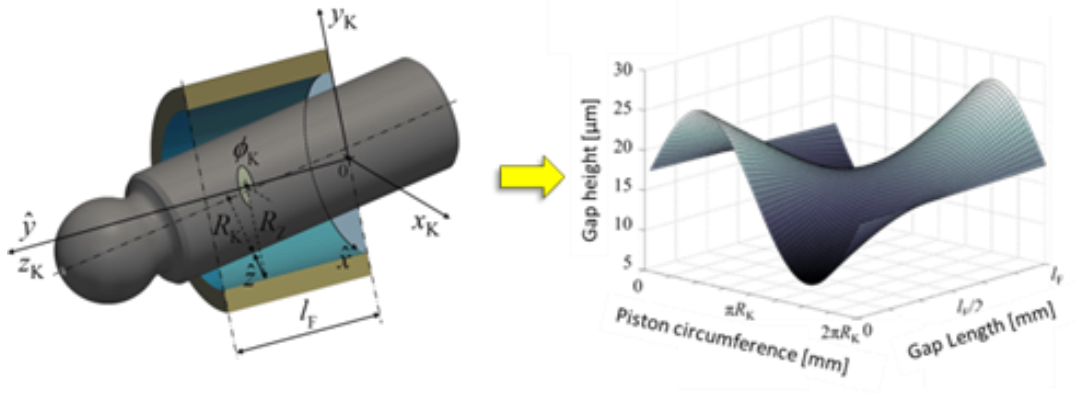


Figure 2.5. Unwrapped fluid film geometry (Pelosi, 2012).

CHAPTER 3. NUMERICAL MODEL

3.1 Overview of the Numerical Model

In this section the numerical model utilized in the study of various micro-surface shapes on the piston is described. This numerical model is represented by the core behavior of the piston/cylinder interface: a non-isothermal fluid film flow governed by the Reynolds and energy equations solved using a finite volume method. The lubricating fluid film is defined by the interaction of the pressure and temperature fields with the solid bodies; a dynamic fluid-structure interaction problem. These parameters are crucial for the correct prediction and detailed analysis of the piston/cylinder interface.

3.1.1 Reynolds Equation

The Reynolds equation is derived mainly from the Navier-Stokes, expressing the fluid velocity, and the continuity equations, integrated over the film thickness. Also to be considered is the aspects that effect the fluid film: the high pressure loads and the thermal gradients that deform the solid along with the ability to introduce a surface shape to the solid bodies. From this, Ivantysynova and Pelosi (2009) introduced a more complete version of the Reynolds equation to model the piston/cylinder interface in reference to Figure 3.1, this expression is given by

$$\begin{aligned} \frac{\partial}{\partial x} \left(h^3 \frac{\partial p}{\partial x} \right) + \frac{\partial}{\partial x} \left(h^3 \frac{\partial p}{\partial x} \right) + \frac{\partial}{\partial y} \left(h^3 \frac{\partial p}{\partial y} \right) + 6\mu \left[\hat{u}_k \left(2 \frac{\partial |h_b|}{\partial x} - \frac{\partial h}{\partial x} \right) + \right. \\ \left. \hat{v}_k \left(2 \frac{\partial |h_b|}{\partial y} - \frac{\partial h}{\partial y} \right) + 2 \frac{\partial h}{\partial t} \right] = 0. \end{aligned} \quad (3.1)$$

Assuming that steady state is reached the inertial forces are negligible in comparison to the viscous forces. It is also assumed that the cylinder is fixed and the piston is the only moving surface.

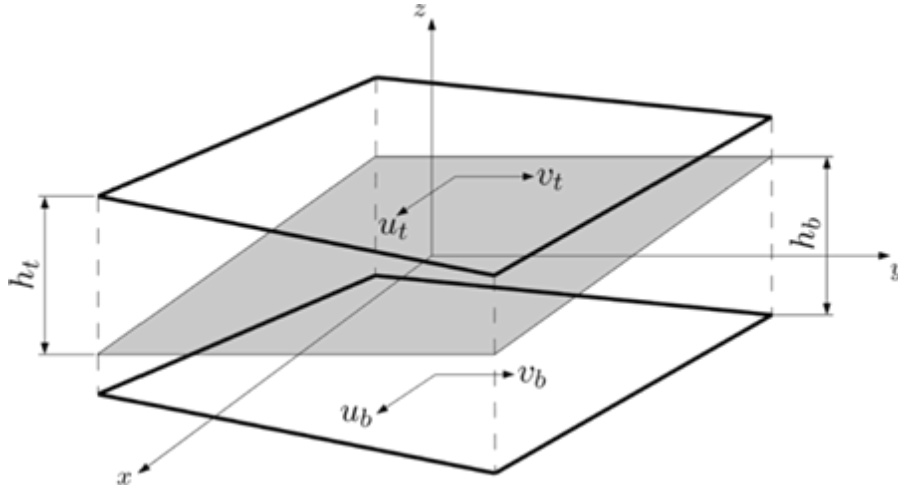


Figure 3.1. Fluid film geometry (Pelosi, 2012).

The fluid velocities considered for the Reynolds equation and also important to determine the leakage flow and viscous friction forces are expressed as

$$\begin{cases} u = \frac{1}{2\mu} \frac{\partial p}{\partial x} (z^2 + zh + h_t h_b) + z \frac{u_t - u_b}{h} + \frac{u_b h_t - u_t h_b}{h} \\ v = \frac{1}{2\mu} \frac{\partial p}{\partial y} (z^2 + zh + h_t h_b) + z \frac{v_t - v_b}{h} + \frac{v_b h_t - v_t h_b}{h} \end{cases} \quad (3.2)$$

where the term related to the pressure gradient is the Poiseuille component and the term related to the piston sliding motion is called the Couette component.

When it comes to the micro-surface shaping of the solid bodies, in this case the piston, a critical aspect of the Reynolds equation is to predict extremely low regions of fluid film pressures. Although numerically the equations allow for predicting negative fluid film thicknesses, it is known that the pressures will never be negative and therefore the pressure is saturated to zero at such boundaries in order to ensure flow continuity in these regions. As a result, the effect of micro-surface shaping of the piston can be investigated via numerical modeling.

3.1.2 Energy Equation

The energy equation must be considered in the non-isothermal fluid flow numerical model in order to predict the temperature distribution in the fluid film within

the gap which in turn determines the fluid properties such as the density, viscosity, etc. along with the heat flux resulting on the solid mechanical bodies from the fluid film that then results in the deformation of the bodies. The energy equation in differential form considering steady-state fluid flow is expressed as (Pelosi 2012)

$$\rho c_p \mathbf{V} \cdot \nabla T = \nabla \cdot (\lambda \nabla T) + \mu \Phi_D. \quad (3.3)$$

In reference to the piston/cylinder coordinate system, the energy equation in Eq. (3.3) is expressed as

$$c_p \left(\hat{u} \frac{\partial T}{\partial \hat{x}} + \hat{v} \frac{\partial T}{\partial \hat{y}} \right) = \frac{1}{\rho} \left[\frac{\partial}{\partial \hat{x}} \left(\lambda \frac{\partial T}{\partial \hat{x}} \right) + \frac{\partial}{\partial \hat{y}} \left(\lambda \frac{\partial T}{\partial \hat{y}} \right) + \frac{\partial}{\partial \hat{z}} \left(\lambda \frac{\partial T}{\partial \hat{z}} \right) \right] + \frac{\mu}{\rho} \Phi_D. \quad (3.4)$$

This equation contains the source term, the mechanical dissipation, Φ_D , in which the heat generated by the viscous shear of the fluid is expressed. This mechanical dissipation is defined in the Cartesian coordinate system by

$$\Phi_D = \left(\frac{\partial \hat{u}}{\partial \hat{z}} \right)^2 + \left(\frac{\partial \hat{v}}{\partial \hat{z}} \right)^2. \quad (3.5)$$

3.1.3 Energy Dissipation and Leakage

The non-isothermal fluid flow model described in the equations above is used to determine the energy dissipation occurring in the fluid film of the gap. By correctly predicting the losses of the interface, the simulation model can be used to study better designs.

The losses in the lubricating gap between the piston and the cylinder ensue from both volumetric (leakages) and mechanical (torque) losses. The main contribution, the energy dissipation, Φ_D , is due to the viscous shearing of the fluid in the gap. From the fluid velocity distribution occurring, the shear stresses on the piston and the cylinder can be determined in both the axial and the circumferential directions. By integrating these shear stress components over the surface areas the total viscous friction force is

$$F_T(\varphi) = \int_A \tau(\varphi) dA. \quad (3.6)$$

From this equation, it can be noted that the viscous friction forces change over on shaft revolution based on the dynamic loading conditions on the piston as the shaft angle, φ , progresses through on revolution.

The leakage, another form of losses in the gap, results from the gap flow flowing from the pressurized displacement chamber into the case as

$$Q_{sk}(\varphi) = \int_0^{2\pi R_k} \int_0^h \hat{v}(\varphi) d\hat{z} d\hat{x}. \quad (3.7)$$

From this equation, it can again be noted, that such as the viscous friction, the volumetric losses also vary over one shaft revolution. Both the Poiseuille and Couette flow are accounted for in the leakage flow losses.

As part of the fluid structure interaction model detailed in the following section, an output of the model is the energy dissipation due to the viscous flow, Φ_D . The total energy dissipated due to the viscous flow in the lubricating gap between the piston and the cylinder is calculated based on the power per unit dissipated or in other words the heat generated by the viscous shear of the fluid as shown in Eq. (3.5).

3.2 Fluid Structure Thermal Interaction Model

The numerical model used to predict the behavior of the fluid film with the Reynolds equation and the energy equation as the basis is a novel fluid structure interaction model coupling both the thermal and elasto-hydrodynamic effects specifically designed for the piston/cylinder interface as proposed by Pelosi (2012). This model captures the impact of micro and macro motion of the piston, fluid and material properties, heat transfer, surface shape, and deformation of the solid parts (the piston and cylinder) due to the pressure and thermal loading of the piston and cylinder. The model predicts the behavior in reference to a single piston and cylinder segment solving at discrete time steps for the dynamic loading conditions over a complete shaft revolution of the machine. Although only a segment of the cylinder is solved for, the entire block is considered in the simulation in order to take account for the effects of neighboring bores on the displacement chamber pressure considered for the reference segment. Utilized this

model, further studies may be done in order to better understand the phenomena and optimize the piston cylinder interface due to piston surface micro-shaping.

The overview of this fluid structure interaction model is indicated in Figure 3.2 in which it can be seen that three main modules compose the overall model.

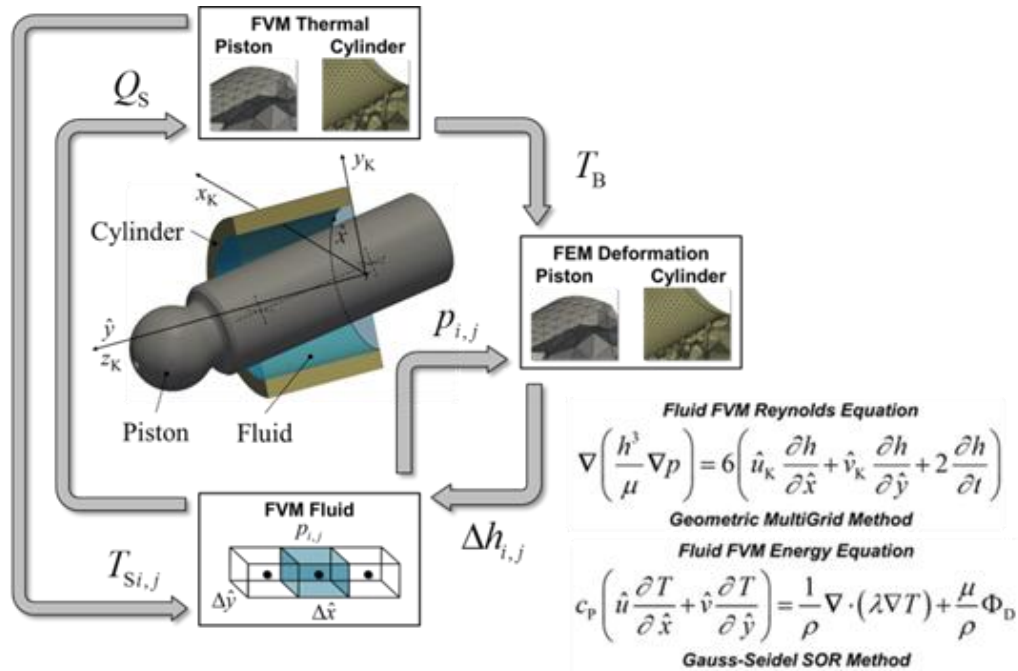


Figure 3.2. Fluid structure thermal interaction model (Pelosi, 2012).

The first, and possibly most important, module solves for the Reynolds and energy equations simultaneously using a finite volume method. As these equations are solved, the dynamic changes in the fluid properties due to the pressure and temperature variation over one shaft revolution are considered. The dynamically changing pressure field is then considered in the changing elastic deformation of the solid bodies. Correspondingly, the fluid film thickness changes are calculated and coupled with the non-isothermal fluid film model.

The second module of the complete model solves for the heat transfer using a finite volume method. The heat fluxes due to the viscous dissipation of the fluid is first calculated in which the temperature distribution on the solid mechanical parts can then be sequentially solved for. This predicted temperature distribution on the solid bodies is then applied as the current boundary surface temperatures affecting the fluid film properties

and the calculation of the energy equation. The heat fluxes also affect the fluid film thickness in the sense that the internal stress loading conditions applied to the piston and the cylinder based on the thermal boundary conditions result in thermal elastic deflection altering the shape of the solid bodies and modifying the film thickness in the gap.

The final module represented in Figure 3.2 solves for the elastic deformations using a finite element method. The elastic deformation of the solid bodies is determined based on the external loads due to the dynamic pressure conditions along with the internal loads due to the temperature. The solution of the deformation based on pressure is obtained using an influence method and completing FEM analysis off-line while the thermal deformation is solved running complete FEM analysis during the run-time.

The deformations that are solved for in the final module of the complete model are very important to the results of the simulation, having a large effect on the behavior of the fluid film of the interface. The importance of considering the deformations in the overall model was studied by Pelosi and Ivantysynova (2011) in a comparison between measurements and simulations in which by taking into account for, the model was able to more accurately predict the outcome of measurements than a previous rigid model.

CHAPTER 4. BASELINE SIMULATION AND MEASUREMENTS

It is necessary to establish a complete baseline for comparison purposes. The first step of this process is to take steady state measurements. The next step is to then use the port and case flow temperature measurements as accurate inputs into the simulation model and run simulations for the baseline unit. These numerical results of the piston/cylinder interface are then used for creating a standard baseline for the research study of surface shaping of the piston. The baseline measurements were made at high and low speeds in combination with high and low pressures at full and partial displacements in both pumping and motoring modes, as shown in the following section, on a standard, 75 cc stock unit. Once this baseline investigation was made for comparison purposes, simulations on various piston surface profiles and configurations at these various operating conditions were conducted and then compared to the baseline to determine the magnitude of reduction in power losses while also considering the gap height in order to reach a deeper understanding of the physical phenomena occurring in the gap in order to further improve the interface.

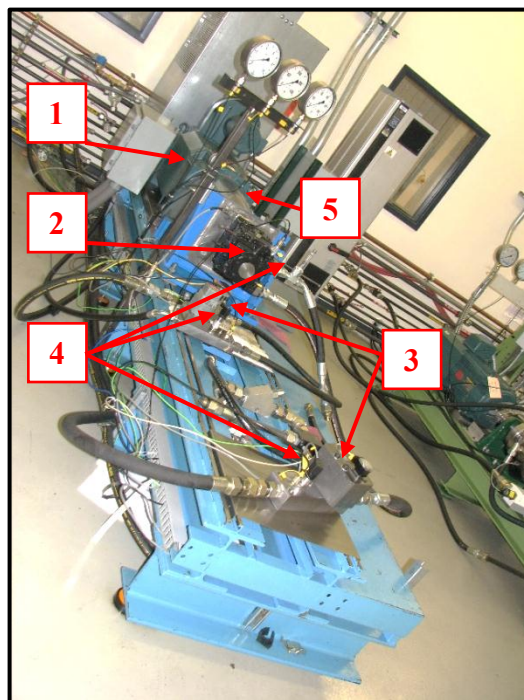
4.1 Steady State Measurements

In the following investigation various operating conditions of the machine in both pumping and motoring mode were chosen in order to investigate the operating of the machine over a wide range. These measurements were taken under steady-state conditions; ISO 4409 in which the inlet temperature must remain constant during the measurements in turn maintaining a constant viscosity. The permissible systematic errors for class B of measurement accuracy were considered as detailed in Table 4.1.

The baseline for comparison is a standard 75 cc stock unit. The fluid used in measurements from which the operating temperature were acquired and the losses were calculated was a hydraulic oil with viscosity grade 32 which was then consequently also considered for all simulation studies. The temperatures at the high pressure port, the low pressure port, and the case, the pressures at the high pressure port, the low pressure port, and leakage port, the flow rates at the high pressure port and the leakage port, the speed, and the torque were all measured at steady state condition with a constant inlet temperature. The temperatures are used as accurate inputs into the simulation study while the losses are later compared in order to verify the code being used.

Table 4.1. ISO measurement accuracy class B.

Parameter	Permissible error	Units
Rotational frequency	± 1.0	%
Torque	± 1.0	%
Volumetric flow rate	± 1.5	%
Pressure below 2 bar gauge	± 0.03	bar
Pressure greater than or equal to 2 bar pressure gauge	± 1.5	%
Temperature	± 1.0	$^{\circ}\text{C}$



1	Electric motor
2	Hydraulic unit
3	Flow meter
4	Pressure sensor
5	Torque meter

Figure 4.1. Steady-state measurement test rig.

The data acquisition system along with the sensors used are further detailed in Table 4.2 and Table 4.3 respectively.

Table 4.2. Steady-state measurement data acquisition.

Component	Specifications/Functions
NI cDAQ	<ul style="list-style-type: none"> • Data acquisition • Timing resolution of 12.5 ms
NI 9205	<ul style="list-style-type: none"> • 8-channel analog input module • Input range: ± 10 VDC • Maximum sampling rate: 500 KS/s • Resolution: 12-bit
NI 9211	<ul style="list-style-type: none"> • 8-channel thermocouple module • Input range: ± 80mVDC • Maximum sampling rate: 14 KS/s • Resolution: 24-bit

Table 4.3. Steady-state measurement sensors.








Sensor Type	Company	Accuracy	Measuring Principle	Range	Signal Output	Band width
Pressure Sensor (delivery port)	 (S-10)	< 0.25 %	Piezoresistive and thin-film technology	0 to 600 bar	1-10 VDC	1000 kHz
Pressure Sensor (low port)	 (S-10)	< 0.25 %	Piezoresistive and thin-film technology	1 to 100 bar	1-10 VDC	1000 Hz
Pressure Sensor (case port)	 (S-10)	< 0.25 %	Piezoresistive and thin-film technology	0 to 25 bar	1-10 VDC	1000 Hz
Flow Meter (case port)		± 0.3 % @ >20cP Repeatability ± 0.05 %	Gear flow meter with magnetic pick-up	0.02 to 18 [l/min]	Dual pulse $V_{\text{supp}} - 1$ VDC	1.2 to 1500 Hz
Flow Meter (delivery port)	 (VC)	± 3 % Linearity ± 1.5 %	Gear flow meter with magnetic pick-up	1.0 to 250 [l/min]	Dual pulse $0.8 * V_{\text{supp}}$ VDC	N/A

Table 4.3. Continued

Torque Meter		0.5% Linearity $\pm 0.5\%$	Strain gage	1 to 1000 Nm	± 0 to 10 VDC	1500 Hz
Thermocouple (Type K)		± 1.5 (-40 and 375 °C) $\pm 0.004 \times T$ (375 and 1000 °C)	junction end thermoelements	180 to +1300 [°C]	N/A	0.5 Hz

It is important to mention that the primary mover's rotational speed is integrated into the controls of the electric motor

4.1.1 Pumping Mode

The test set up for pumping mode is shown in Figure 4.2. The test procedure is shown in Table 4.4 considering the desired operating conditions to be measured. It is important to mention that the unit displacement was controlled using a set screw.

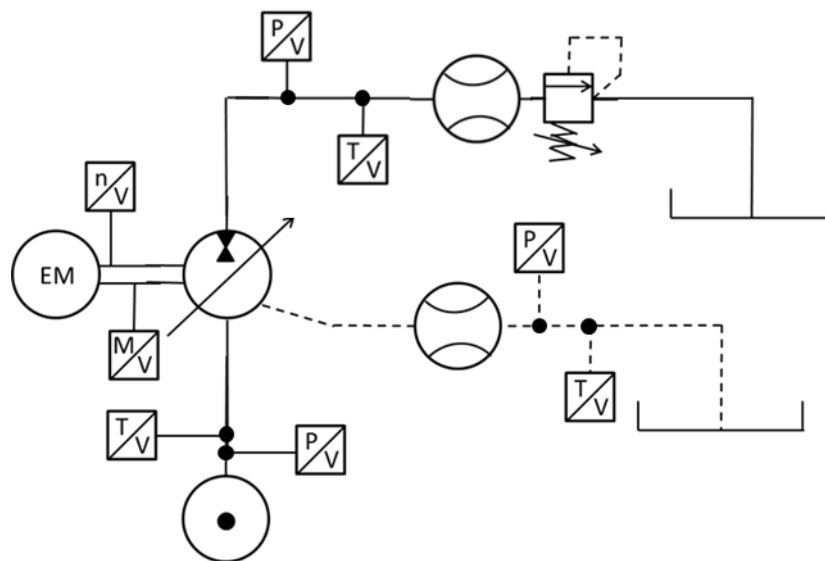
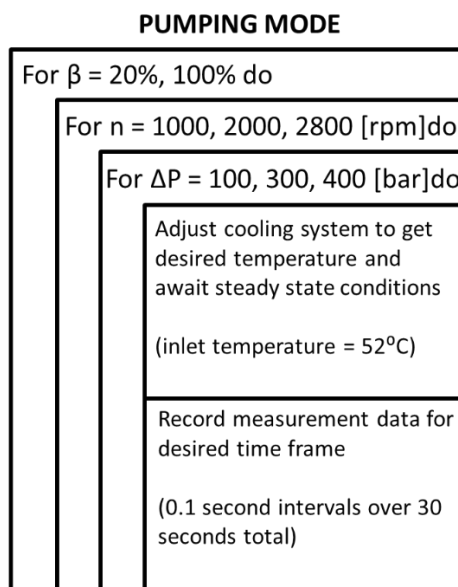


Figure 4.2. Baseline pumping mode test set up.

Table 4.4. Baseline pumping mode test procedure



The test procedure detailed above is necessary for steady-state conditions. As shown, first a swash plate angle is chosen, from there, the speed and pressure of the desired operating condition is set. Once the operating condition is achieved, the cooling system is adjusted to the desired inlet fluid temperature. Once steady state conditions are reached and the inlet temperature has not varied for 10 minutes, the measurement data is recorded for the set time frame; in this case, 0.1 second intervals for 30 seconds.

The temperature results of the measured data for the pumping mode operating conditions are shown below in Table 4.5 and

Table 4.6; all measured parameters are further shown in Appendix 2. The measured operating conditions that are later to be simulated are numbered 1-11 while those labeled A-D were only measured and not considered in the simulation study. Operating conditions 1-8, Table 4.5, are considered based on the commonality of such operating conditions and represent the most frequently used operating range where improvements of efficiency are very important. Operating conditions 9-11 and A-D,

Table 4.6, were selected since they represent the more extreme operating conditions that the machine is capable of; high pressures and high speeds. It is important to ensure that the machine will still run at these operating conditions throughout the study.

Table 4.5. Baseline pumping mode measured temperature results; common operating conditions.

Operating Condition - Pumping ($\beta = 100\%$)	1	2	3	4	Unit
High Pressure	125	325	125	325	bar
Low Pressure	25	25	25	25	bar
Angular Speed	1000	1000	2000	2000	rpm
Case Temperature	50.81	57.10	56.96	64.60	°C
Temperature at High Pressure Port	53.66	56.80	53.43	56.30	°C
Temperature at Low Pressure Port	52.4	52.5	52.2	52.4	°C
Swash Plate Angle	17	17	17	17	°

Operating Condition - Pumping ($\beta = 20\%$)	5	6	7	8	Unit
High Pressure	125	325	125	325	bar
Low Pressure	25	25	25	25	bar
Angular Speed	1000	1000	2000	2000	rpm
Case Temperature	60.09	70.87	59.99	68.23	°C
Temperature at High Pressure Port	55.14	64.09	54.75	59.88	°C
Temperature at Low Pressure Port	52.2	52.1	52.3	52.3	°C
Swash Plate Angle	3.4	3.4	3.4	3.4	°

Table 4.6. Baseline pumping mode measured temperature results; high pressure operating conditions.

Operating Condition - Pumping ($\beta = 100\%$)	9	10	A	11	Unit
High Pressure	425	425	325	425	bar
Low Pressure	25	25	25	25	bar
Angular Speed	1000	2000	2800	2800	rpm
Case Temperature	70.20	73.00	75.00	76.37	°C
Temperature at High Pressure Port	59.40	58.60	57.29	58.69	°C
Temperature at Low Pressure Port	52.4	52.4	52.5	52.7	°C
Swash Plate Angle	17	17	17	17	°

Operating Condition - Pumping ($\beta=20\%$)	B	C	D	Unit
High Pressure	425	325	425	bar
Low Pressure	25	25	25	bar
Angular Speed	2000	2800	2800	rpm
Case Temperature	76.24	71.39	76.82	°C
Temperature at High Pressure Port	66.09	61.53	65.80	°C
Temperature at Low Pressure Port	52.4	52.6	52.4	°C
Swash Plate Angle	3.4	3.4	3.4	°

4.1.2 Motoring Mode

The test set up for motoring mode is shown in Figure 4.3. While the test procedure described above remains the same, the speeds and pressures measured are slightly different for motoring mode as shown below in Table 4.7; the high speeds and high pressures were not considered based on the limited torque on the electric motor. The measurements were taken at full displacement (operating conditions 12-15 that were later simulated) and additionally include partial displacement (operating conditions E-H that were not considered in simulation studies). Notice that in the circuit that was implemented for motoring mode that the flow is now measured at the inlet (remains at the high pressure port).

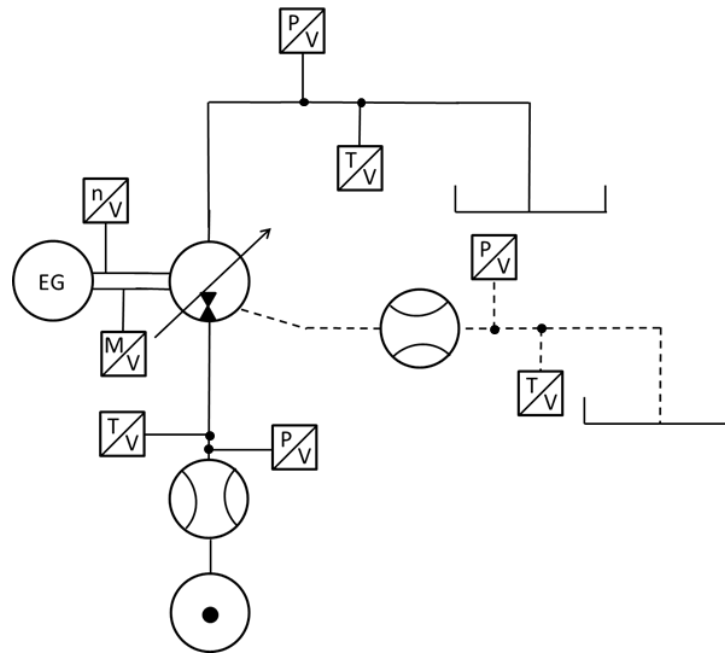


Figure 4.3. Baseline motoring mode test set up.

The results of the measured data for the pumping mode operating conditions are shown in Table 4.8. Again the case follows that the measured operating conditions that are later to be simulated are numbered 12-15 while those labeled E-H were only measured and not considered in the simulation study. These operating conditions were chosen in order to represent the motoring mode of the machine. This is important to

consider in order to show that the machine is still capable of still running well under both modes of operation.

Table 4.7. Baseline motoring mode test procedure.

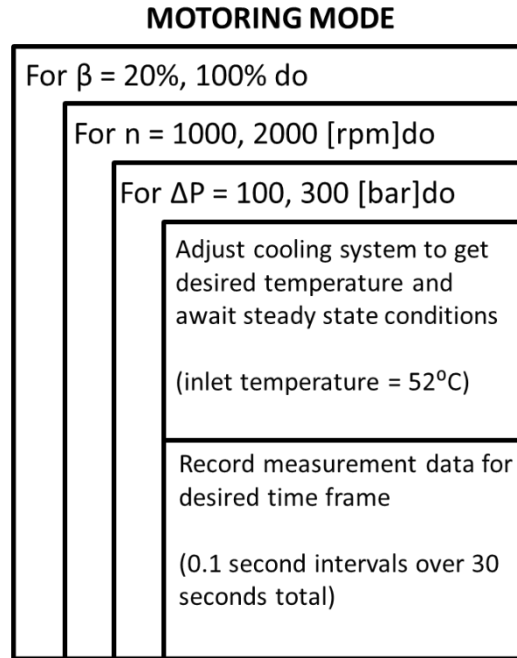


Table 4.8. Baseline motoring mode measured results.

Operating Condition - Motoring ($\beta = 100\%$)	12	13	14	15	Unit
High Pressure	150	275	150	275	bar
Low Pressure	50	50	50	50	bar
Angular Speed	1000	1000	2000	2000	rpm
Case Temperature	55.90	58.69	60.66	65.92	°C
Temperature at High Pressure Port	52.40	52.45	52.20	52.93	°C
Temperature at Low Pressure Port	51.4	50.9	51.4	51.3	°C
Swash Plate Angle	17	17	17	17	°

Operating Condition - Motoring ($\beta=20\%$)	E	F	G	H	Unit
High Pressure	100	275	100	275	bar
Low Pressure	0.2	25	8.5	50	bar
Angular Speed	1000	1000	2000	2000	rpm
Case Temperature	55.06	61.76	59.00	64.40	°C
Temperature at High Pressure Port	52.35	52.59	52.70	52.23	°C
Temperature at Low Pressure Port	52.2	53.2	52.7	52.2	°C
Swash Plate Angle	3.4	3.4	3.4	3.4	°

Note that for motoring mode, due to the measurement set-up and the line losses, the low pressure measured was the lowest possible pressure that was achievable. For full displacement, the higher displacement of the motor results in higher flow meaning a higher low pressure maintained at 50 bar. For partial displacement, the low pressure increases also as the displacement increases due to the operating speed. Also, a pressure differential of 300 bar was not attainable based on a maximum high pressure of 275 bar that was limited by the torque of the electric motor.

4.2 Piston/Cylinder Surface Wear Measurements

Once the steady-state measurements were completed, the unit was disassembled and the wear profiles on the piston and the cylinder were measured on a profilometer (surface roughness measuring system) as shown in to be used as accurate inputs into the model. The specifications of the profilometer used are shown in Figure 4.4.



Figure 4.4. Profilometer.

Table 4.9. Profilometer specifications.

Manufacturer	Model	Measuring Range	Resolution
Mitutoyo	SJ - 500	$\pm 40\mu\text{m}$ (z-axis) $\pm 50\mu\text{m}$ (x-axis)	$0.001\mu\text{m}$ (z-axis) $0.05\mu\text{m}$ (x-axis)

To measure the wear on the surface of the piston, it was necessary to take two traces, one from the case side and one from the DC side, since the piston gap length is longer than the measuring range of the profilometer. In post-processing, these two traces were combined to obtain a complete wear surface profile for the piston. This process was repeated eight times for each piston and an average was taken for a 2D surface profile representation as an input into the model. This process is shown in Figure 4.5.

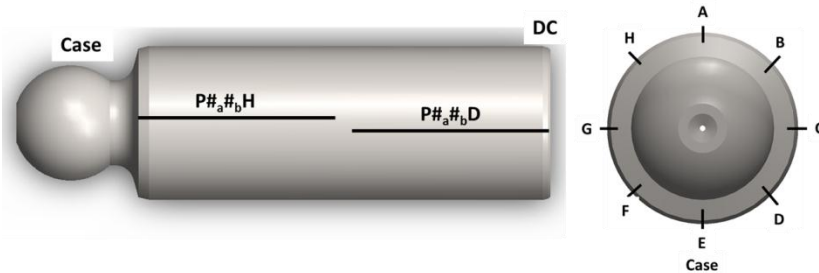


Figure 4.5. Piston wear profile measurement procedure.

To measure the wear on the bushing surface, only one trace was necessary since the length of the bushing is within the measuring range of the profilometer. Nine traces were measured for each bushing and then post-processed into a 3D surface profile representation as an input into the model. This process is shown in Figure 4.6. To ensure repeatability and accuracy the entire block is rotated as the same trace for each bushing is taken sequentially in which the process is then repeated for each trace location.

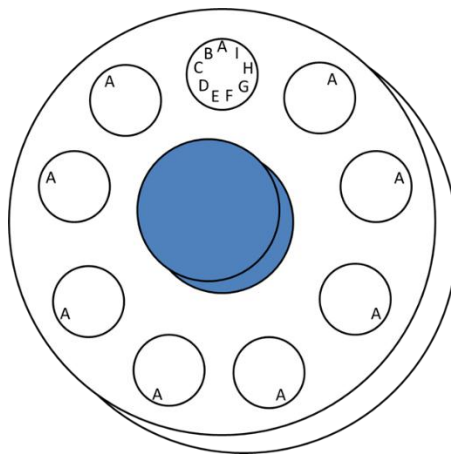


Figure 4.6. Bushing wear profile measurement procedure.

The following figures show the 9 piston and 9 bushing 3D wear surface profiles. Note that although each wear profile is slightly different, the model only considers one of these piston/bushing combinations in which an average among the 9 was chosen for simulation.

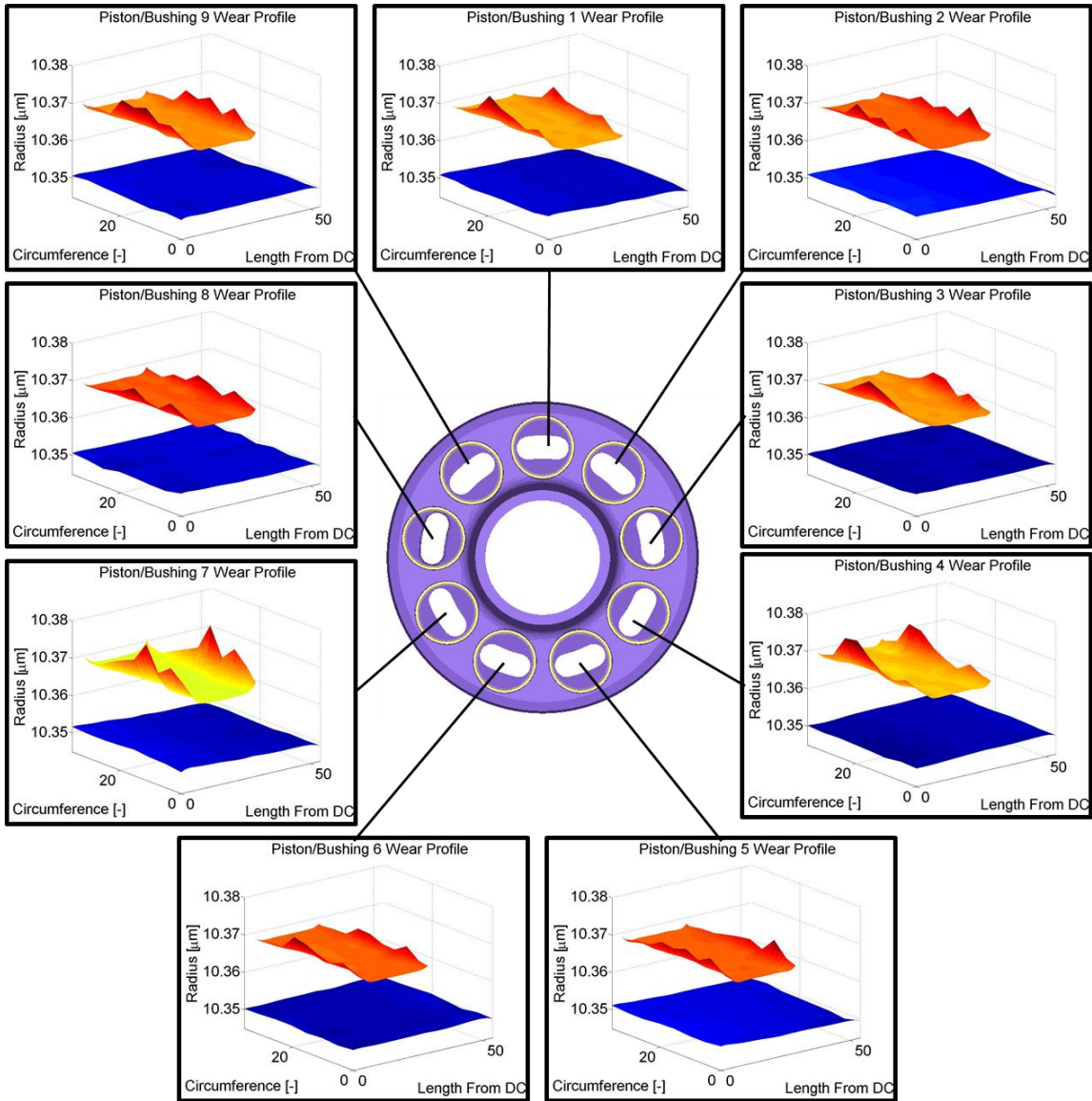


Figure 4.7. Piston/bushing wear profiles.

4.3 Baseline Simulation

In order to establish a reliable simulated baseline for comparison to the surface shaping study, simulations were done for the numbered measured operating conditions shown above as well as accounting for the same material and surface wear of the measured piston and bushing. These simulations were run for only the piston/cylinder interface; the other two interfaces, the slipper/swashplate and the block/valveplate, were not considered in simulation as this is not part of the focus of this research. The operating conditions that were simulated were chosen based on the commonality of the operating conditions, some of the corner operating conditions, and in both modes of the machine in order to capture the wide ranges that the machine is capable of while limiting the number of simulations to be considered in the interest of time and computational expense. Also, in the numerical model, a single piston/cylinder segment is considered over one shaft revolution and based on reciprocating motion, the losses are then multiplied by the number of pistons in the unit; in this case 9. It is important to note that although this is the case, the numerical model still considers the entire block in order to account for the effects of neighboring bores on the displacement chamber pressure in respect to the reference piston and cylinder segment.

4.3.1 Boundary conditions

The boundary conditions of the interface specified to the model are very important in solving the Reynolds equation along with the pressure and thermal elastic deformations of the solid bodies. The boundary conditions are chosen such to accurately reflect the real world external environment experienced by the solid bodies to be analyzed. The pressure and thermal boundary conditions utilized in the following micro-surface shaping study on the piston are detailed below.

Considering both the piston and the cylinder for the pressure and thermal boundary conditions, an inertial relief constraint is considered. In the inertial relief method, the moving parts are not arbitrarily constrained in the actual situation; therefore in simulation an accelerating coordinate system is introduced based on the center of mass of the structure in which the applied loads, which are not in equilibrium, are balanced

based on generated translational and rotational accelerations. More details of this method can be found in Pelosi (2012).

4.3.1.1 Pressure Boundary Conditions

In the model, the pressure boundary conditions must be correctly defined in order to accurately calculate the iterative steps of the Reynolds equation that is directly connected to the lubricating film dynamic pressure field. For this interface an influence method scheme is implemented in concerns of simulation time. The pressure elastic deformation of the solids are calculated based on the dynamic loading conditions applied to the influence matrix created from a mesh with the boundary conditions such as the for the micro-surface shaping study shown in Figure 4.8

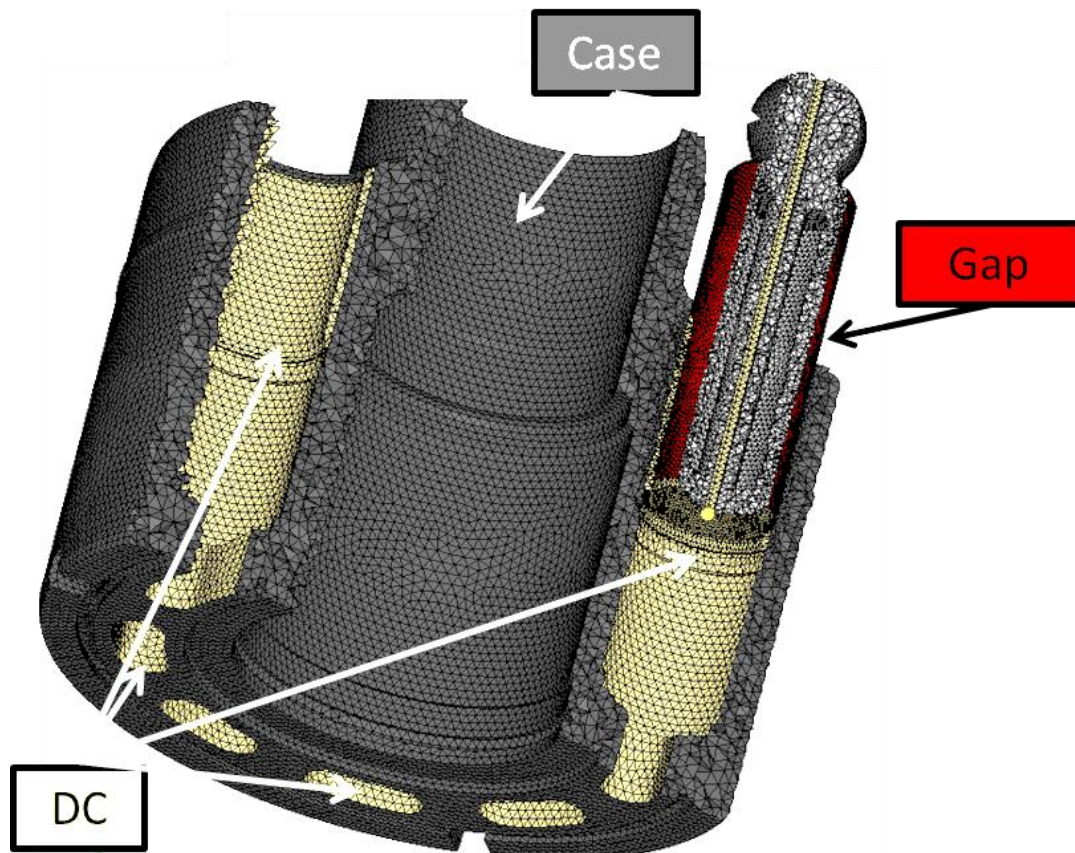


Figure 4.8. Piston/cylinder interface pressure boundary conditions to define IMs.

4.3.1.2 Pressure Profiles

The instantaneous displacement chamber pressure profile considered for the pressure boundary conditions as shown above were first simulated as inputs into the gap simulation based on the geometry of the valveplate connecting the chamber to the ports and the average measured high and low pressures. These are shown below for each operating condition simulated. As can be seen, the speed and the displacement only have a slight effect on the profile as the temperatures and the motion of the piston slightly changes. The change in operating pressure changes the magnitude of the profile, but the shape again remains very similar due to the geometry of the valveplate. Motoring mode changes the profile drastically as the geometry of the valveplate changes with the opposite motion.

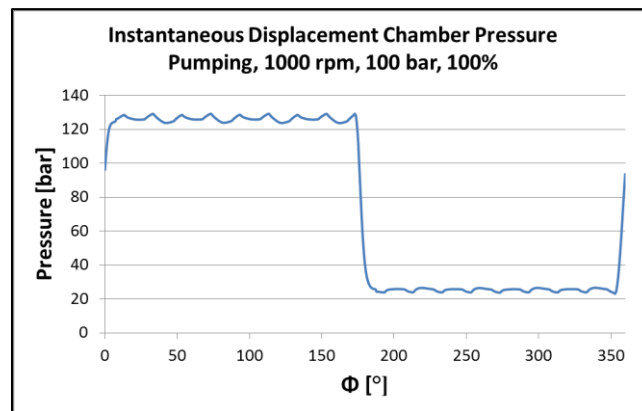


Figure 4.9. Baseline simulated instantaneous displacement chamber pressure for operating condition 1; pumping, 1000 rpm, 100 bar, 100%.

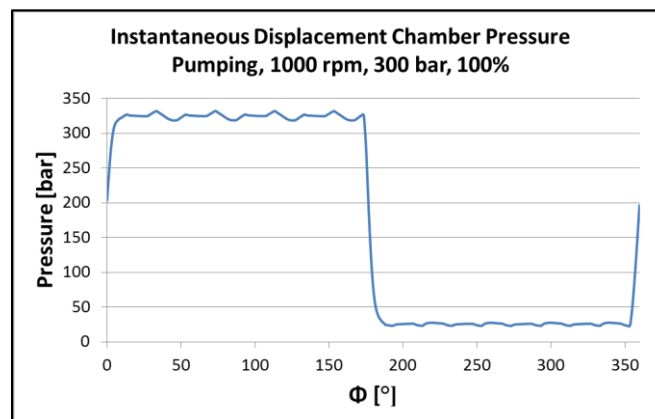


Figure 4.10. Baseline simulated instantaneous displacement chamber pressure for operating condition 2; pumping, 1000 rpm, 300 bar, 100%.

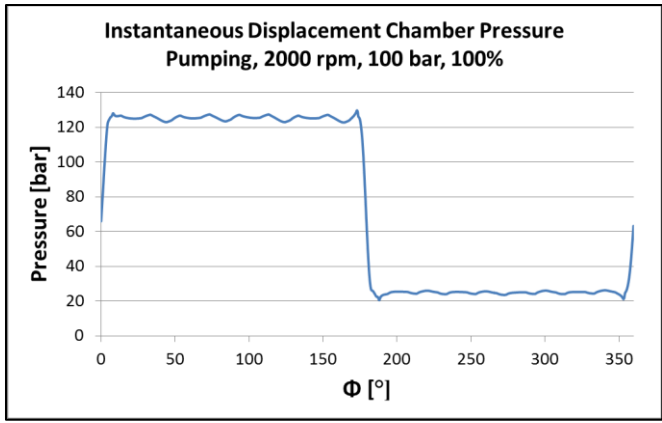


Figure 4.11. Baseline simulated instantaneous displacement chamber pressure for operating condition 3; pumping, 2000 rpm, 100 bar, 100%.

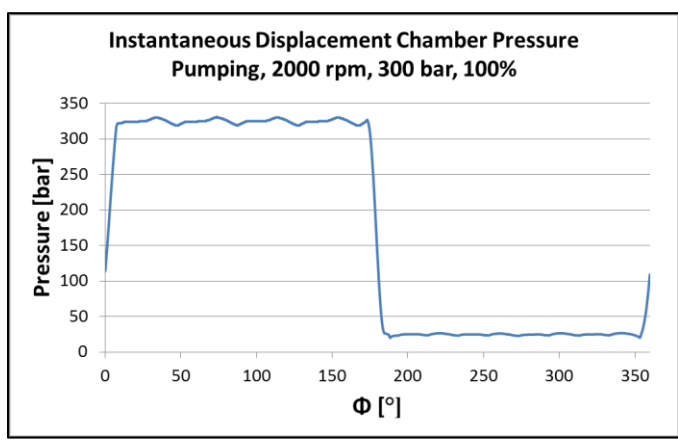


Figure 4.12. Baseline simulated instantaneous displacement chamber pressure for operating condition 4; pumping, 2000 rpm, 300 bar, 100%.

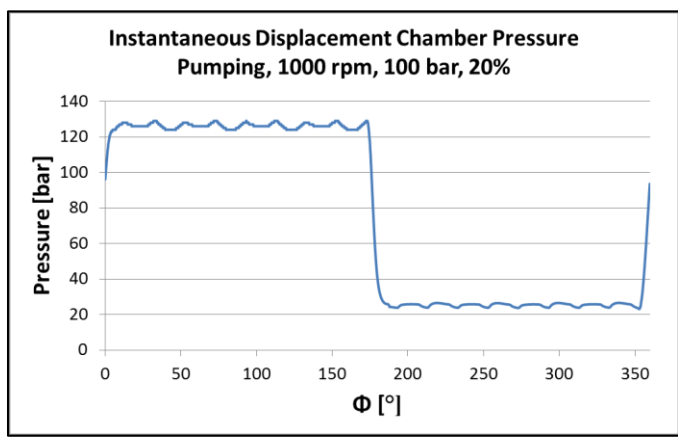


Figure 4.13. Baseline simulated instantaneous displacement chamber pressure for operating condition 5; pumping, 1000 rpm, 100 bar, 20%.

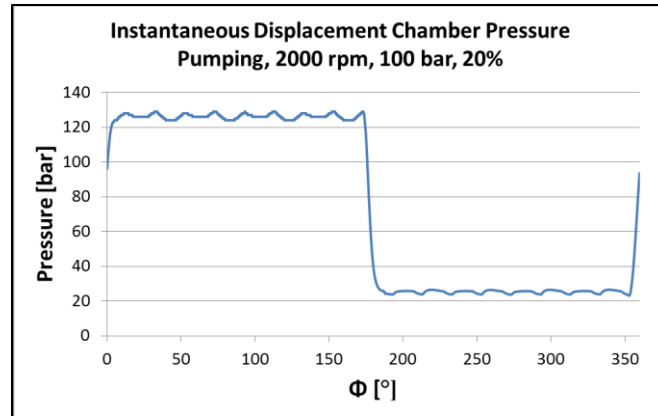


Figure 4.14. Baseline simulated instantaneous displacement chamber pressure for operating condition 7; pumping, 2000 rpm, 100 bar, 20%.

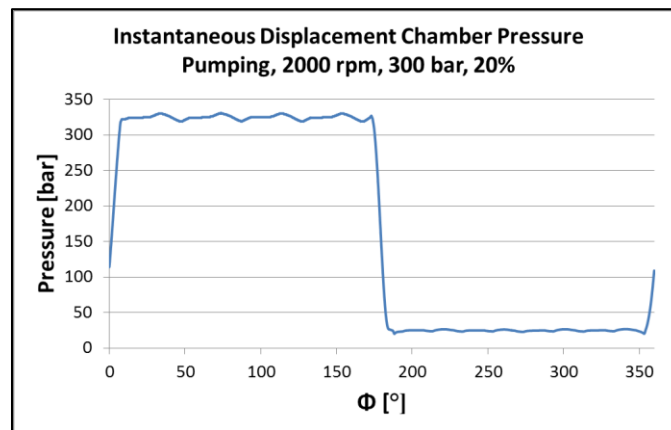


Figure 4.15. Baseline simulated instantaneous displacement chamber pressure for operating condition 8; pumping, 2000 rpm, 300 bar, 20%.

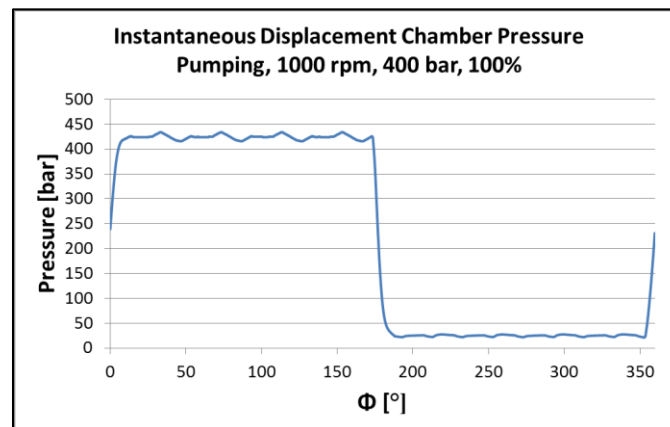


Figure 4.16. Baseline simulated instantaneous displacement chamber pressure for operating condition 9; pumping, 1000 rpm, 400 bar, 100%.

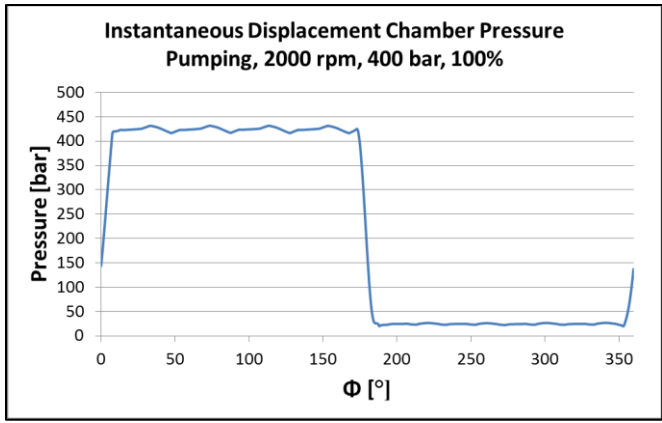


Figure 4.17. Baseline simulated instantaneous displacement chamber pressure for operating condition 10; pumping, 2000 rpm, 400 bar, 100%.

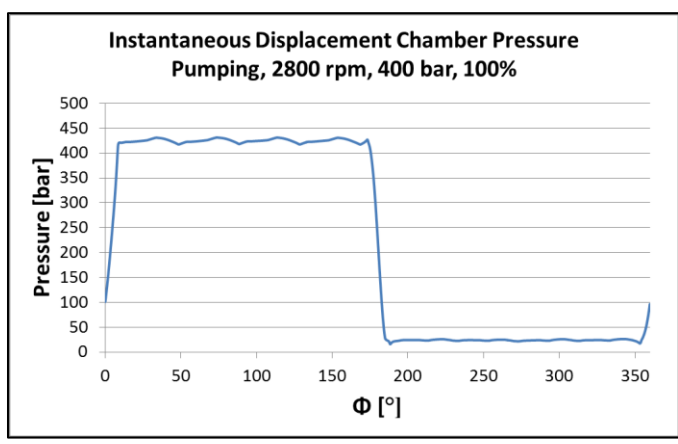


Figure 4.18. Baseline simulated instantaneous displacement chamber pressure for operating condition 11; pumping, 2800 rpm, 400 bar, 100%.

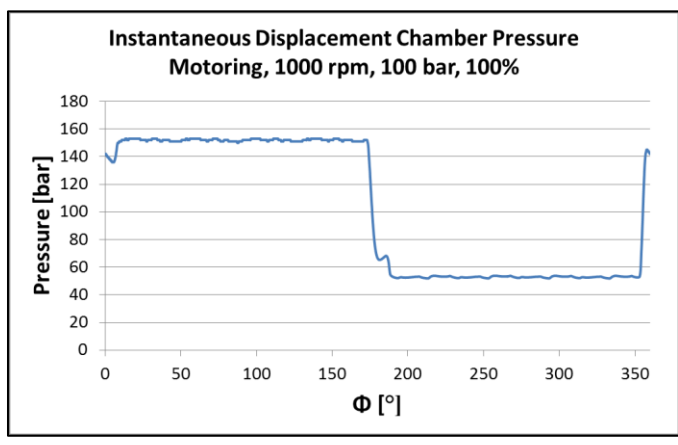


Figure 4.19. Baseline simulated instantaneous displacement chamber pressure for operating condition 12; motoring, 1000 rpm, 100 bar, 100%.

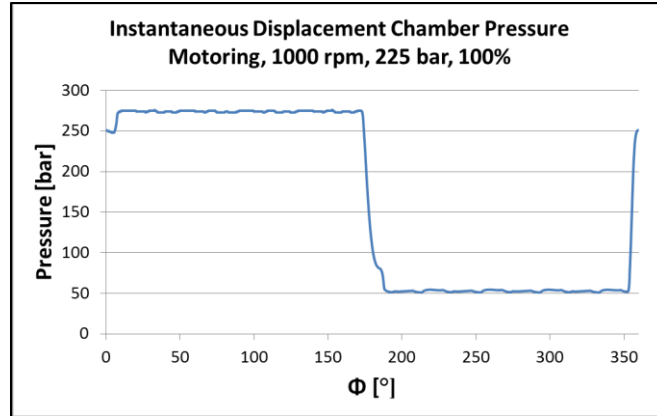


Figure 4.20. Baseline simulated instantaneous displacement chamber pressure for operating condition 13; motoring, 1000 rpm, 225 bar, 100%.

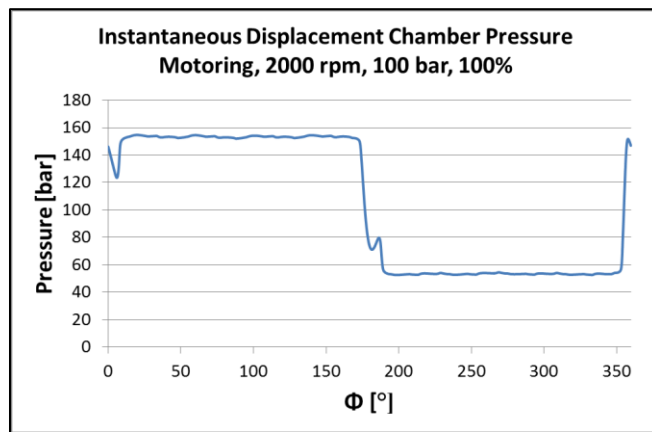


Figure 4.21. Baseline simulated instantaneous displacement chamber pressure for operating condition 14; motoring, 2000 rpm, 100 bar, 100%.

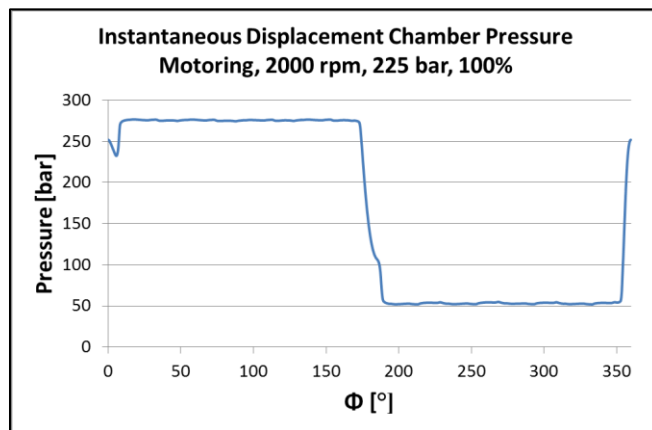


Figure 4.22. Baseline simulated instantaneous displacement chamber pressure for operating condition 15; motoring, 2000 rpm, 225 bar, 100%.

4.3.1.3 Thermal Boundary Conditions

The thermal boundary conditions are of a high significance to the accuracy of the model as well. The boundary conditions that are used for the micro-surface shaping study condition include:

- Neumann boundary: the surface has a set heat flux. A Neumann boundary condition is specified for the fluid film gap between the piston and the cylinder since the heat flux is known from the non-isothermal film flow calculation.

$$q_s = \frac{\lambda_{oil}}{\Delta \hat{z}_{film}} (T_{film} - T_s) \Delta t \quad (4.1)$$

- Mixed boundary: the temperature as measured (standard unit) along with an estimated convection coefficient from literature are specified. The temperature at the boundary cell is solved and bounded by its neighbors and the outer environmental conditions. A mixed boundary condition is applied to all external surface of the solid bodies.

$$q_s = \alpha_{Air} (T_{Air} - T_s) \Delta t \quad (4.2)$$

- Dirichlet boundary: a fixed boundary condition with a given temperature at the face. A Dirichlet boundary condition presents a strong influence on the resulting temperature field. This boundary condition is not applied in this study since it does not accurately represent any of the conditions occurring.

The boundary conditions for the piston and the cylinder are defined in Table 4.10 and shown in Figure 4.23.

Table 4.10. Piston/cylinder interface boundary conditions defined.

Boundary Conditions			
Face	Condition	h (W/m ² K)	T (°C)
Case	Mixed	1000	T _{case}
DC	Mixed	3000	(T _{HP} +T _{LP})/2
Air	Mixed	50	T _{ambient}

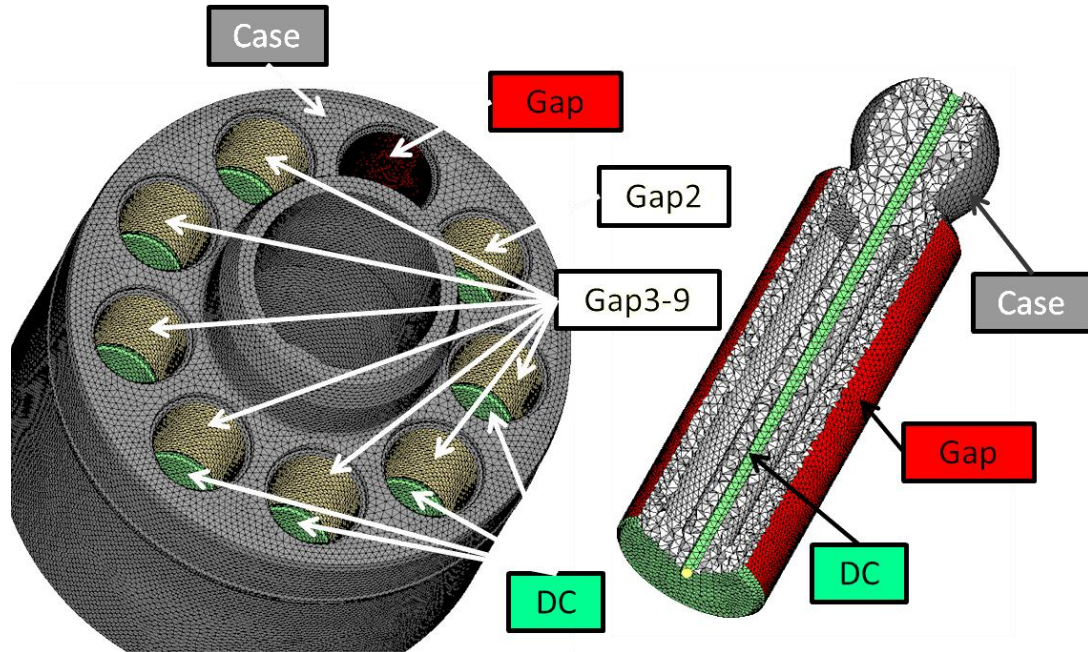


Figure 4.23. Piston/cylinder interface thermal boundaries conditions.

4.3.2 Simulation Baseline Results

The simulated baseline used for comparison is the same measured standard 75 cc stock piston/cylinder interface in which a measured wear profile on both the surface of the piston and the bushing after use of the machine is considered as shown in Figure 4.24. Measurements were taken on a steady state measurement test rig as previously described in order to use the measured temperatures as accurate inputs to the numerical model for the various operating conditions of the study.

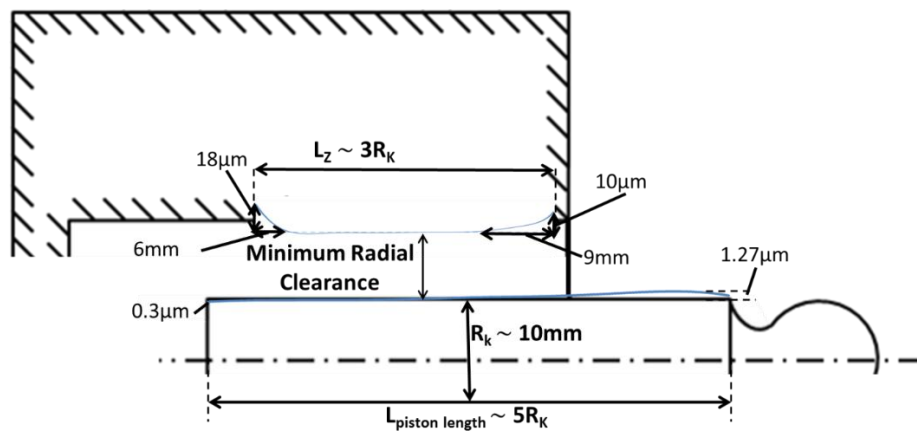


Figure 4.24. Measured wear profile of a used piston and cylinder.

The simulated losses, including the energy dissipation and the leakage, for the baseline at the various operating conditions are shown below in Figure 4.25 and Figure 4.26 respectively. Note that operating condition 6, 1000 rpm, 300 bar, 20% displacement is shown as zero in the following graphs considering the simulations did not numerically converge based on the large side contact that occurs.

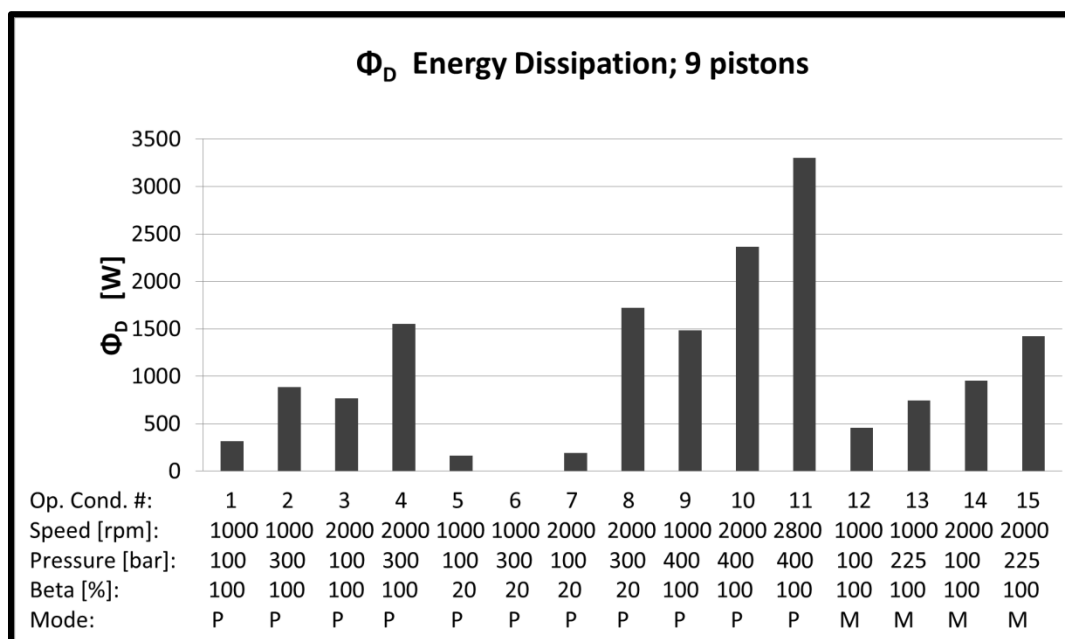


Figure 4.25. Baseline energy dissipation; piston/cylinder interface.

As expected, as the speed and pressure increase, the energy dissipation increases due to the increased side load. For partial displacement, the side load is greatly decreased causing the energy dissipation to also greatly decrease at the lower operating pressures. As for the partial displacement and higher operating pressure, the energy dissipation actually increases due to the large increase in leakage (shown below); the gap between the piston and the cylinder is more sufficient since the external forces on the piston are not as great in turn causing the piston to not squeeze against the bushing so much allowing for more fluid to leak out of the gap. The energy dissipation of pumping compared to motoring of the machine tends to be similar since the efficiency of the machine in both modes is similar.

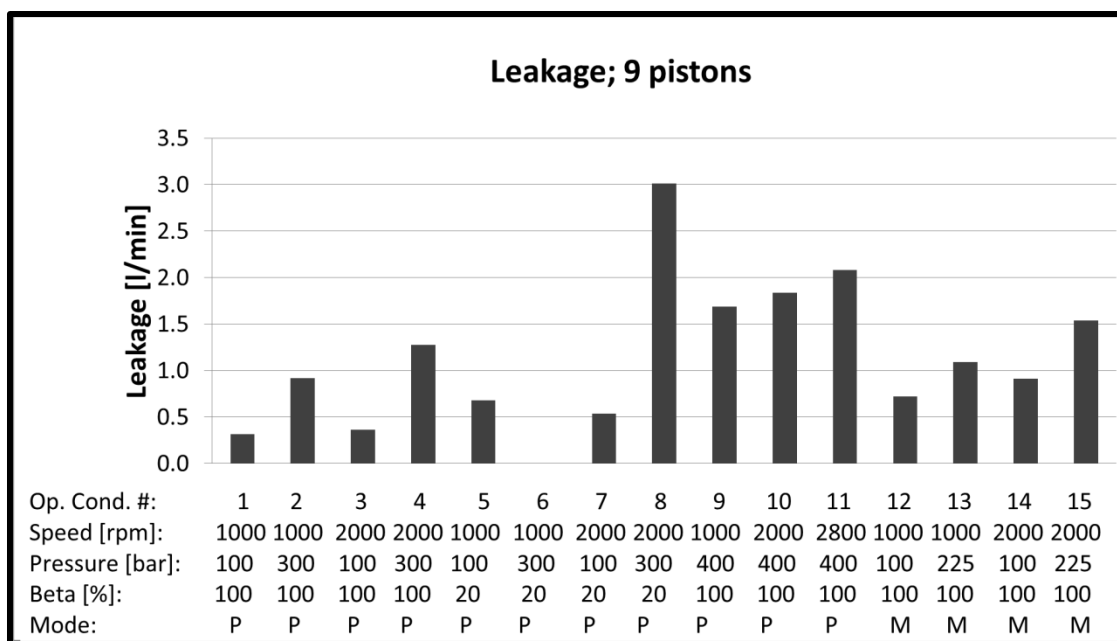


Figure 4.26. Baseline leakage; piston/cylinder interface.

When comparing the leakage among the various operating conditions, the speed has little effect on the results, while the increase in operating pressure results in an increase of leakage. The explanation for this is that the pressure in the DC is increased with the increased operating pressure forcing fluid to flow out of the gap between the piston and the cylinder at an increased rate. Even further as mentioned above, as the swash plate angle is decreased, the side load on the piston is less resulting in a more centered piston in the bore allowing for more leakage, especially as the operating pressure is increased. As for motoring, a similar trend again follows.

To further understand the phenomena occurring in the fluid film for a comparison, the multi-plots, shown in the following figures, show a contour plot of the fluid film thickness between the piston and the cylinder. Overlaid in red is the contact pressure that is occurring due to critically low to no fluid film between the piston and the cylinder; this contact pressure is saturated to 2880 bar based on the yield strength of the material. Depicted in blue is the fluid pressure in the gap that supports the external loads. Shown in the multi-plots are 45^o steps through the high pressure stroke of a revolution, 0^o-180^o. In the consideration of motoring mode, the numerical analysis continues to consider the

high pressure stroke first in which the motion of the piston is rather changed. The plots are shown in comparison for operating condition 3,4 (increasing pressure), 8 (decreasing displacement), 11 (increasing speed and pressure), and 15 (motoring mode).

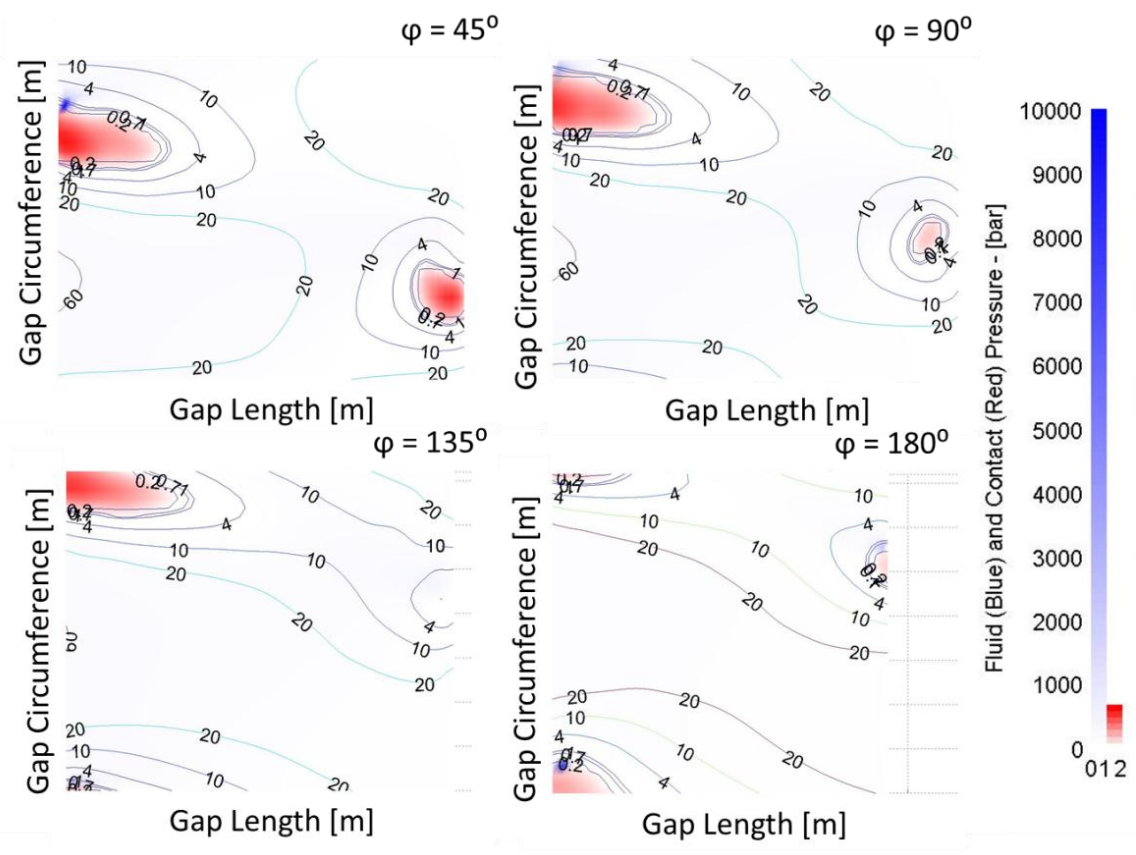


Figure 4.27. Baseline multi-plot, operating condition 3; 2000 rpm, 100 bar, 100%.

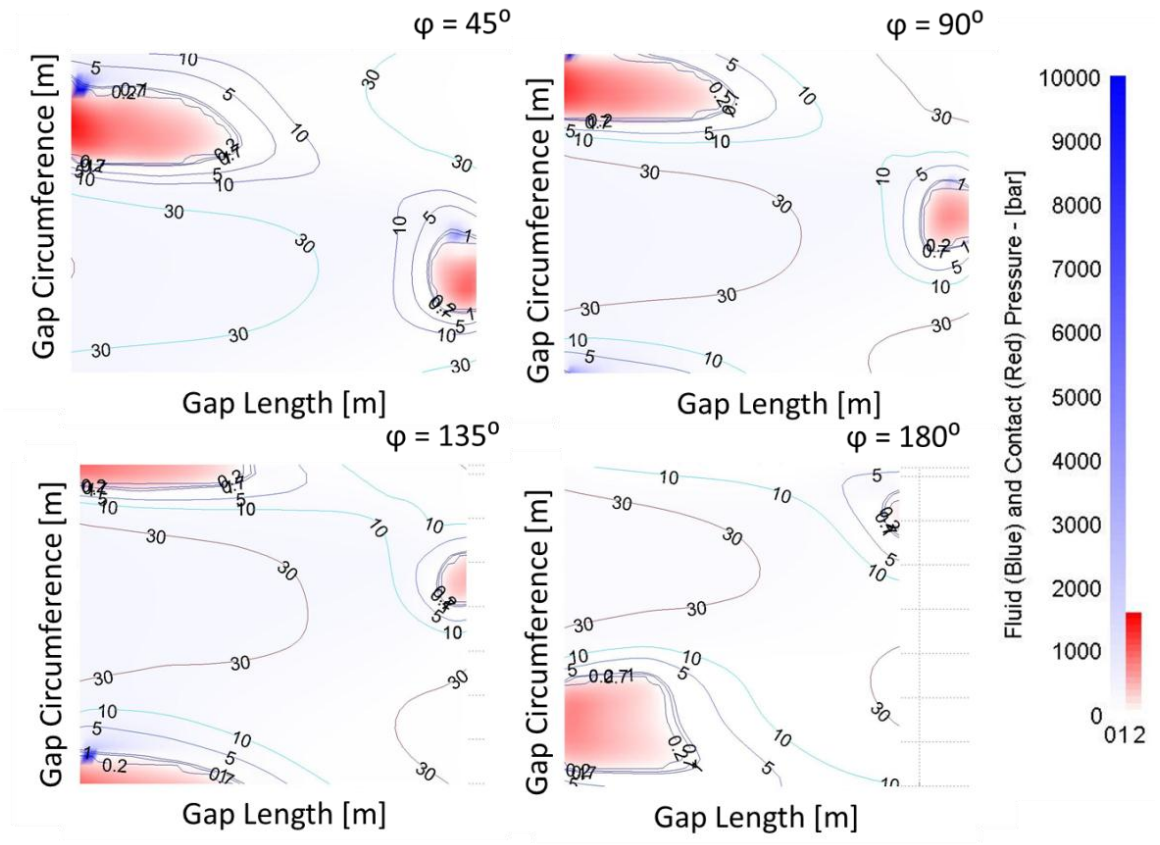


Figure 4.28. Baseline multi-plot, operating condition 4; 2000 rpm, 300 bar, 100%.

As the operating pressure increases from operating condition 3 (100 bar) to operating condition 4 (300 bar) the areas of critical minimum fluid film thickness increases along with the contact pressure. This is due to the increased external loads on the piston along with the deformations of the solid bodies.

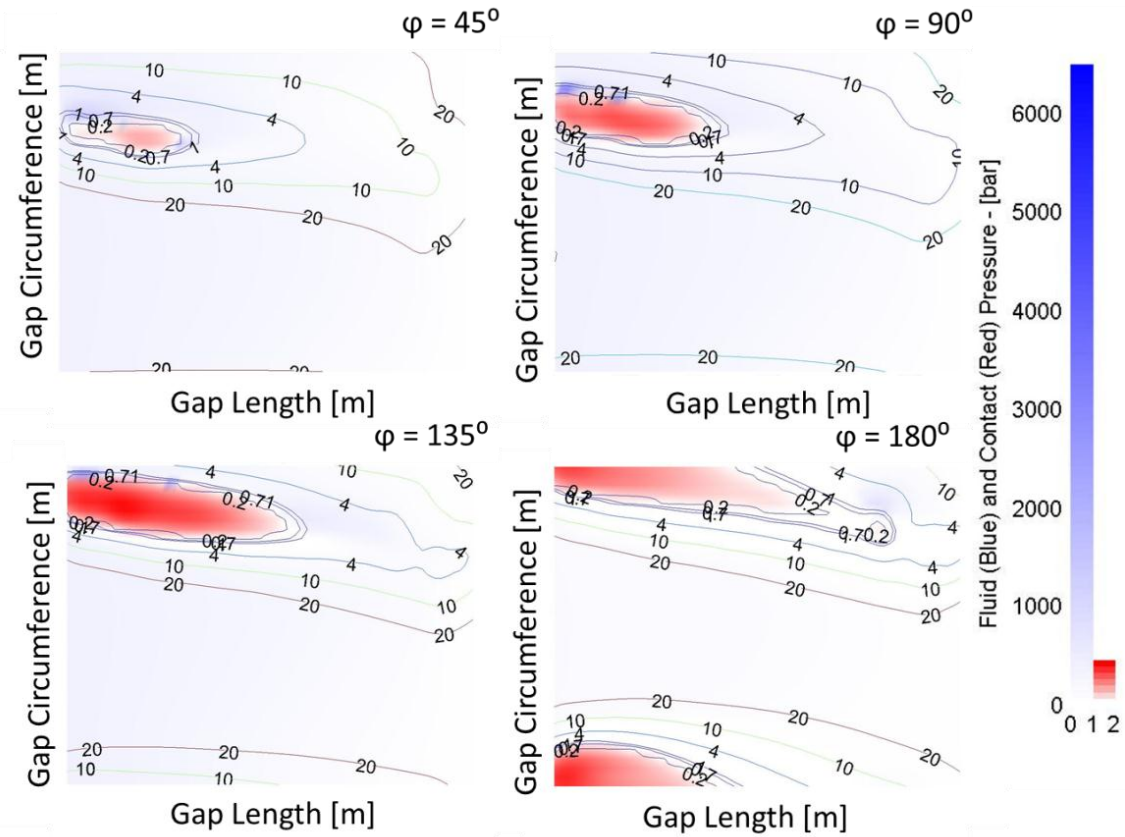


Figure 4.29. Baseline multi-plot, operating condition 8;
2000 rpm, 300 bar, 20%.

As the displacement is decreased in operating condition 8 (20% beta) from operating condition 4 (100% beta) the contact pressure and the fluid pressure is reduced due to the decrease in side load. This then results in the piston being less inclined in the bore and without the fluid support, the piston tends to scrape along the bushing causing the areas shown. This in turn allows the fluid to leak from the large fluid film thickness created on the opposing circumferential side of the gap.

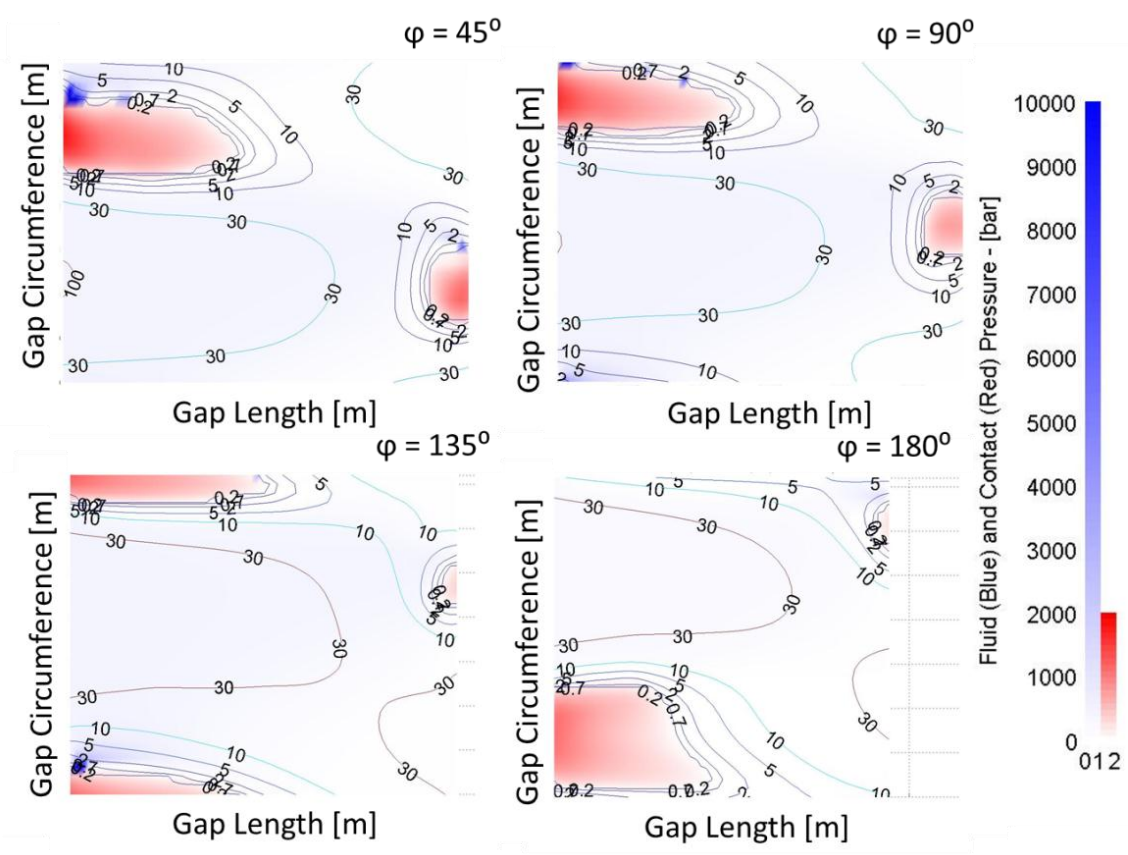


Figure 4.30. Baseline multi-plot, operating condition 11; 2800 rpm, 400 bar, 100%.

By even further increasing the pressure along with the speed from operating condition 4 (2000 rpm, 300 bar) to operating condition 11 (2800 rpm, 400 bar) it is shown that the areas of minimum fluid film thickness remain similar, but the contact pressure is slightly increased. Since the increase in speed does not have a large impact on the motion of the piston, this slight increase is due mainly to the increase in pressure.

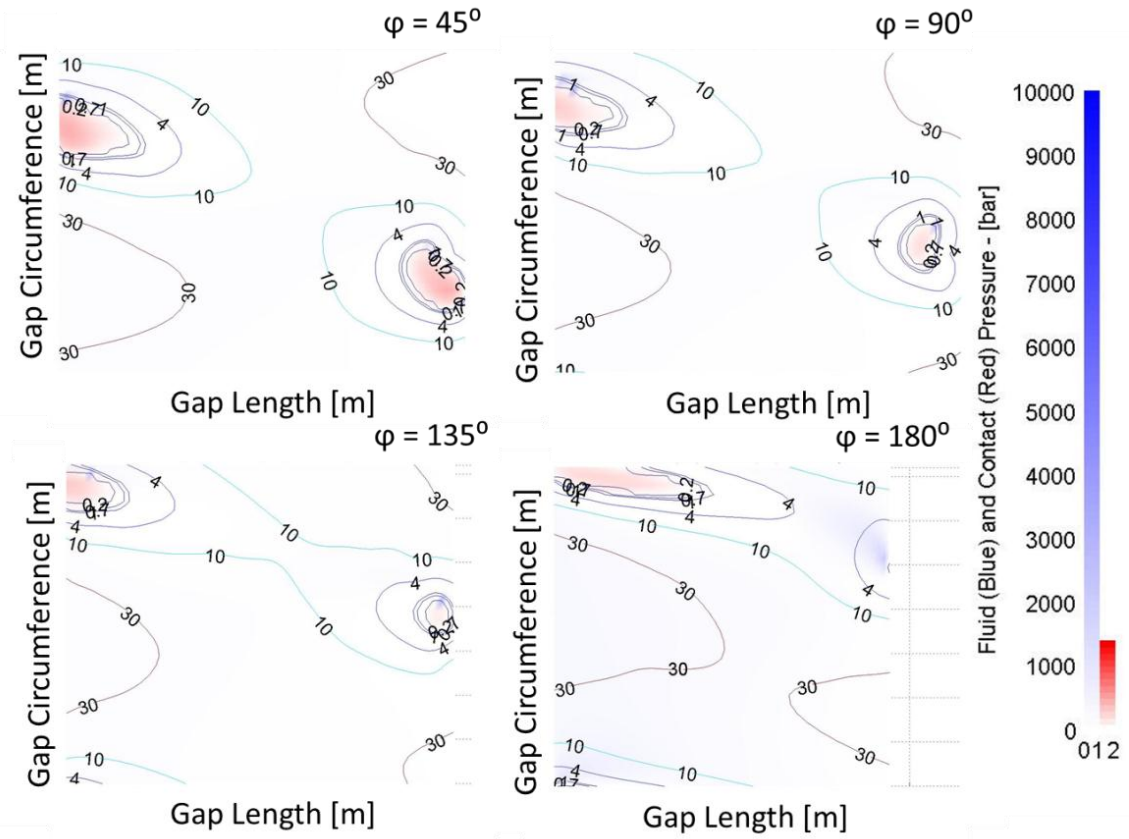


Figure 4.31. Baseline multi-plot, operating condition 15; motoring, 2000 rpm, 225 bar, 100%.

By switching the operating mode of the machine from operating condition 4 (pumping) to operating condition 15 (motoring) the critical minimum gap heights tend to occur in similar locations and with similar contact pressures; however, the areas are reduced, consequently the increase in leakage yet the decrease in energy dissipation. This also slightly depends on the reduction in pressure based on the measuring capabilities.

Furthermore, shown below are the axial friction forces of the piston over one shaft revolution (Figure 4.32-Figure 4.36). The coordinate system in which the axial friction forces are considered is shown in Figure 2.4; the positive z-axis is in the direction of motion of the piston as it moves out of the bore.

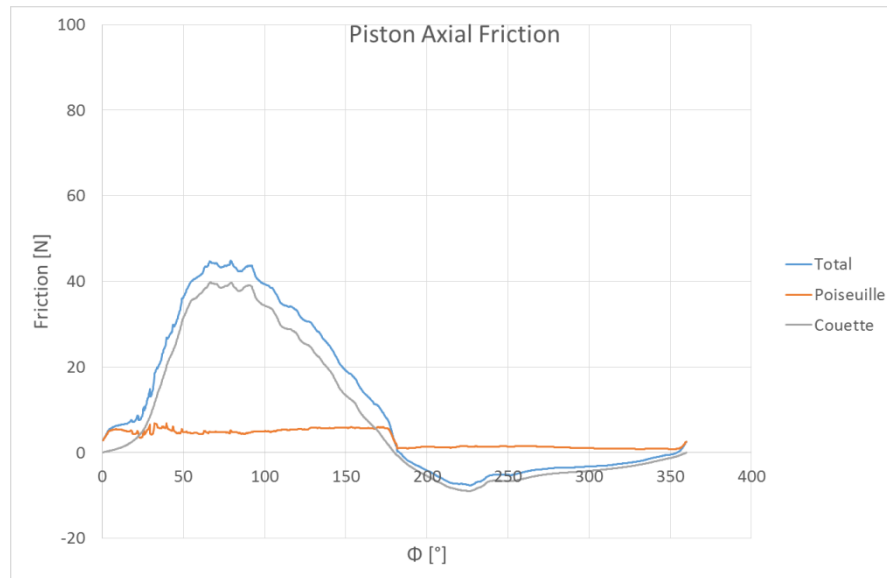


Figure 4.32. Baseline piston axial friction, operating condition 3; 2000 rpm, 100 bar, 100%.

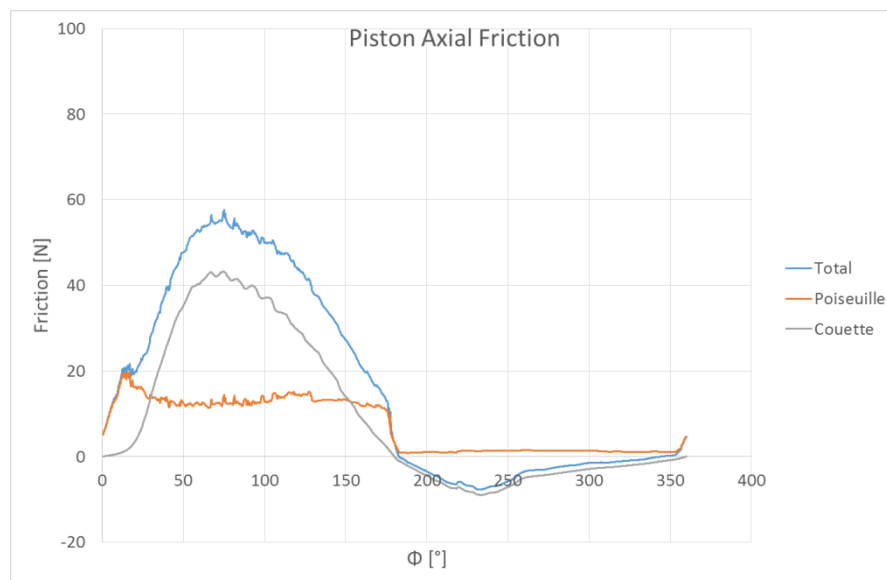


Figure 4.33. Baseline piston axial friction, operating condition 4; 2000 rpm, 300 bar, 100%.

As the operating pressure increases from operating condition 3 (100 bar) to operating condition 4 (300 bar) the axial friction forces also increase due to the increased side loads and deformations.

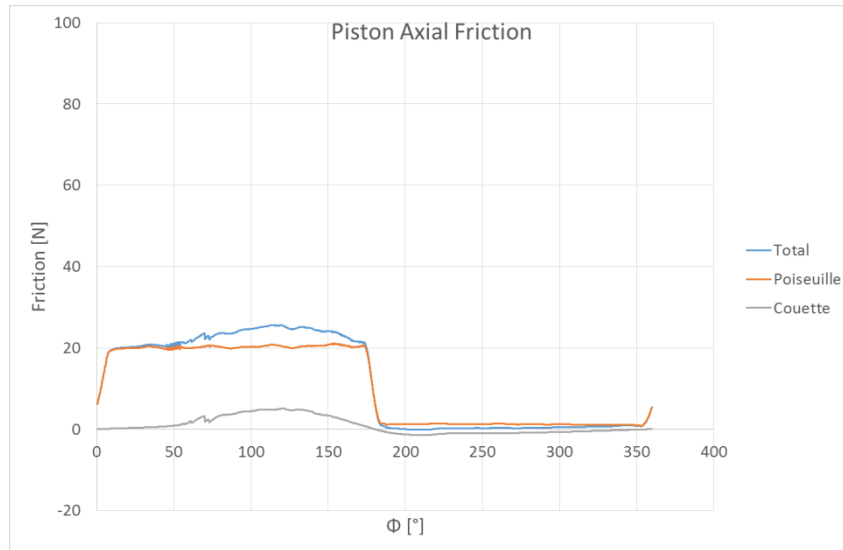


Figure 4.34. Baseline piston axial friction, operating condition 8; 2000 rpm, 300 bar, 20%.

As the displacement decreases from operating condition 4 (100% beta) to operating condition 8 (20% beta) the axial friction forces acting on the cylinder decrease drastically due to the drastic decrease in the side loads as previously explained. This means that although the torque losses are decreased, it was shown that the leakages are greatly increased in which the energy dissipation is in turn slightly increased.

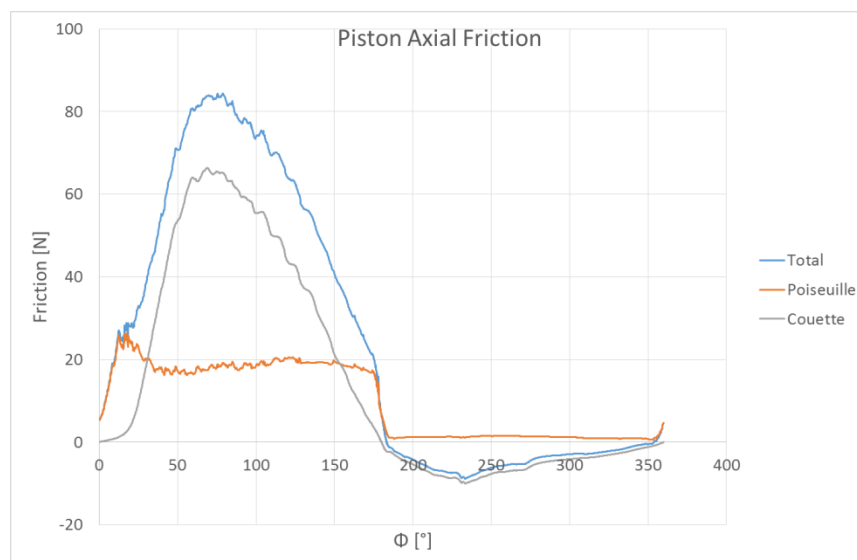


Figure 4.35. Baseline piston axial friction, operating condition 11; 2800 rpm, 400 bar, 100%.

As the speed and pressure increase from operating condition 4 (2000 rpm, 300 bar) to operating condition 11 (2800 rpm, 400 bar) the piston axial friction forces further increase with the further increase in pressure; the torque loss aiding the increased leakage in the largely increased energy dissipation.

As can be seen in pumping mode throughout the operating conditions shown, as the piston moves into the bore in the negative direction during the high pressure stroke, the couette component of the friction force opposes this motion resulting in a positive friction force. In this case the poiseuille component aids the couette component and results in a larger total friction force.

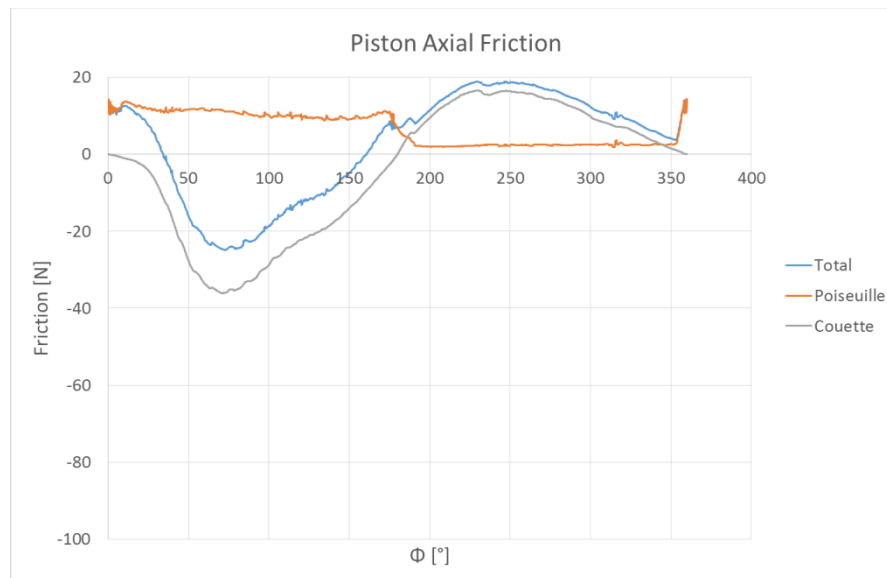


Figure 4.36. Baseline piston axial friction, operating condition 15; motoring, 2000 rpm, 225 bar, 100%.

As the mode of operating changes from operating condition 4 (pumping) to operating condition 15 (motoring) the axial friction forces acting on the cylinder are decreased due to the decrease in critical minimum fluid film thickness as shown above. So in this case, although the leakage slightly increases, the torque losses are decreased and therefore the decrease in energy dissipation is reflected. Based on the coordinate system as described above, since the couette friction force component is opposing the motion of the piston, it is negative in the high pressure stroke since the motion of the piston is in the positive direction in motoring mode. In this case the poiseuille

component is actually opposing the couette component in the high pressure stroke resulting in a reduced total friction force.

Shown below is the fluid film based on the deformations of the solid bodies due to the pressure (left) and thermal (right) loading for various operating conditions simulated for the baseline. The deformations are shown below are considered half way through the high pressure stroke ($\phi = 90^\circ$).

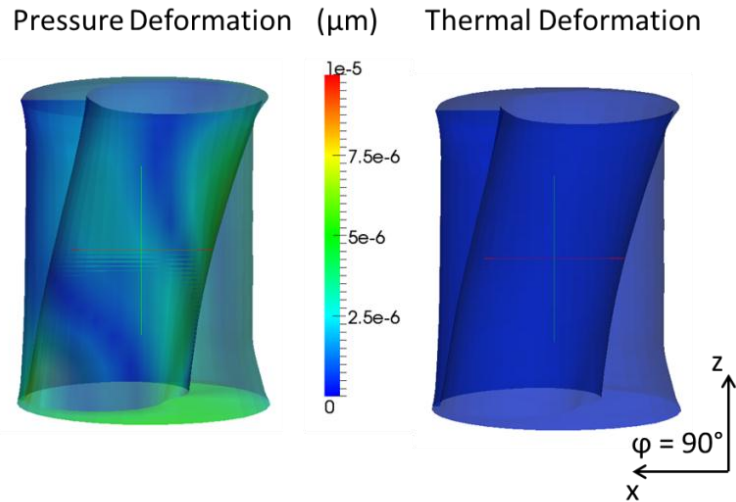


Figure 4.37. Baseline piston/cylinder deformation, operating condition 3; 2000 rpm, 100 bar, 100%.

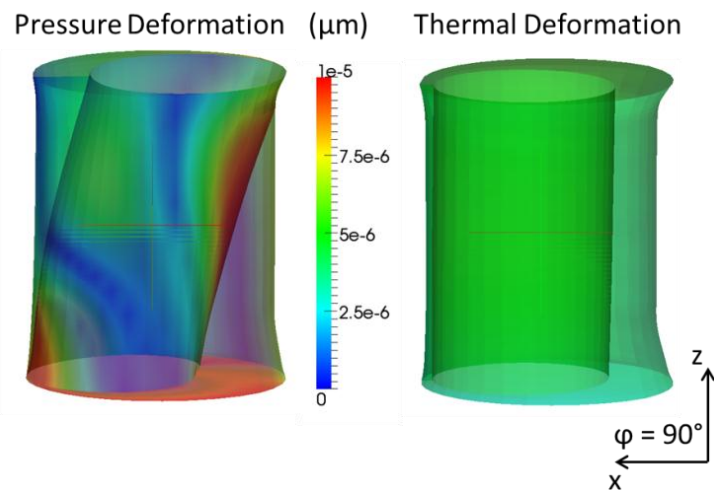


Figure 4.38. Baseline piston/cylinder deformation, operating condition 4; 2000 rpm, 300 bar, 100%.

As the operating pressure increases from 100 bar to 300 bar, as expected the pressure deformations also increased while the motion of the piston remains similar. Also, since the case pressure is increased the magnitude of the thermal deformations are also increased.

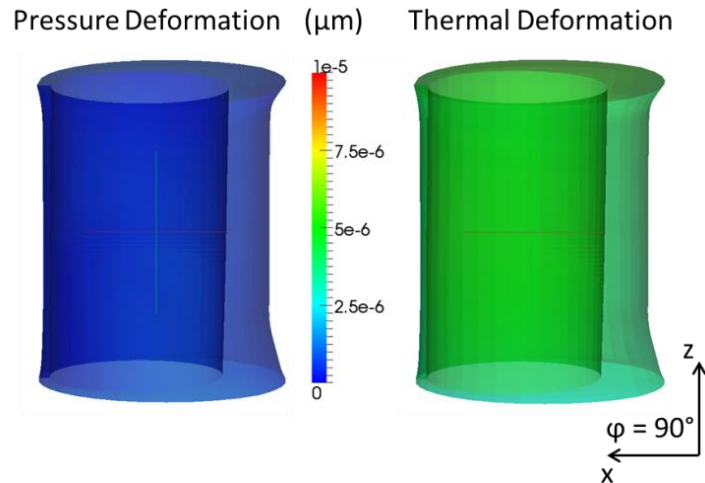


Figure 4.39. Baseline piston/cylinder deformation, operating condition 8; 2000 rpm, 300 bar, 20%.

At partial displacement, the pressure deformations are greatly reduced, but the case temperature remains similar and therefore the deformation due to the thermal loading is very similar.

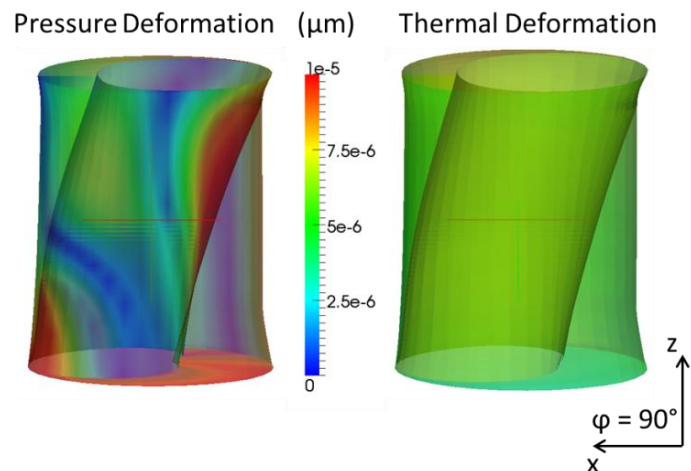


Figure 4.40. Baseline piston/cylinder deformation, operating condition 11; 2800 rpm, 400 bar, 100%.

As the speed and pressure are further increased, the pressure and thermal loading is increased and therefore the deformations are also larger as expected.

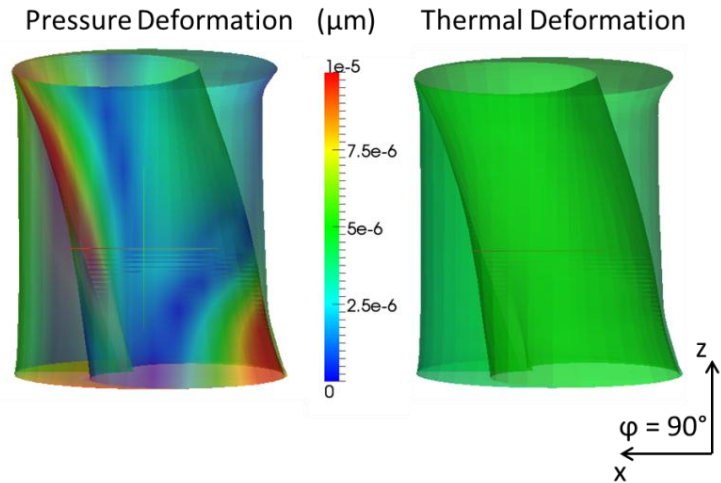


Figure 4.41. Baseline piston/cylinder deformation, operating condition 15; motoring, 2000 rpm, 225 bar, 100%.

The magnitude of the deformations of the solid bodies in motoring mode is very similar to that of the pumping mode. The difference is the motion of the piston is reversed at this time step of the revolution as is how the numerical model calculates the change in operation.

The inclination angle of the piston within the cylinder bore is also shown to better understand the effects on the leakage (Figure 4.43-Figure 4.47). The inclination angle is further described in Figure 4.42 in which it is the angle between the axis of the cylinder and the axis of the piston.

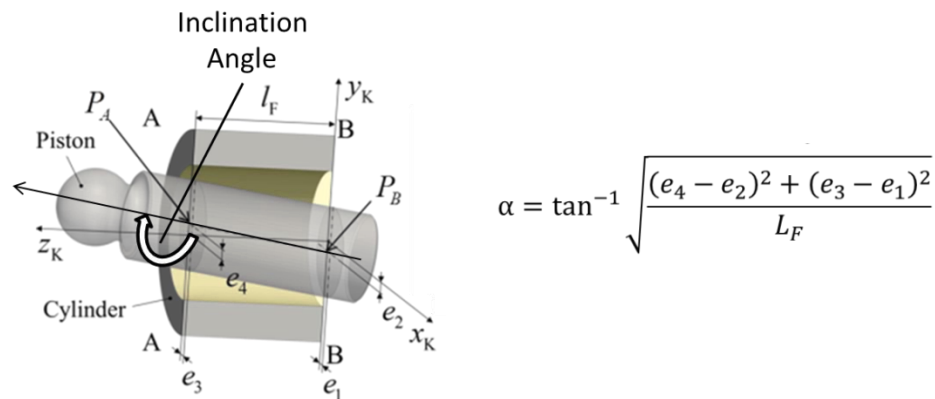


Figure 4.42. Inclination angle description.

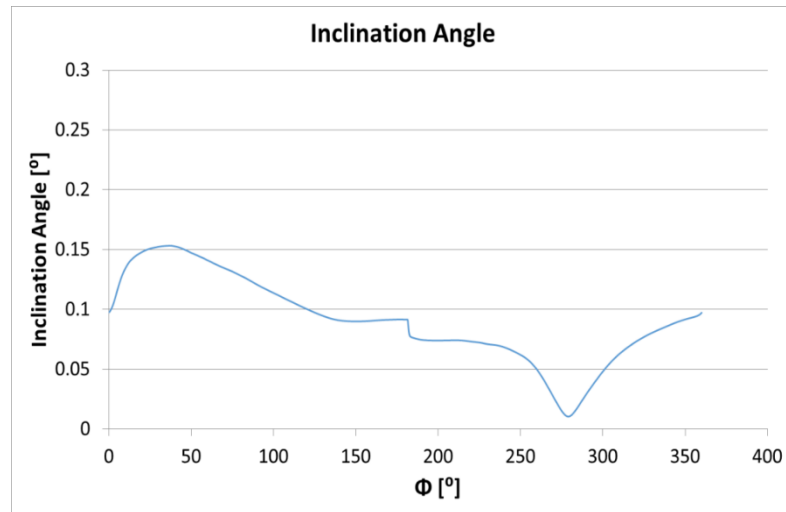


Figure 4.43. Baseline inclination angle, operating condition 3; 2000 rpm, 100 bar, 100%.

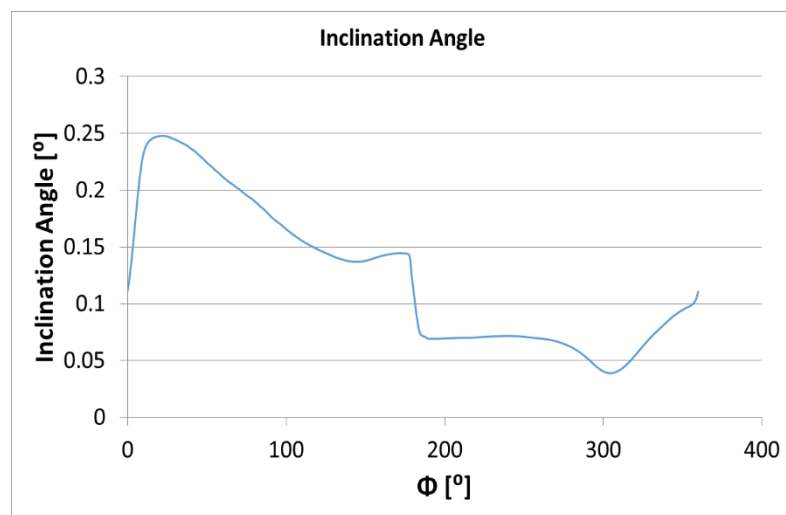


Figure 4.44. Baseline inclination angle, operating condition 4; 2000 rpm, 300 bar, 100%.

As the operating pressure increases from operating condition 3 (100 bar) to operating condition 4 (300 bar) the inclination of the piston also increases. This is again due to the increase in elastic pressure deformations experienced by the solid bodies and also the side load on the piston that causes it to tilt more within the bore.

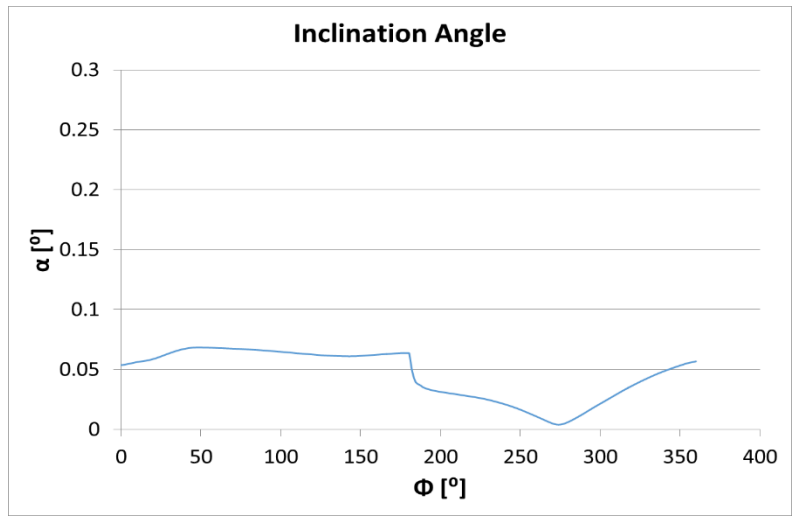


Figure 4.45. Baseline inclination angle, operating condition 8; 2000 rpm, 300 bar, 20%

As the displacement decreases from operating condition 4 (100%) to operating condition 8 (20%) the inclination of the piston severely decreases. This is again due to the large decrease in the external forces acting on the piston in turn causing the piston to remain relatively flat in reference to the side of the bore. This is also the reason for the much larger leakage shown at this operating condition; a larger pressure results in pushing the fluid out of the gap while the low displacement angle allows for a larger area between the piston and the cylinder for flow.

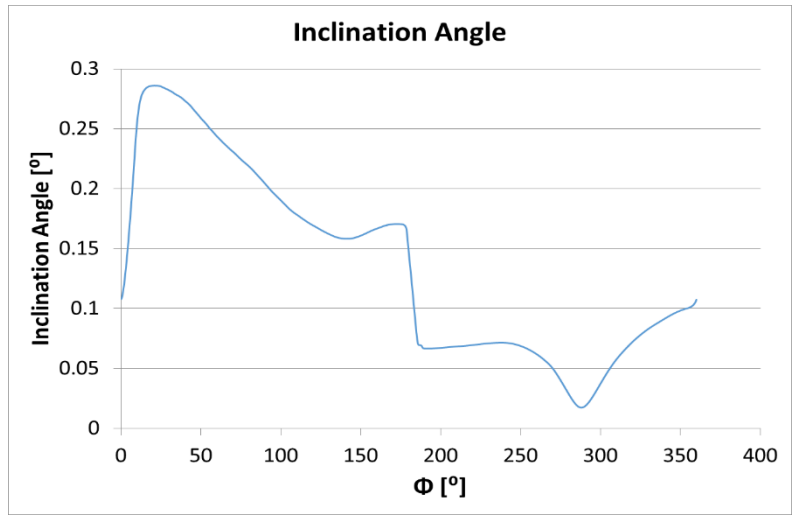


Figure 4.46. Baseline inclination angle, operating condition 11; 2800 rpm, 400 bar, 100%.

As the operating speed and pressure increases from operating condition 4 (2000 rpm, 300 bar) to operating condition 11 (2800 rpm, 400 bar) the inclination of the piston additionally increases as formerly explained for the pressure increase between operating conditions 3 and 4.

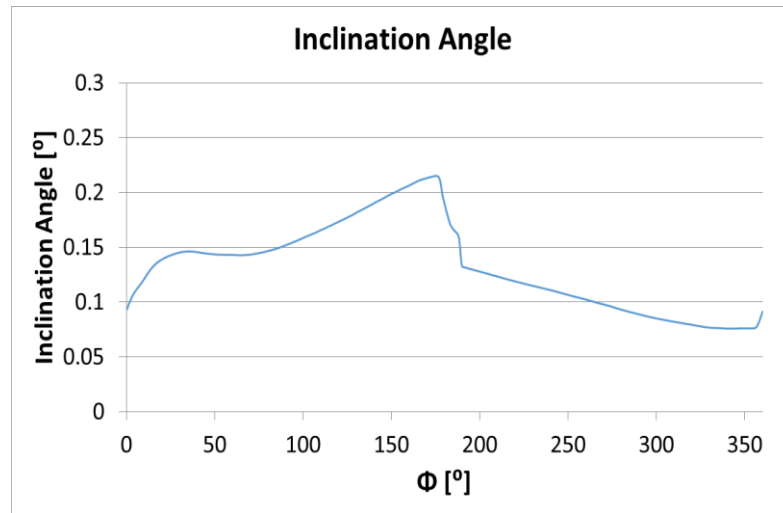


Figure 4.47. Baseline inclination angle, operating condition 15; motoring, 2000 rpm, 225 bar, 100%.

As the mode of operation changes from operating condition 4 (pumping) to operating condition 15 (motoring) the inclination angle decreases in the high pressure stroke due to the previously explained reasons.

4.4 Code Verification

In order to verify the simulation results for both the baseline and the piston surface shaping study to follow, simulated results are compared to measurements; detailed in the following section, this is done through measurements on the Tribo test rig (Lasaar, 2003) compared to simulation with the fluid structure interaction model.

4.4.1 Tribo Test Rig

The tribo test rig, shown in Figure 4.48, measures the axial and tangential friction forces acting on the cylinder surface due to the relative motion of the piston in an axial piston machine utilizing a three axis piezoelectric force sensor that is connected to the

bushing via a lever arm (Lasaar, 2003). The instantaneous displacement chamber pressure is also measured utilizing a piezoelectric pressure sensor.



Figure 4.48. The tribo test rig.

This test pump replicates the behavior of a nine piston axial piston pump with a rotating cylinder block and stationary swash plate. Figure 4.49 shows the design of how this behavior is replicated. There are only three main corresponding pistons in the block while five other pistons, located on the blocks outer circumference, are used to balance the external forces. One of these main corresponding pistons moves in a hydrostatically balanced bushing that is disconnected from the cylinder block. The friction forces exerted on this bushing are conveyed through the lever to the connected sensor. The oversized cylinder block allows for the housing of the force measurement system. This test pump has a fixed swash plate angle of 17° . A telemetry system on the test rig allows the transfer of the data from the sensor signals of the rotating group to a data acquisition system.

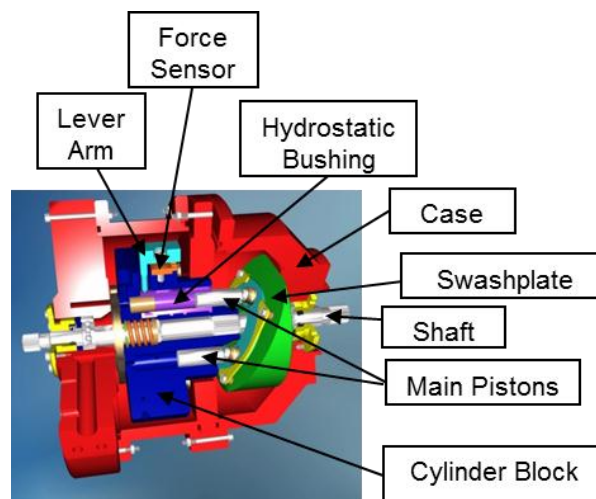


Figure 4.49. The tribo test rig pump assembly.

4.4.2 Input Parameters

For comparison to measurement purposes, numerical analysis was performed for three operating conditions in correspondence with the measurements taken by Rolf Lasaar. These operating conditions are presented in Table 4.11.

Table 4.11. Tribo measured and simulated operating conditions

Operating Condition	1	2	3	Unit
High Pressure	80	120	150	bar
Low Pressure	19.3	19.2	19.2	bar
Angular Speed	800	800	800	rpm
Case Temperature	52.95	53.00	53.28	°C
Temperature at High Pressure Port	52.42	52.85	53.35	°C
Temperature at Low Pressure Port	51.04	51.57	51.69	°C
Swash Plate Angle	17	17	17	°

These operating conditions were simulated with a measured wear profile on the piston and the cylinder that were used for the measurements as shown in Figure 4.50 (measured similar to that described for the baseline).

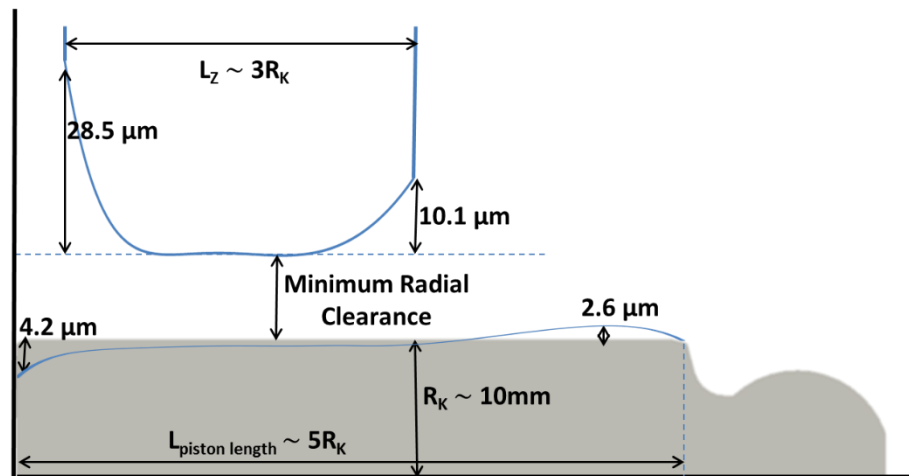


Figure 4.50. Standard surface wear profile of the tribo piston and cylinder.

The boundary conditions for the piston and the cylinder are shown in Figure 4.51. The geometry of the measured piston and cylinder, including the measured wear profiles shown above, are captured in the numerical model along with the actual measured instantaneous displacement chamber pressures over one shaft revolution, shown in Figure

4.52 - Figure 4.54 for the 3 different operating conditions, that are used in the analysis of the fluid film flow, the force balance, and the elastic deformation of the parts.

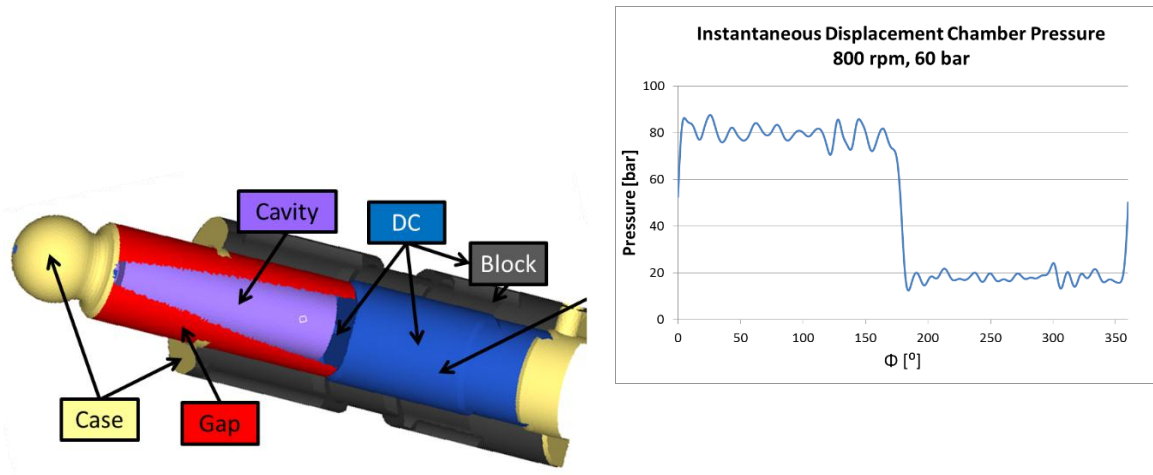


Figure 4.51. Tribo test rig piston and cylinder boundary conditions.

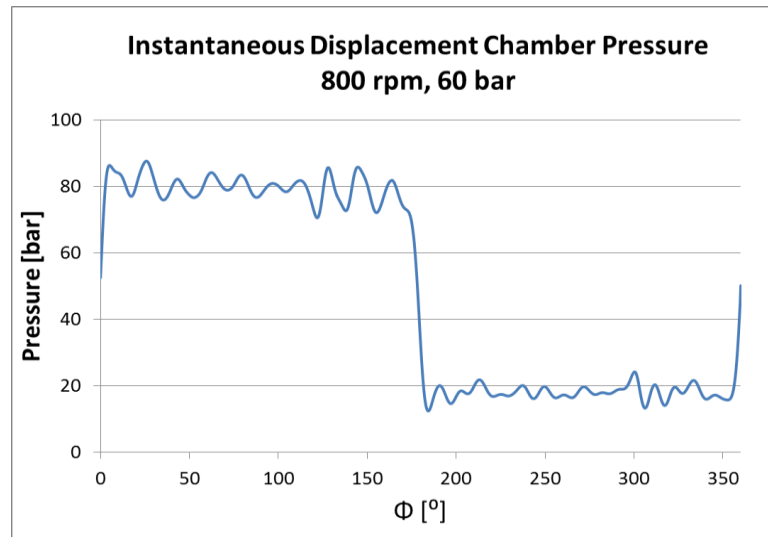


Figure 4.52. Tribo test rig measured instantaneous displacement chamber pressure for operating condition 1; 800 rpm, 60 bar.

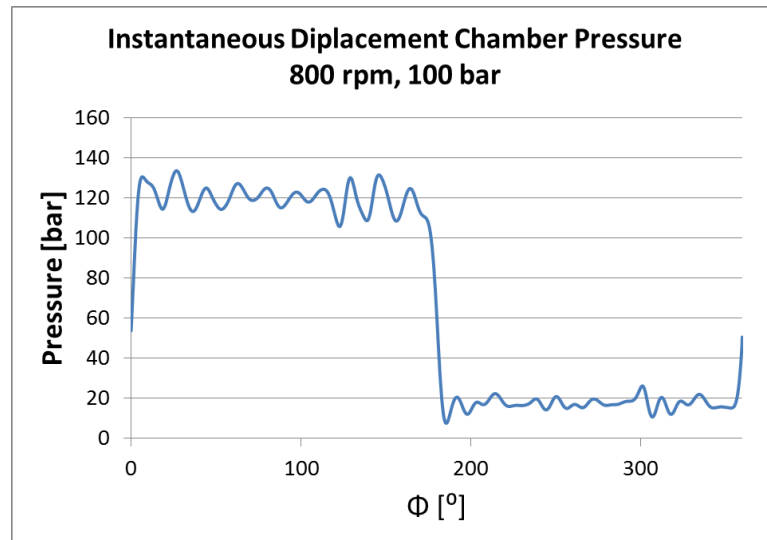


Figure 4.53. Tribo test rig measured instantaneous displacement chamber pressure for operating condition 2; 800 rpm, 100 bar.

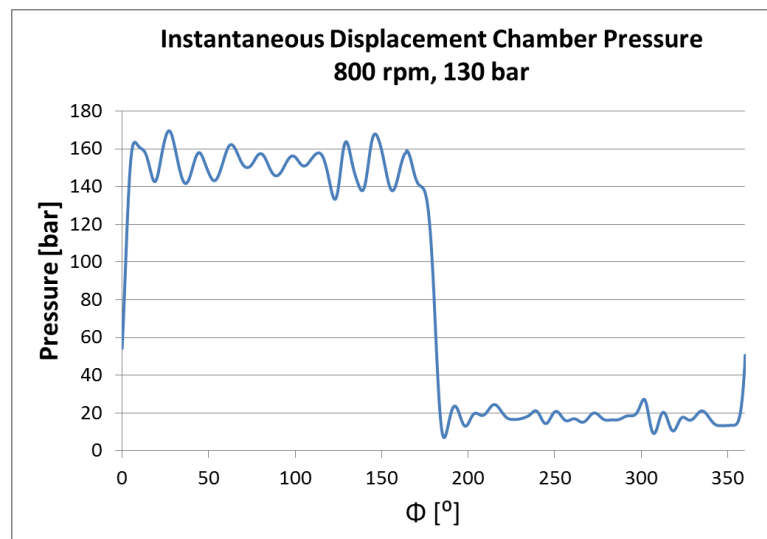


Figure 4.54. Tribo test rig measured instantaneous displacement chamber pressure for operating condition 3; 800 rpm, 130 bar.

4.4.3 Comparison of Simulation and Measurement Results

As previously stated, the tribo test rig measures the friction forces acting on the cylinder; shown below, Figure 4.55 - Figure 4.57, is the comparison of these measurements to the simulated results. The axial viscous friction forces occurring can be divided into two components, Couette and Poiseuille. The Couette is based on the relative motion of the piston while the Poiseuille is based on the pressure differential throughout

the fluid film. In the following plots, only the couette component of the viscous friction forces is compared to the measurements taken on the tribo test rig. Based on the construction of the tribo test rig, the Poiseuille component of friction is cancelled out in the measurements since there are two paths of leakage from the DC to the case; the normal path through the lubricating gap between the piston and the cylinder, and an introduced path on the opposite between the floating bushing and the DC in which the clearance is identical to that of the nominal gap between the piston and the cylinder.

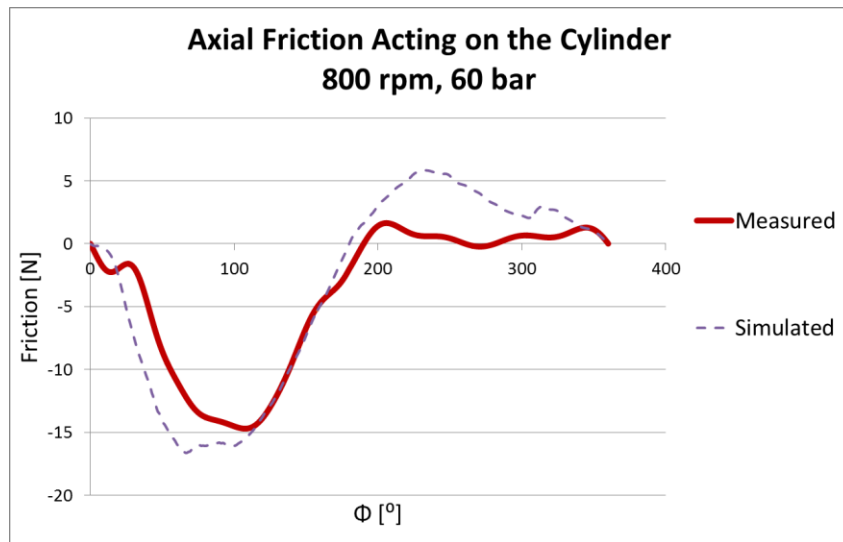


Figure 4.55. Axial friction force comparison for operating condition 1; 800 rpm, 60 bar.

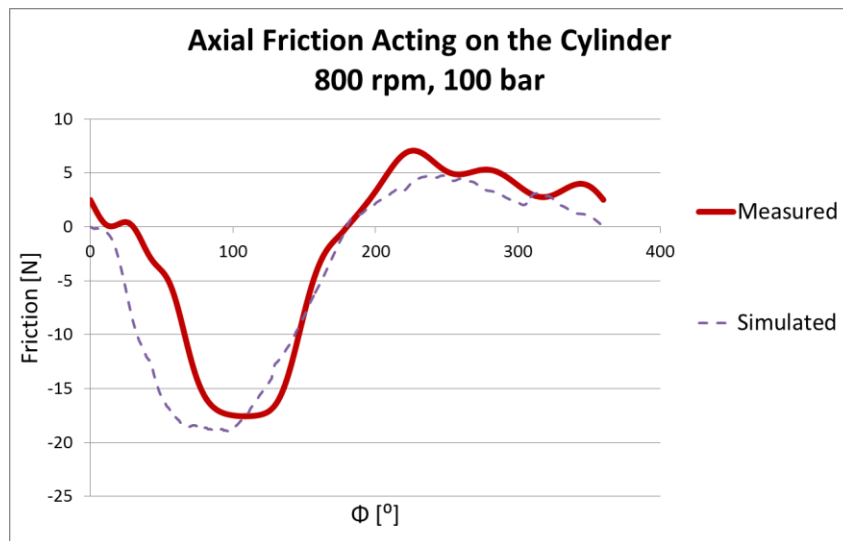


Figure 4.56. Axial friction force comparison for operating condition 2; 800 rpm, 100 bar.

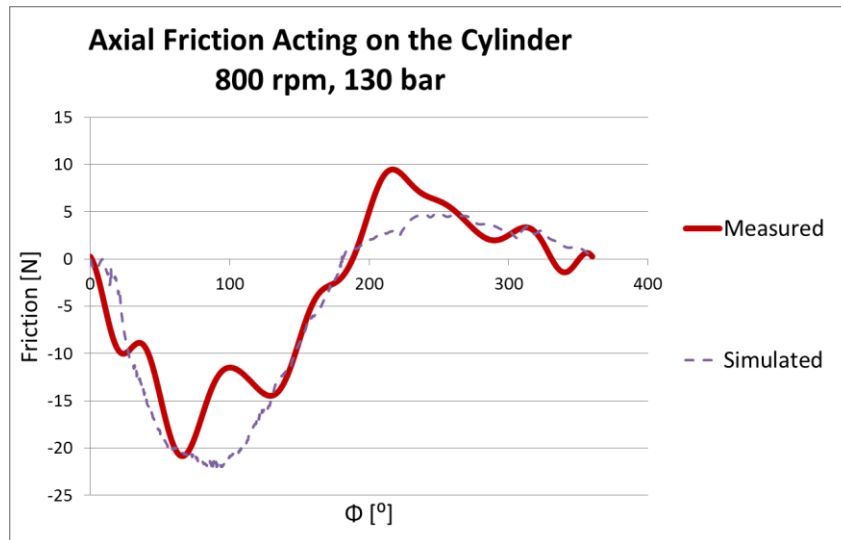


Figure 4.57. Axial friction force comparison for operating condition 3; 800 rpm, bar.

By comparing the simulated friction forces to the measured friction forces, the code can be verified as they are within reasonable difference.

CHAPTER 5. NOVEL PISTON DESIGNS

In this section, the novel piston designs that were studied in the following piston micro-surface shaping investigation are shown in detail. For the parameters of the surface profiles along with the operating conditions, the material properties, and the boundary conditions for the simulation-based investigation are described. The geometries include a sinusoidal wave, a flat sinusoidal wave, a barrel, a sinusoidal waved barrel, and a circumferential sinusoidal waved piston micro-surface shaped profile considered with a nominal, cylindrical bore without a wear profile.

5.1 Sinusoidal Wave Surface Profile (Sine Wave)

The first micro-surface shape of the piston is proposed as a sinusoidal wave following the work of Garret (2009). The sinusoidal wave is introduced in the axial direction along the gap length of the piston surface, $L_{\text{piston length}}$. This shape is represented in Figure 5.1.

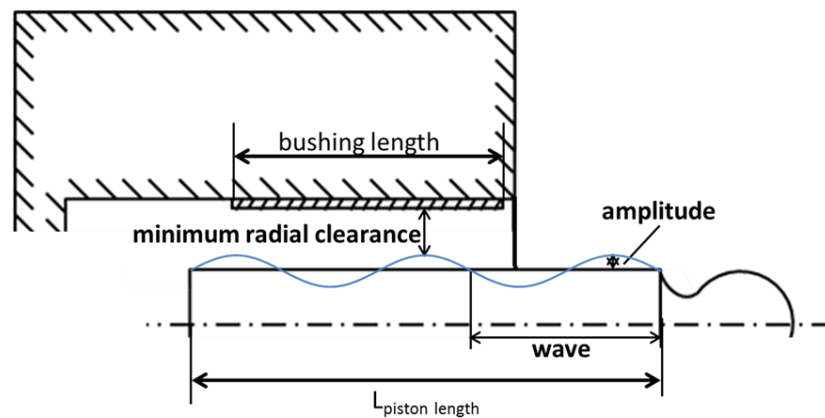


Figure 5.1. Sinusoidal wave piston surface profile.

The sinusoidal wave has two main design parameters that define its geometry and one that defines its configuration that may be varied:

1. **Amplitude:** The amplitude of the sine wave is the distance from equilibrium, the original surface of the cylindrical piston, to the peak of the oscillation of the sine wave. The peak amplitude is illustrated in Figure 5.1.
2. **Number of Waves:** The number of occurrences of a repeating event, the number of waves, in the axial direction along the gap length of the piston, $L_{\text{piston length}}$. One wave is measured between any two points with the same phase, as shown in Figure 5.1, between the corresponding zero crossings including one crest and one trough. Due to results of previous research it was found that it is best that the sine wave starts from equilibrium into a peak on both ends; half wave necessary.
3. **Minimum Radial Clearance:** The distance between the peak point of the surface profile, in this case the peak of the crest of the sine wave, and the bushing as shown in Figure 5.1. In the study to follow a 0.96 relative clearance is considered.

5.2 Flat Sinusoidal Wave Surface Profile (Flat)

From the sinusoidal wave, a flat sinusoidal waved micro-surface shape of the piston is also proposed in order to better understand the significance of the number of waves in comparison to a cylindrical piston. The flat sinusoidal wave is introduced in the axial direction along the gap length of the piston surface, $L_{\text{piston length}}$ in which the amplitude is considered at the ends and the center is flat. This shape is represented in Figure 5.2.

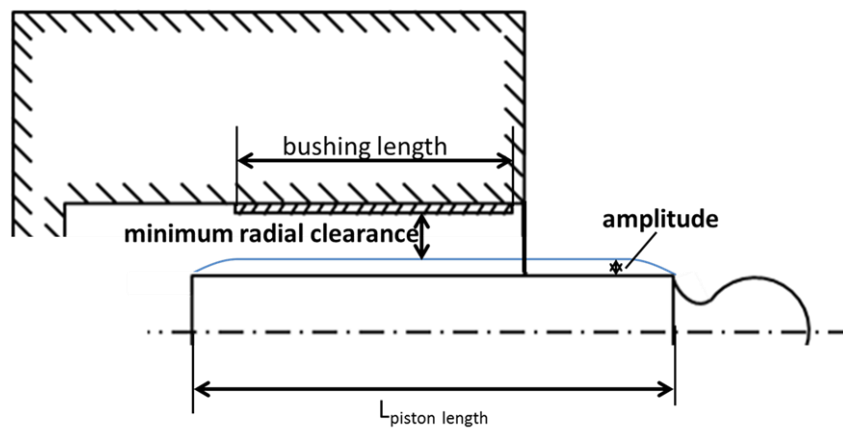


Figure 5.2. Flat sinusoidal wave piston surface profile.

The flat sinusoidal wave has one main design parameter that defines its geometry and one that defines its configuration that may be varied for optimal design:

1. Amplitude: The amplitude of the flat sine wave is the distance from equilibrium, the original surface of the cylindrical piston, to the peak of the oscillation of the sine wave, in this case the flat center surface. The peak amplitude at the ends of the gap length of the piston, $L_{\text{piston length}}$, is illustrated in Figure 5.2.
2. Minimum Radial Clearance: The distance between the peak point of the surface profile, in this case the flat surface connecting the sine wave ends, and the bushing as shown in Figure 5.2. In the study to follow a 0.96 relative clearance is considered.

5.3 Barrel Surface Profile (Barrel)

To further the state of the art work of Lasaar (2003) with the newest version of the code, another micro-surface shape of the piston to be studied is the barrel. The barrel is introduced in the axial direction along the gap length of the piston surface, $L_{\text{piston length}}$. This shape is represented in Figure 5.3.

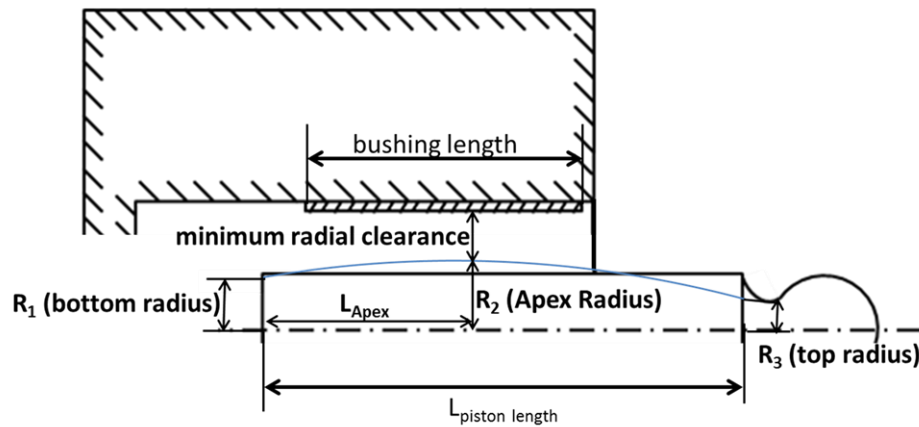


Figure 5.3. Barrel piston surface profile.

The barrel has four main design parameters that define its geometry and one that defines its configuration that may be varied for optimal design:

1. Apex Radius: The apex radius of the barrel is the distance from the center line of the piston, the z_k -axis, to the peak of the perimeter of the barrel. The apex radius is illustrated in Figure 5.3 as R_2 .
2. Apex Location: The location of the apex is considered to be the length from the DC end of the piston to the horizontal location of the peak of the barrel as shown in Figure 5.3.
3. Bottom Radius: The bottom radius of the barrel is the distance from the center line of the piston, the z_k -axis, to the perimeter of the barrel at the DC end of the piston. The bottom radius is illustrated in Figure 5.3 as R_1 .
4. Top Radius: The top radius of the barrel is the distance from the center line of the piston, the z_k -axis, to the perimeter of the barrel at the case end of the piston. The top radius is illustrated in Figure 5.3 as R_3 .
5. Minimum Radial Clearance: The distance between the peak point of the surface profile, in this case the apex of the barrel, and the bushing as shown in Figure 5.3. In the study to follow a 0.96 relative clearance is considered.

5.4 Sinusoidal Waved Barrel Surface Profile (Waved Barrel)

A combination of the sinusoidal wave and the barrel surface profile, the sinusoidal waved barrel, is another micro-surface shape of the piston to be studied. The sine wave in combination with the barrel is introduced in the axial direction along the gap length of the piston surface, $L_{\text{piston length}}$. This shape is represented in Figure 5.4.

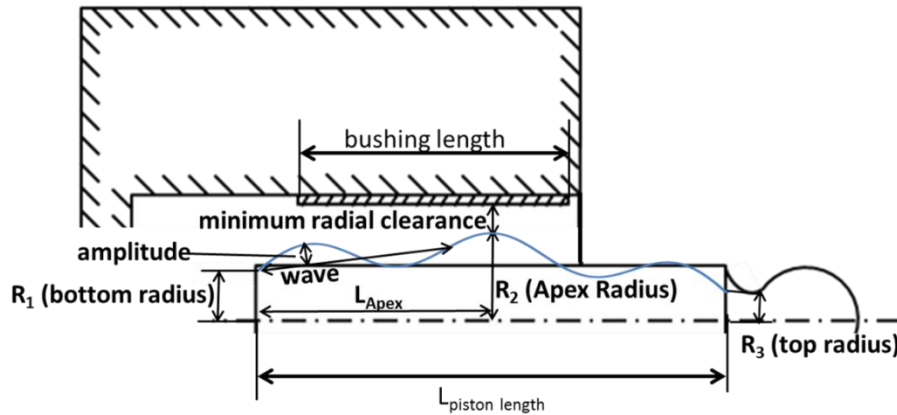


Figure 5.4. Sinusoidal wave barrel piston surface profile.

The sinusoidal wave barrel has six main design parameters, two considering the sinusoidal wave and four considering the barrel, that define its geometry and one that defines its configuration that may be varied for optimal design:

1. Amplitude: The amplitude of the sine wave is the distance from equilibrium, the original surface of the cylindrical piston, to the peak of the oscillation of the sine wave. The peak amplitude of the sine barrel is illustrated in Figure 5.4.
2. Number of Waves: The number of occurrences of a repeating event, the number of waves, in the axial direction along the barrel along the gap length of the piston,. One wave is measured between any two points with the same phase, as shown in Figure 5.4, between the corresponding “zero crossings”, or in this case the center between the crest and trough, including one crest and one trough.
3. Apex Radius: The apex radius of the sine barrel is the distance from the center line of the piston, the z_k -axis, to the peak of the perimeter of the barrel in combination with the crest of the sine wave. The apex radius is illustrated in Figure 5.4 as R_2 .
4. Apex Location: The location of the apex is considered to be the length from the DC end of the piston to the horizontal location of the peak of the sine barrel as shown in Figure 5.4.
5. Bottom Radius: The bottom radius of the wave barrel is the distance from the center line of the piston, the z_k -axis, to the perimeter of the wave barrel at the DC end of the piston. The bottom radius is illustrated in Figure 5.4 as R_1 .

6. Top Radius: The top radius of the wave barrel is the distance from the center line of the piston, the z_k -axis, to the perimeter of the wave barrel at the case end of the piston. The top radius is illustrated in Figure 5.4 as R_3 .
7. Minimum Radial Clearance: The distance between the peak point of the surface profile, in this case the apex of the wave barrel, and the bushing as shown in Figure 5.4. In the study to follow a 0.96 relative clearance is considered.

5.5 Circumferential Sinusoidal Wave Surface Profile

A combination of a circumferential sinusoidal wave and the flat surface profile of the cylindrical piston are two more micro-surface shapes of the piston to be studied. The sine wave is introduced in the circumferential direction in combination with either the flat surface profile in the axial direction along the gap length of the piston surface or in combination with the standard cylindrical piston. These shapes are further described below.

5.5.1 In Combination with Flat Sinusoidal Wave Surface Profile

The combination of the circumferential sinusoidal wave with the flat surface profile is represented in Figure 5.5.

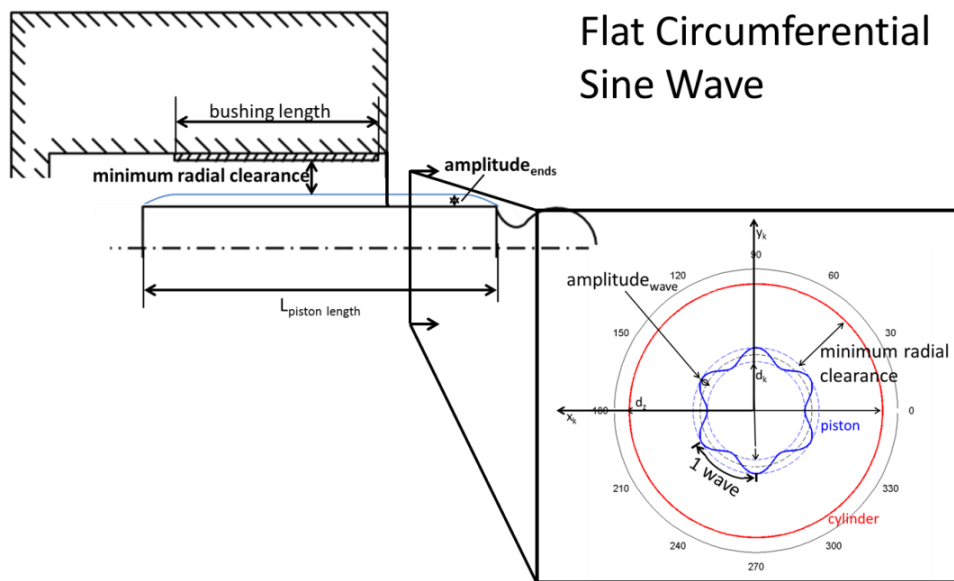


Figure 5.5. Circumferential sinusoidal wave in combination with the flat sinusoidal wave piston surface profile.

The circumferential sinusoidal wave in combination with the flat sinusoidal wave has three main design parameters that define its geometry, a combination of the sine wave parameters and the flat sine parameters, and one that defines its configuration that may be varied for optimal design:

1. Amplitude Ends: The amplitude of the flat sine wave is the distance from equilibrium, the original surface of the cylindrical piston, to the peak of the oscillation of the sine wave, in this case the flat center surface. The peak amplitude at the ends of the gap length of the piston, $L_{\text{piston length}}$, is illustrated in Figure 5.5, the same as Figure 5.2 in Section 5.2.
2. Amplitude Wave: The amplitude of the circumferential sine wave is the distance from equilibrium, the original surface of the cylindrical piston, to the peak of the oscillation of the sine wave. The peak amplitude is illustrated in the bottom right $x_k - y_k$ cross-section of Figure 5.5.
3. Number of Waves: The number of occurrences of a repeating event, the number of waves, in the circumferential direction around the circumference of the surface of the piston. One wave is measured between any two points with the same phase, as shown in the bottom right $x_k - y_k$ cross-section of Figure 5.5, between corresponding crest to crest.
4. Minimum Radial Clearance: The distance between the peak point of the surface profile, in this case the peak of the crest of the sine wave along the flat surface, and the bushing as shown in Figure 5.5. In the study to follow a 0.96 relative clearance is considered.

5.5.2 In Combination with Cylindrical Surface Profile

The combination of the circumferential sinusoidal wave with the cylindrical piston is represented in Figure 5.6.

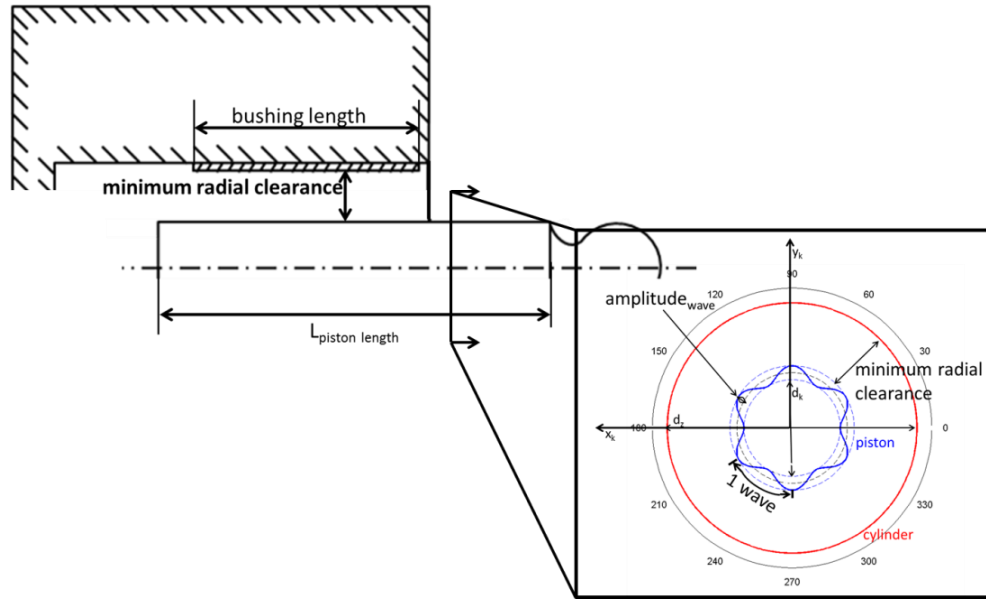


Figure 5.6. Circumferential sinusoidal wave in combination with the cylindrical piston surface profile.

The circumferential sinusoidal wave in combination with cylindrical piston has two main design parameters that define the geometry of the sine wave and one that defines its configuration that may be varied for optimal design:

1. Amplitude Wave: The amplitude of the circumferential sine wave is the distance from equilibrium, the original surface of the cylindrical piston, to the peak of the oscillation of the sine wave. The peak amplitude is illustrated in the bottom right $x_k - y_k$ cross-section of Figure 5.6.
2. Number of Waves: The number of occurrences of a repeating event, the number of waves, in the circumferential direction around the circumference of the surface of the piston. One wave is measured between any two points with the same phase, as shown in the bottom right $x_k - y_k$ cross-section of Figure 5.6, between corresponding crest to crest.
3. Minimum Radial Clearance: The distance between the peak point of the surface profile, in this case the peak of the crest of the sine wave, and the bushing as shown in Figure 5.6. In the study to follow a 0.96 relative clearance is considered.

CHAPTER 6. PISTON MICRO-SURFACE SHAPING DESIGN PARAMETER STUDY

In this section the main, base design surface profiles (the sine wave, the flat, and the barrel) are studied in further detail in order to find the optimal design parameter of the various surface shapes. The overall decrease in power loss and the leakage will be evaluated along with the performance in order to better understand the effects that the design parameters have on the results of the piston/cylinder interface. In respect to the computational cost and time only 4 operating conditions were studied as shown in Table 6.1.

Table 6.1. Design parameter study operating conditions.

Operating Condition – Pumping ($\beta = 100\%$)	1	2	3	4	Unit
High Pressure	125	325	125	325	bar
Low Pressure	25	25	25	25	bar
Angular Speed	1000	1000	2000	2000	rpm
Swash Plate Angle	17	17	17	17	°

6.1 Sinusoidal Wave Piston Surface Profile Design Parameters Study

The sine wave piston surface profile, shown in Figure 5.1, was investigated by varying the amplitude of the wave and also the number of waves in order to better understand the effect that each design parameter had on the performance of the piston cylinder interface. The amplitude was varied from 1 μm to 11 μm in increments of 2 μm , example of this shown in Figure 6.1, while the number of waves was simultaneously varied from 1.5-10.5 waves in 1 wave increments, example of this shown in Figure 6.2.

A previous study was done showing that the sine wave performed best when both ends were on a downward slope of the sine wave; the reason for the half wave in this

study. The complete combination of these design parameters that were studied can be seen in Table 6.2. Throughout this study the relative clearance was kept constant at 0.96.

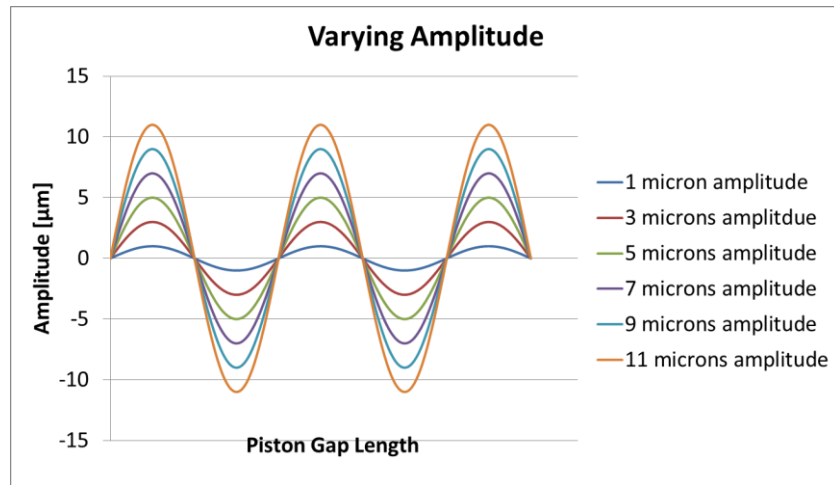


Figure 6.1. Varying amplitude of the sine wave piston surface profile.

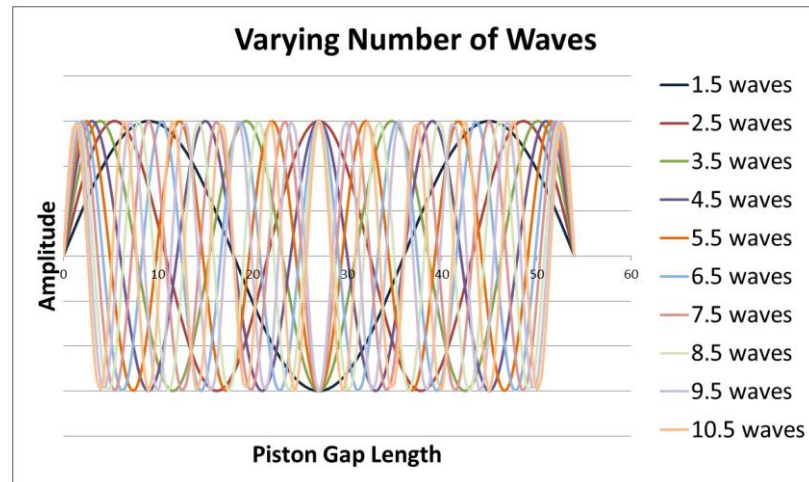


Figure 6.2. Varying number of waves of the sine wave piston surface profile.

Table 6.2. Complete combination list of design parameters for sine wave design parameter study.

Amplitude (μm)	Number of Waves
1	1.5, 2.5, 3.5, 4.5, 5.5, 6.5, 7.5, 8.5, 9.5, 10.5
3	1.5, 2.5, 3.5, 4.5, 5.5, 6.5, 7.5, 8.5, 9.5, 10.5
5	1.5, 2.5, 3.5, 4.5, 5.5, 6.5, 7.5, 8.5, 9.5, 10.5
7	1.5, 2.5, 3.5, 4.5, 5.5, 6.5, 7.5, 8.5, 9.5, 10.5
9	1.5, 2.5, 3.5, 4.5, 5.5, 6.5, 7.5, 8.5, 9.5, 10.5
11	1.5, 2.5, 3.5, 4.5, 5.5, 6.5, 7.5, 8.5, 9.5, 10.5

The decrease in energy dissipation from the baseline, Figure 6.3 to Figure 6.6, is considered for the various amplitude and number of waves on the sine wave piston surface profile. This simulation study was conducted for the various operating conditions at full displacement (operating conditions 1-4, respectively shown).

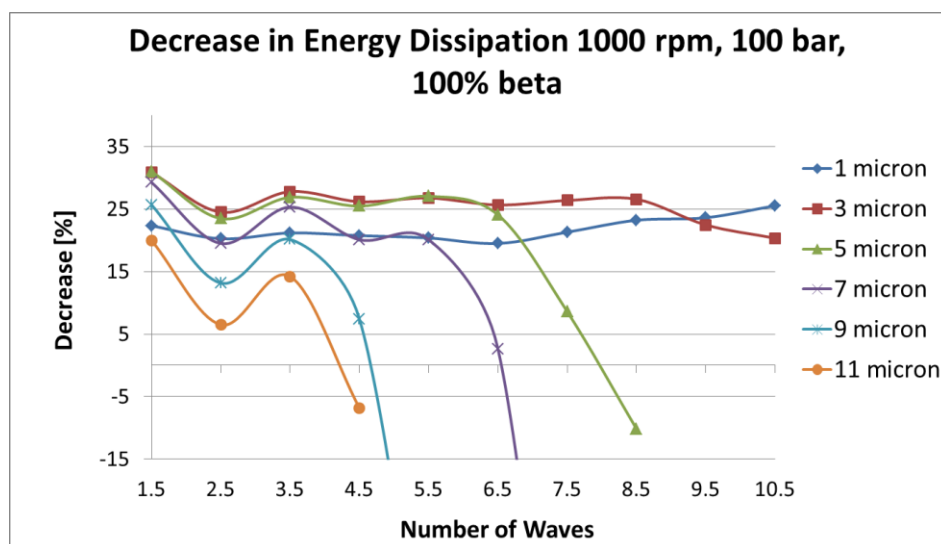


Figure 6.3. Decrease in energy dissipation due to varying the design parameters of the sine wave piston surface profile – operating condition 1 - 1000 rpm, 100 bar, 100%.

For operating condition 1, a 3 μ m amplitude in combination with any number of waves studied are the best for the sine wave surface profile in terms of decreasing energy dissipation from the baseline. The number of waves seem to have little effect on the 1 μ m amplitude also whereas the larger the amplitude, the larger the effect of the number of waves; the more waves, the worse the total energy dissipation. In general, as the amplitude increases so does the energy dissipation with the exception of the 1 μ m amplitude.

For operating condition 2, a 3 μ m amplitude in combination with any number of waves studied are the best for the sine wave surface profile in terms of decreasing energy dissipation from the baseline. At this operating condition, 1 μ m amplitude did not even converge numerically as too much contact between the piston and the bushing was occurring. The 1.5 wave sinusoidal surface profiles also did not converge for the various

amplitudes. As shown previous, the number of waves and the amplitude of the sine wave continue to have the same effect on the energy dissipation with the increased operating pressure.

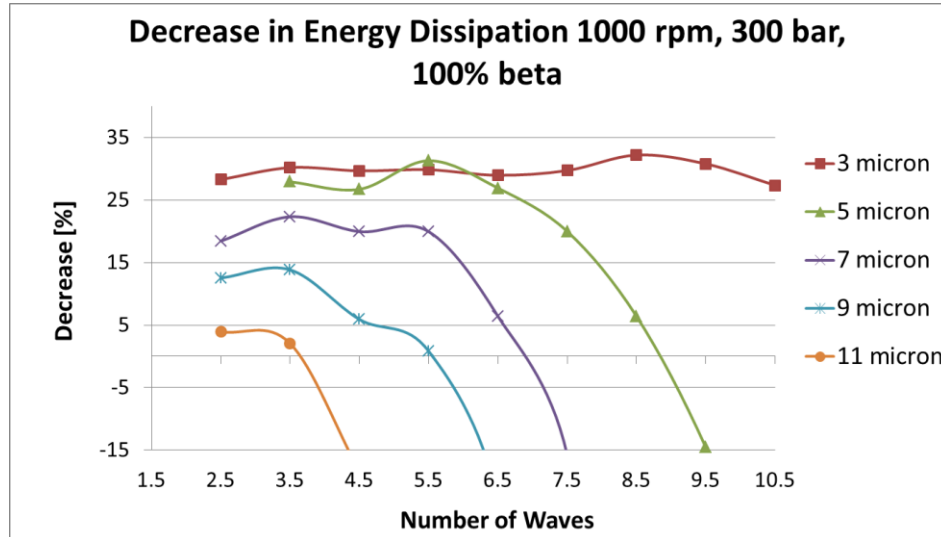


Figure 6.4. Decrease in energy dissipation due to the design parameters of the sine wave piston surface profile – operating condition 2 - 1000 rpm, 300 bar, 100%..

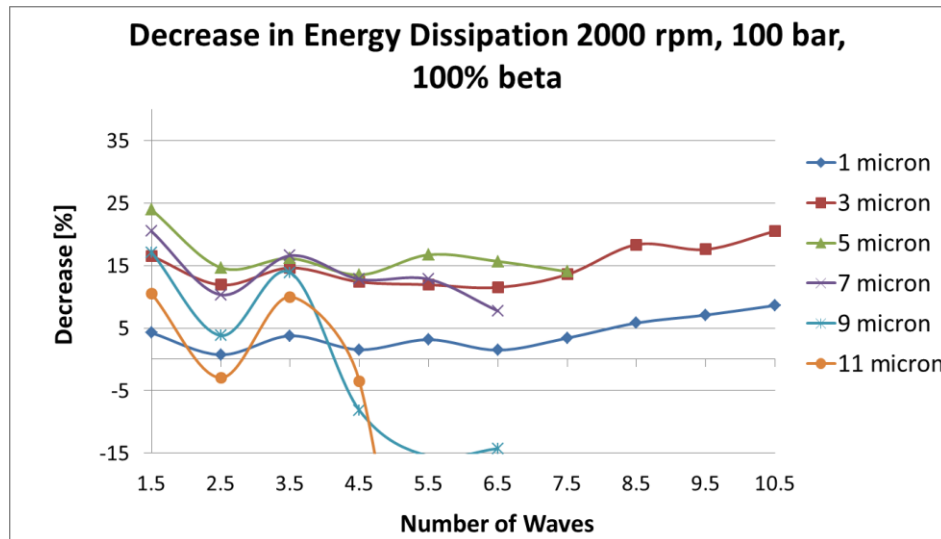


Figure 6.5. Decrease in energy dissipation due to varying the design parameters of the sine wave piston surface profile – operating condition 3 - 2000 rpm, 100 bar, 100%.

For operating condition 3, a 3 μm amplitude in combination with any number of waves studied are again the best for the sine wave surface profile in terms of decreasing energy dissipation from the baseline. At this operating condition the larger amplitude sine waves fail to numerically converge with more waves due to the increased detrimental contact occurring. The number of waves maintains to have little effect on the smaller amplitudes (1 μm - 3 μm). The same trend follows for the slower speed operating condition 1.

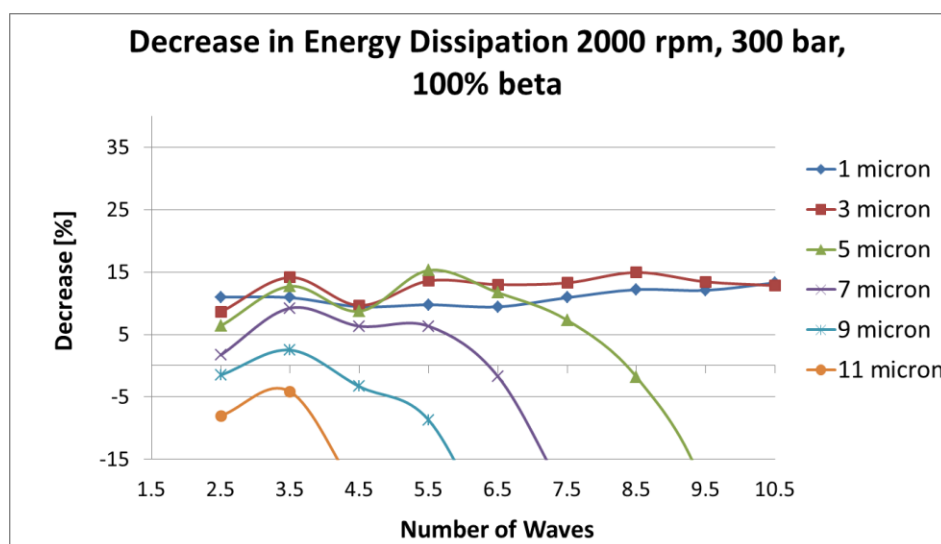


Figure 6.6. Decrease in energy dissipation due to varying the design parameters of the sine wave piston surface profile – operating condition 4 - 2000 rpm, 300 bar, 100%.

For operating condition 4, a 1 μm - 3 μm amplitude with any number of waves studied are the best for the sine wave surface profile in terms of decreasing energy dissipation. The same trend follows as previously shown for the other operating conditions.

Overall the best design parameters for the sine wave are an amplitudes of 3 μm in combination with 2.5-10.5 waves in an increment of 1 (1.5 waves is left out since the model did not converge for this number of waves at an operating pressure of 300 bar) over the operating conditions studied. It also follows that the number of waves has little effect on the energy dissipation at smaller amplitudes while increasing the number of waves in conjunction with larger amplitudes increases the energy dissipation more. In

general, as the amplitude increases so does the energy dissipation with the exception of the 1 μm amplitude. The decrease in leakage from the baseline, Figure 6.7-Figure 6.10, is considered for the amplitudes and number of waves for the sine wave piston surface profile for operating conditions 1-4.

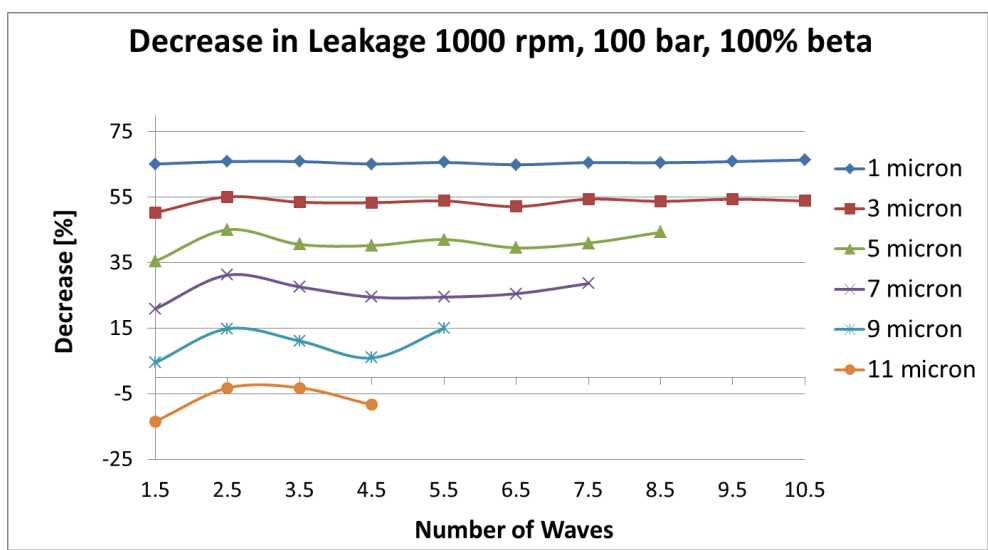


Figure 6.7. Decrease in leakage due to varying the design parameters of the sinusoidal wave piston surface profile – operating condition 1 - 1000 rpm, 100 bar, 100%.

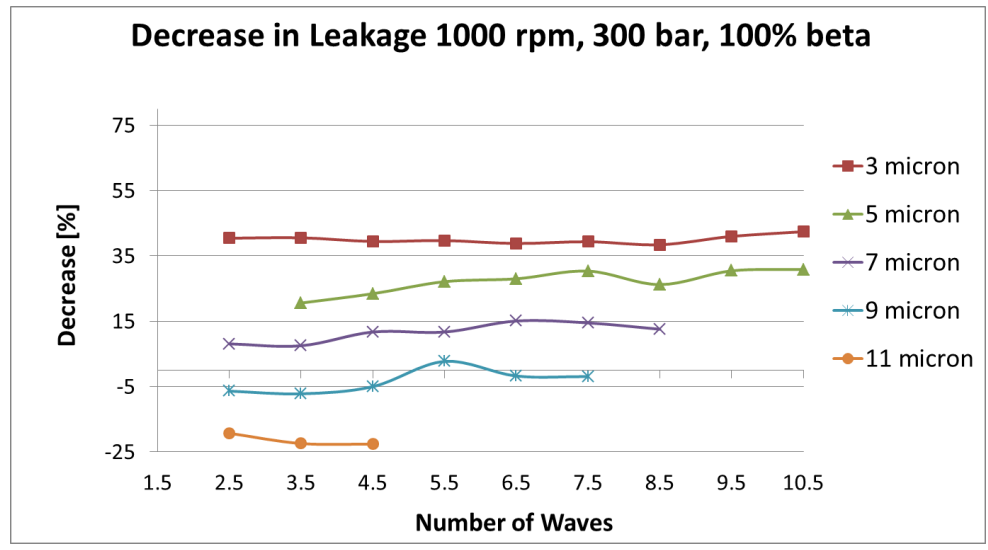


Figure 6.8. Decrease in leakage due to the design parameters of the sinusoidal wave piston surface profile – operating condition 2 - 1000 rpm, 300 bar, 100%.

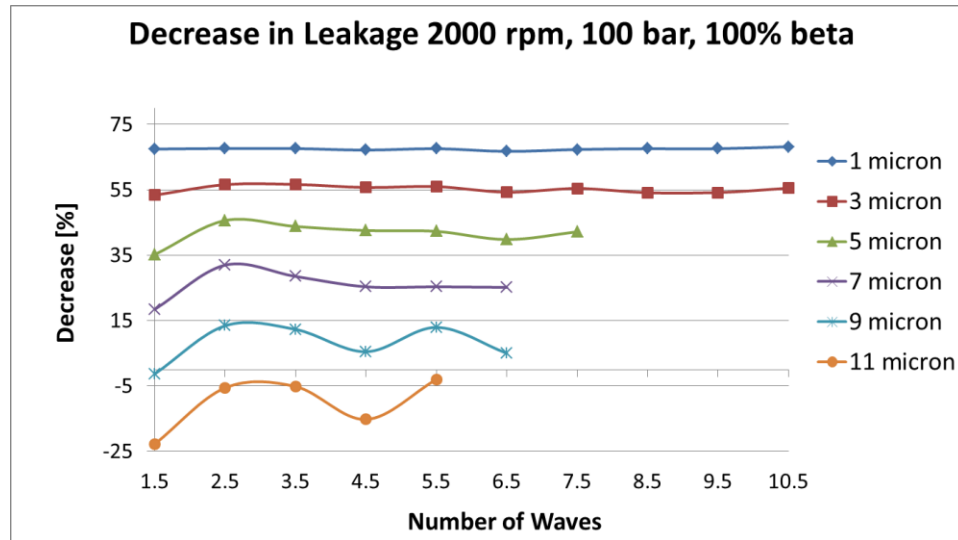


Figure 6.9. Decrease in leakage due to varying the design parameters of the sinusoidal wave piston surface profile – operating condition 3 - 2000 rpm, 100 bar, 100%.

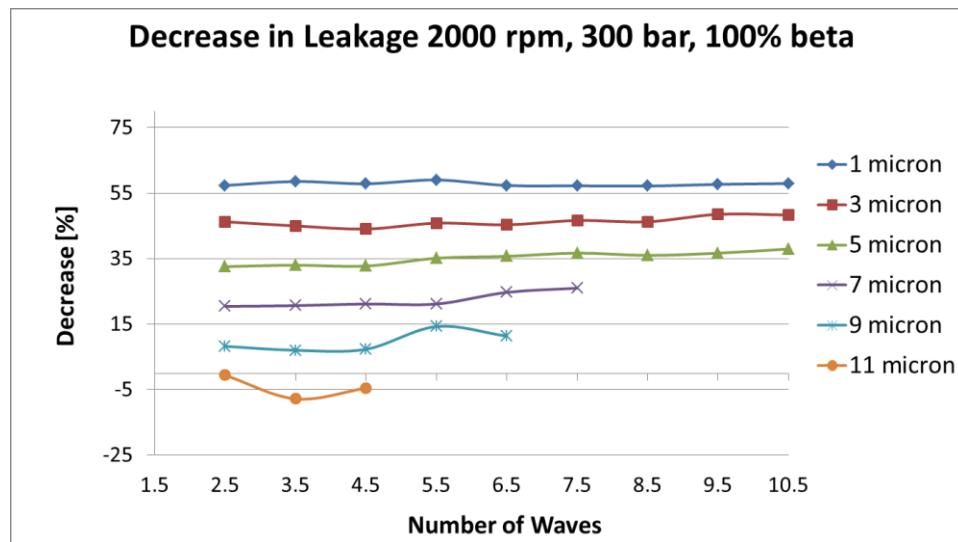


Figure 6.10. Decrease in leakage due to varying the design parameters of the sinusoidal wave piston surface profile – operating condition 4 - 2000 rpm, 300 bar, 100%.

Among all of the operating conditions shown above, the decrease in leakage is largest the smaller the amplitude. It also follows that the larger the amplitude, the larger the effect that the number of waves has on the results.

Comparing the leakages losses to the total energy dissipation, it can be noted that the 1 μm amplitude results in larger torque losses as the larger decreases in leakages are not directly reflected in the total energy dissipation. The torque losses are also increased for the larger number of waves with the larger amplitudes as shown in the energy dissipation while they remain more constant among the lower amplitudes.

6.1.1 Vary Amplitude

In order to show the impact that varying the amplitude of the sine wave surface profile, a constant number of waves was chosen. For the case shown below, 6.5 waves was chosen at operating condition 4. With this number of waves, the effect that the amplitude has on the performance of the interface is apparent since at this number of waves there is a large difference in the energy dissipation as shown previously for the different amplitudes.

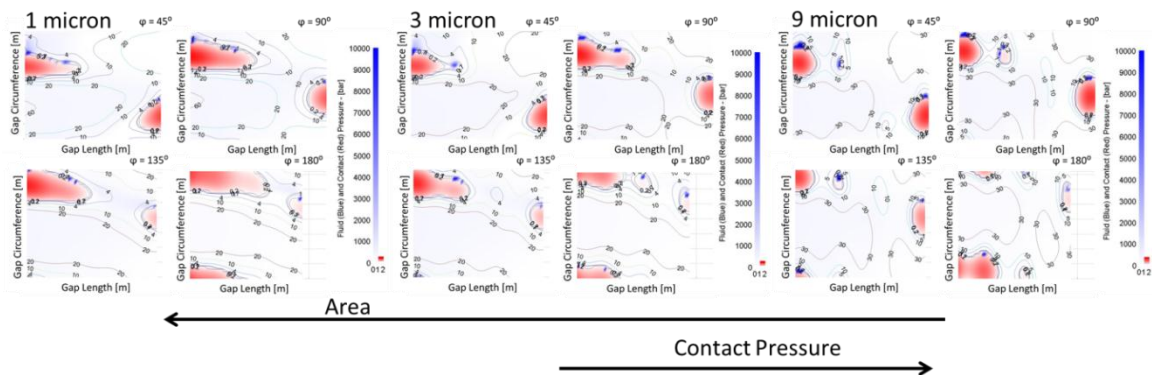


Figure 6.11. Varying amplitude of the sine wave piston surface profile multi-plots – operating condition 4; 2000 rpm, 300 bar, 100%.

As the amplitude increases on the sine wave surface profile at this operating condition, it can be seen that the area of critical minimum fluid film thicknesses decreases. The contact pressure between the 1 μm and the 3 μm are similar and this is why the 3 μm amplitude results in a larger decrease due to the larger decrease in torque losses, less area of critical minimum film thickness. Although the 9 μm amplitude sine wave results in less area, the contact pressure is slightly higher; this in combination with

the increase in leakage results in the larger increase in energy dissipation with the constant 6.5 waves.

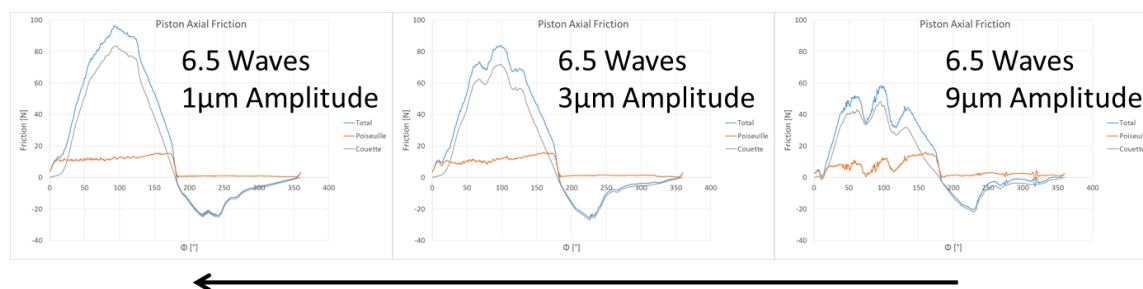


Figure 6.12. Varying amplitude of the sine wave piston surface profile piston axial friction forces – operating condition 4; 2000 rpm, 300 bar, 100%.

The increase in the amplitude of the waves on the sine wave surface profile decreases the axial friction forces acting on the cylinder. The reason for this is depicted in the multiplots shown above. The areas of the critical fluid film thickness are larger at the lower amplitudes although the contact pressures increase with the higher amplitude, this is not considered in the code, therefore the friction forces are calculated to be larger according to the larger areas of critical minimum fluid film.

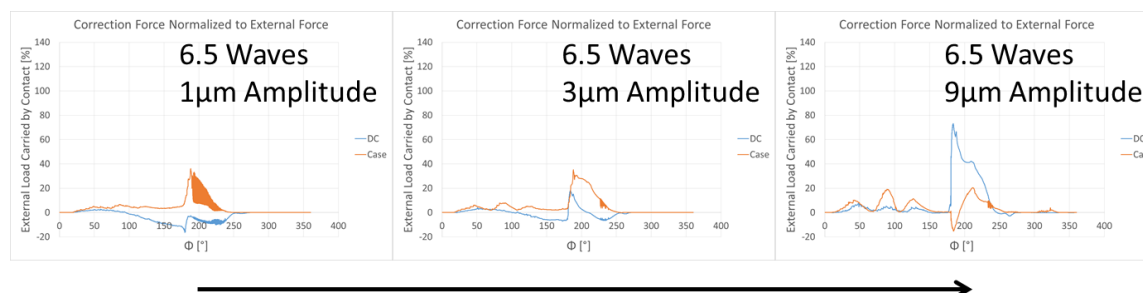


Figure 6.13. Varying amplitude of the sine wave piston surface profile correction forces normalized to external force – operating condition 4; 2000 rpm, 300 bar, 100%.

The correction force normalized to the external forces shown above conclude that as the amplitude of the sine wave increases to 9 μm , the load carried by the contact also increases on the DC side meaning that more critical fluid film thickness is occurring which leads to an increase in torque indicating the increase in the energy dissipation. As

for the lower amplitude sine waves, the correction is very similar although the $1\ \mu\text{m}$ amplitude wave tends to be a little less stable and bounces as the transition is made to the low pressure stroke around 180° .

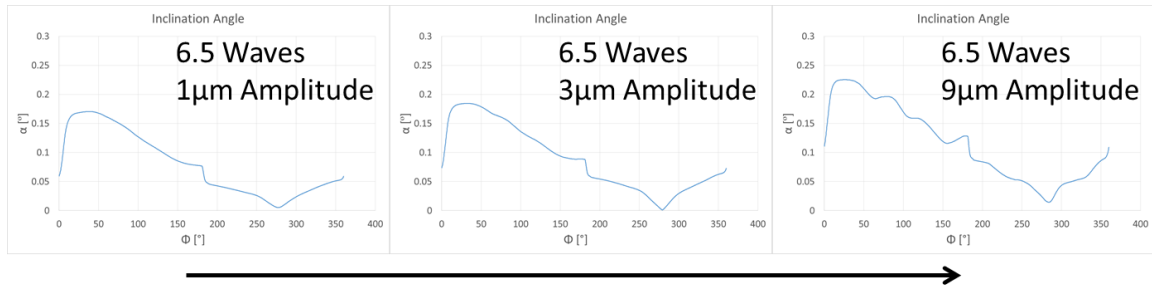


Figure 6.14. Varying amplitude of the sine wave piston surface profile inclination angles—operating condition 4; 2000 rpm, 300 bar, 100%.

As expected, the inclination angle increases as the amplitude of the sine wave increases; as the amplitude increases, the piston is able to tilt more within the bore based on the increased slopes at the ends. It can be seen that with the $2\ \mu\text{m}$ increase between the inclination angle only slightly increases. With the $6\ \mu\text{m}$ increase in amplitude, the inclination angle increases much more. The angle does not increase as much as it possibly could though and this is the reason that the leakage is better at the lower end amplitude in which a better seal between the piston and the cylinder is created reducing the leakage in the gap.

6.1.2 Vary Number of Waves

In order to show the impact that varying the number of waves on the sine wave surface profile, a constant amplitude was chosen. For the case shown below, an amplitude of $5\ \mu\text{m}$ was chosen at operating condition 4. At this amplitude, the effect that the number of waves has on the performance of the interface should be apparent since at this amplitude there is a change in energy dissipation at this operating condition as previously shown.

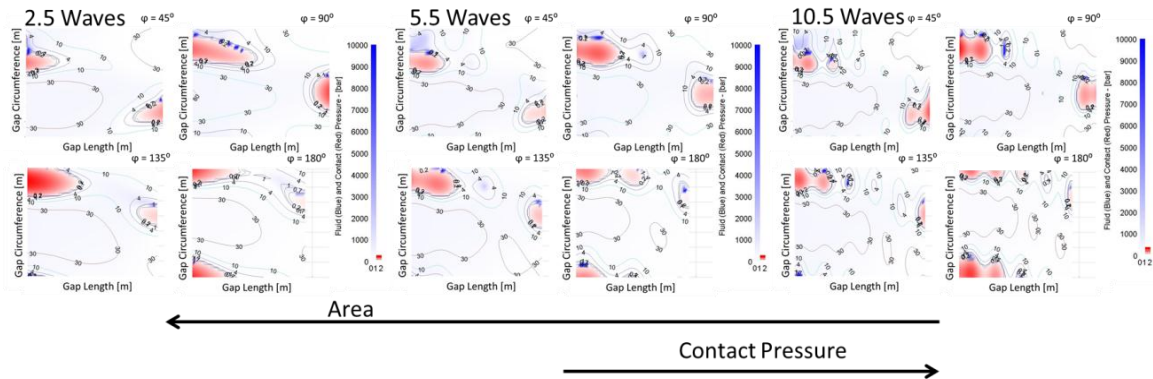


Figure 6.15. Varying the number of waves of the sine wave piston surface profile multi-plots – operating condition 4; 2000 rpm, 300 bar, 100%.

As the number of waves increases on the sine wave surface profile at this operating condition, it can be seen that the area of critical minimum fluid film thicknesses decreases, but the contact pressure of those areas increases. This can be seen more so for the 10.5 waves; with more waves, there is less area to contact, but the critical minimum fluid film thickness becomes more detrimental. This is why as the large increase in energy dissipation is seen at the 10.5 waves as the torque losses increase with the increase in the contact pressure.

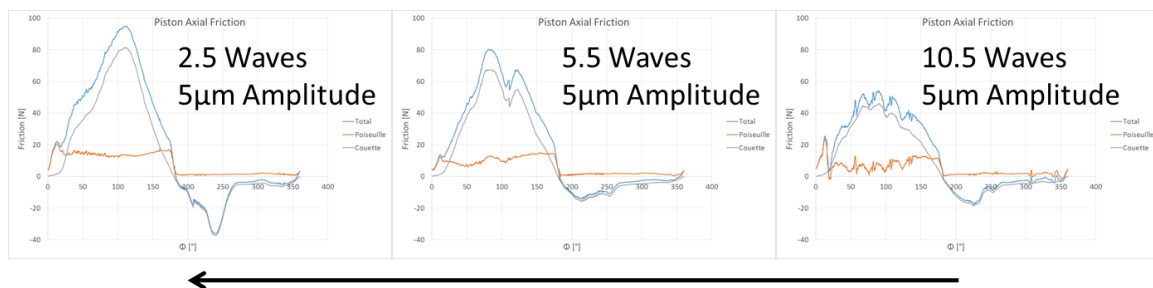


Figure 6.16. Varying the number of waves of the sine wave piston surface profile piston axial friction forces – operating condition 4; 2000 rpm, 300 bar, 100%.

The increase in the number of waves on the sine wave surface profile decreases the axial friction forces acting on the cylinder. The reason for this is depicted in the multi-plots shown above as previously described.

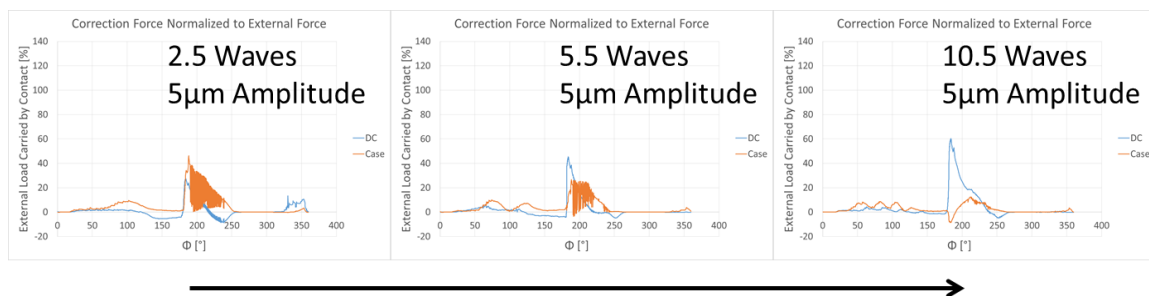


Figure 6.17. Varying the number of waves of the sine wave piston surface profile correction forces normalized to external force – operating condition 4; 2000 rpm, 300 bar, 100%.

When it comes to the correction force normalized to the external forces, it can be seen that as the number of sine waves increases to 10.5 waves, the load carried by the contact also increases on the DC side meaning that more critical fluid film thickness is occurring which leads to an increase in torque mirroring the increase in the energy dissipation that is shown for the 10.5 waves.

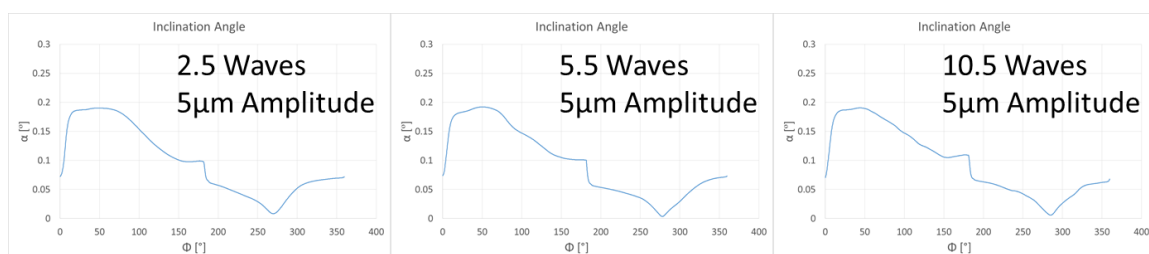


Figure 6.18. Varying the number of waves of the sine wave piston surface profile inclination angles – operating condition 4; 2000 rpm, 300 bar, 100%.

The inclination of the piston does not change much considering the amplitude of the sine wave remains the same in which the number of waves does not have a large effect on this. As this is the case shown, it also correlates to the similar leakage shown in Figure 6.10 in which the number of waves is not shown to have an effect.

6.2 Flat Sinusoidal Wave Piston Surface Profile Design Parameters Study

The flat piston surface profile, shown in Figure 5.2, was investigated by varying the amplitude at the ends of the piston gap length. The amplitude was varied from $1\mu\text{m}$ to $11\mu\text{m}$ in increments of $2\mu\text{m}$ as shown in Figure 6.19. Throughout this study the relative clearance was kept constant at 0.96.

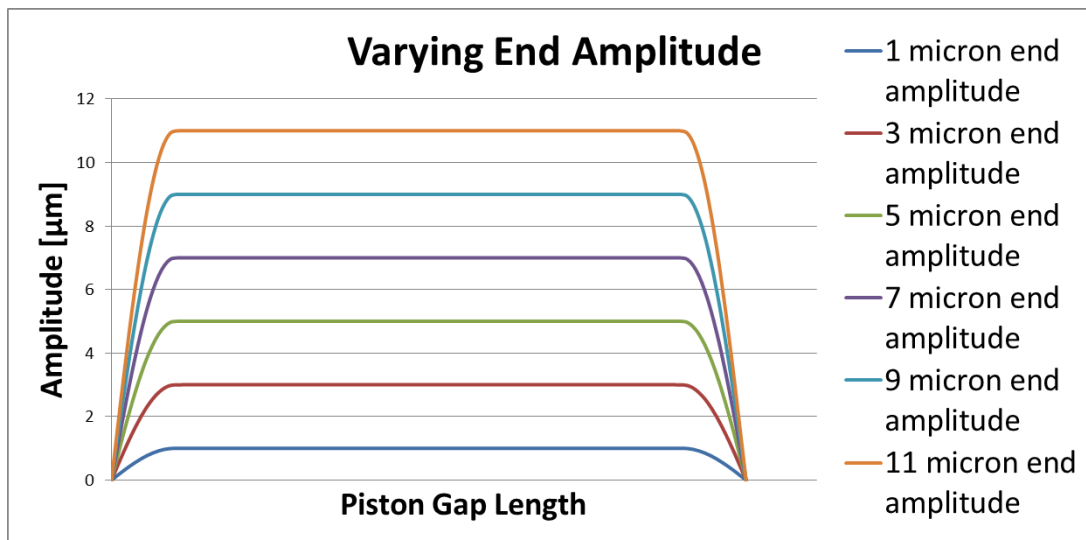


Figure 6.19. Varying end amplitude of the flat sinusoidal wave piston surface profile.

The decrease in energy dissipation from the baseline, Figure 6.20, is considered for the various amplitude on the flat piston surface profile. This simulation study was conducted for the various operating conditions at full displacement (operating conditions 1-4).

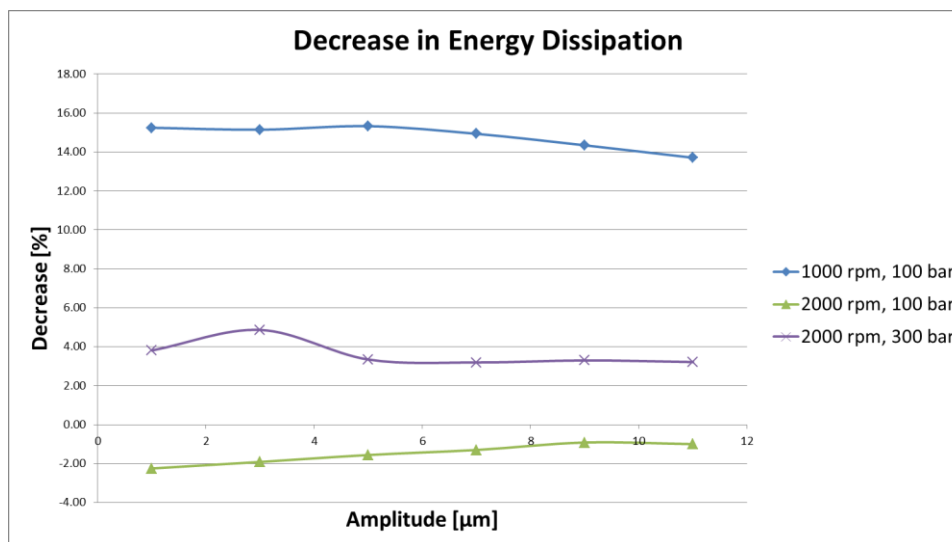


Figure 6.20. Decrease in energy dissipation due to varying the design parameters of the flat piston surface profile; (operating condition 1-4).

The decrease in energy dissipation is shown to not strongly depend on the amplitude of the ends of the flat piston surface profile. Since the clearance between the piston and the

cylinder remains the same along the flat gap length of the piston, the change in the ends has little effect.

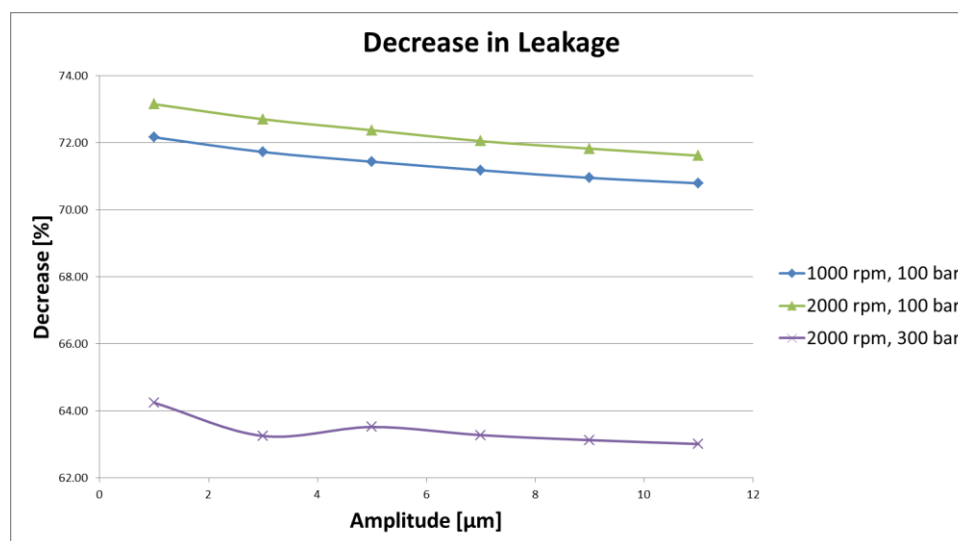


Figure 6.21. Decrease in leakage due to varying the design parameters of the flat piston surface profile – (operating condition 1-4).

The same trend follows for the leakage as was the case for the energy dissipation. Although, the leakage slightly increases with the increase in the amplitude of the ends; a larger amplitude results in a larger area for the fluid to flow from the gap.

6.2.1 Vary Amplitude at Ends

Below details the impact that varying the amplitudes of the ends of the flat piston surface profile has on the performance of the interface. For the case shown the amplitude is varied between 1 μm , 5 μm , and 9 μm . The results are shown for one operating conditions, operating condition 4.

As can be seen in the multi-plots above, the areas of the critical minimum fluid film along with the contact pressure remain similar while varying the amplitude. This reflects the little change in the energy dissipation along with the leakages since the motion of the piston within the bore does not seem to be influenced by the amplitude at the ends of the flat surface profile.

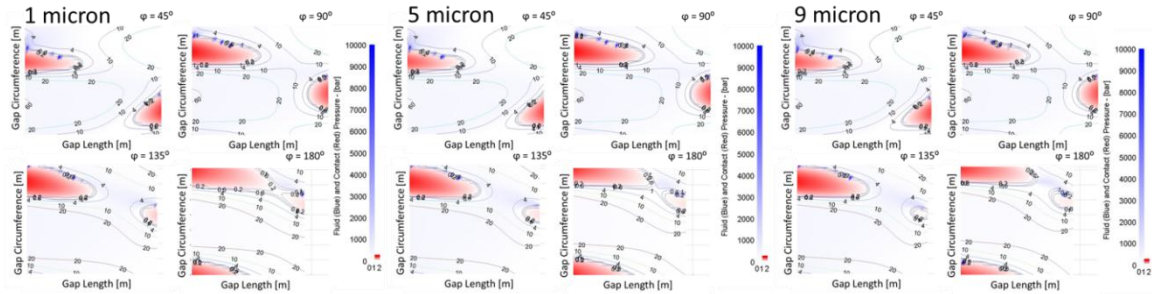


Figure 6.22. Varying the amplitude at the ends of the flat piston surface profile multi-plots – operating condition 4; 2000 rpm, 300 bar, 100%.

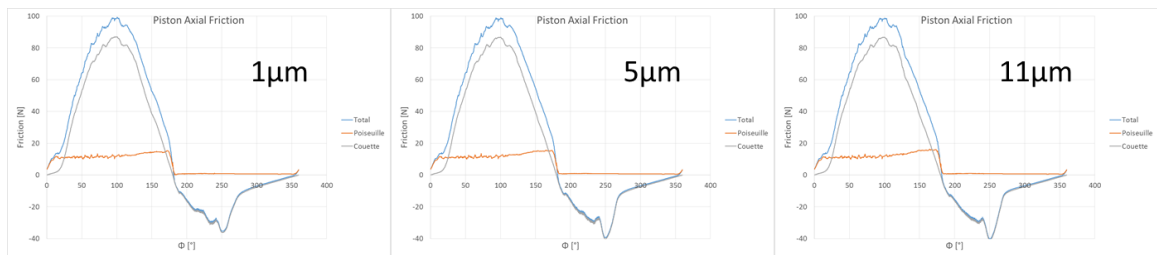


Figure 6.23. Varying the amplitude at the ends of the flat piston surface profile piston axial friction forces – operating condition 4; 2000 rpm, 300 bar, 100%.

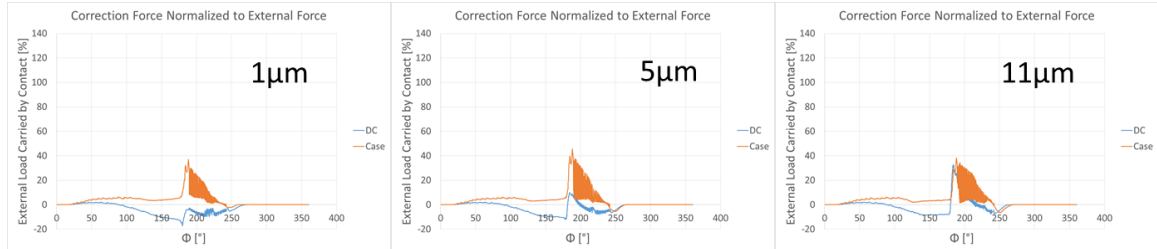


Figure 6.24. Varying the amplitude at the ends of the flat piston surface profile correction forces normalized to external force – operating condition 4; 2000 rpm, 300 bar, 100%.

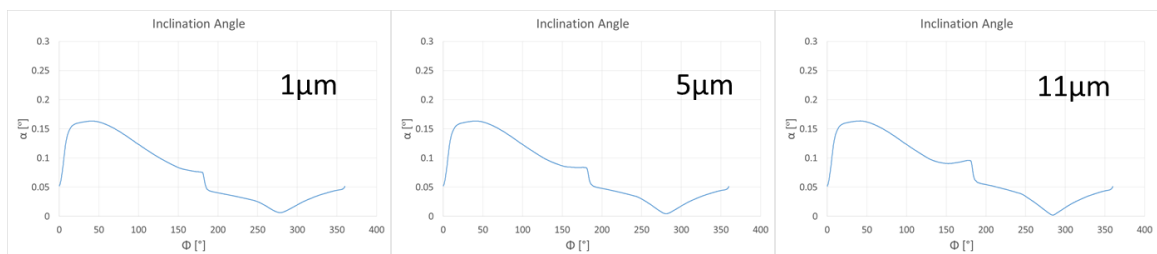


Figure 6.25. Varying the amplitude at the ends of the flat piston surface profile inclination angles – operating condition 4; 2000 rpm, 300 bar, 100%.

As shown in the multi--plots, the motion of the piston as the amplitudes of the ends of the flat surface profile change remains the same. Therefore, as this is the case, the axial friction forces acting on the cylinder, the correction of the piston within the bore, and the inclination angle of the piston remains the same.

6.3 Barrel Piston Surface Profile Design Parameters Study

The barrel piston surface profile, shown in Figure 5.3, was investigated by varying the radius of the barrel and also varying the location of the apex in order to better understand the effect that each design parameter had on the performance of the piston cylinder interface. The radius of the barrel was varied by changing the bottom radius (R_1) and the top radius (R_3); a ratio of R_1/R_2 and a ratio of R_3/R_2 was varied from 0.9980 to 0.9998 simultaneously in consistent increments as shown in Figure 6.26. The location of the apex was varied by changing the location of the apex in respect to the length of the piston, $L_{Apex}/L_{length\ piston} = 0.0833$ to 1 in consistent increments as shown Figure 6.27. In this case, the clearance between the piston and the cylinder ($RC=0.96$) remained constant throughout the study. A complete table of the combinations of the radius and location of the apex of the barrel of this optimization study can be seen in Table 6.3.

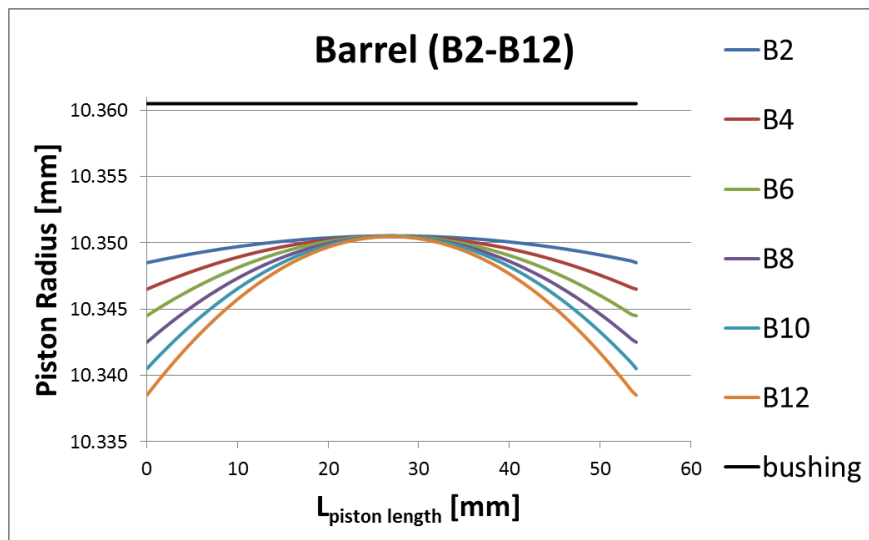


Figure 6.26. Varying radii of the barrel piston surface profile.

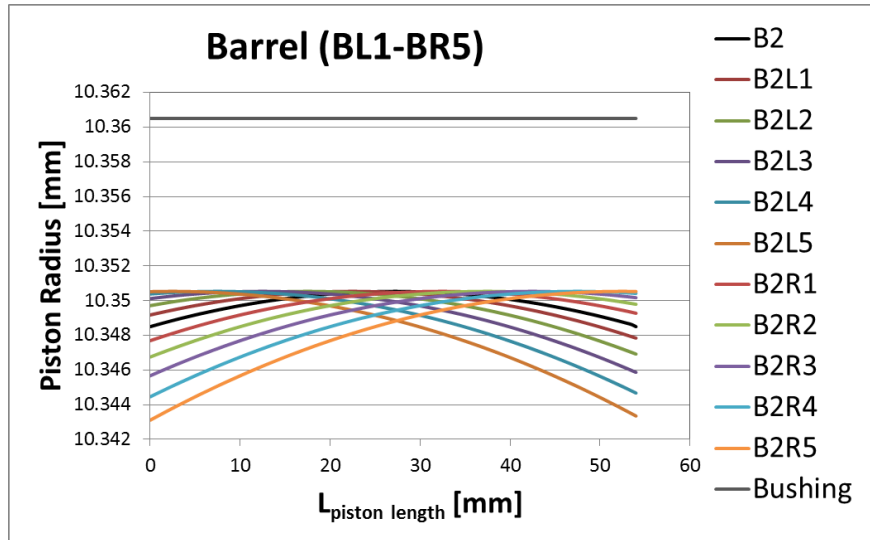


Figure 6.27. Varying apex location of the barrel piston surface profile.

Table 6.3. Complete combination list of design parameters for barrel design study.

Radius (R_1 and R_3) (mm)	Location of Apex (mm)
10.3485	0, 4, 9, 14, 19, 24, 29, 34, 39, 44, 49
10.3465	0, 4, 9, 14, 19, 24, 29, 34, 39, 44, 49
10.3445	0, 4, 9, 14, 19, 24, 29, 34, 39, 44, 49
10.3425	0, 4, 9, 14, 19, 24, 29, 34, 39, 44, 49
10.3405	0, 4, 9, 14, 19, 24, 29, 34, 39, 44, 49
10.3385	0, 4, 9, 14, 19, 24, 29, 34, 39, 44, 49

The decrease in energy dissipation from the baseline, Figure 6.28-Figure 6.31, is considered for the various radii and locations of the apex on the barrel piston surface profile. This simulation study was conducted for the various operating conditions at full displacement (operating conditions 1-4). For operating condition 1, B2-B6 with a shift of L5-L4 are the best. As the barrel surface profiles are shifted right (L1-R5), the decrease in energy dissipation declines and the lower radii result in larger decreases in energy dissipation.

As the operating pressure increases for operating condition 2, it is shown that the smaller the radii the better. Among all of the various radii of the barrel, the best shift is in the middle (L1-R1). As the barrel surface profile is shifted further to the right, the critical minimum gap heights become too large for numerical convergence of the code. In general at this operating condition, the larger the radii of the barrel, the larger the impact

that the shift has on the energy dissipation. As the speed increases to operating condition 3, the larger radii (B6 –B12) tend to be better than the smaller radii for the left shift. Again it is the case that the shift has a larger effect on the larger radii resulting in the mid shift (L1-M) barrel surface shapes to be very similar no matter the radii. The best shift is the left shift (L5-L3).

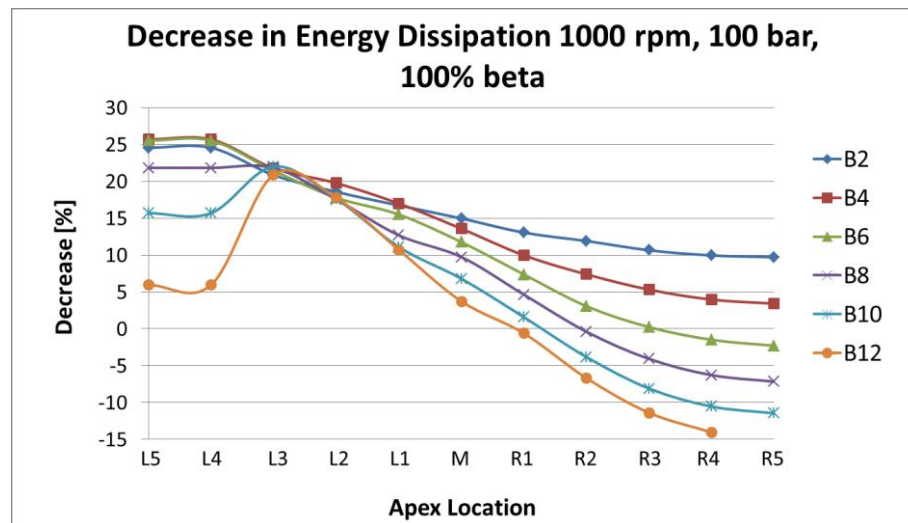


Figure 6.28. Decrease in energy dissipation due to varying the design parameters of the barrel piston surface profile – operating condition 1 - 1000 rpm, 100 bar, 100%.

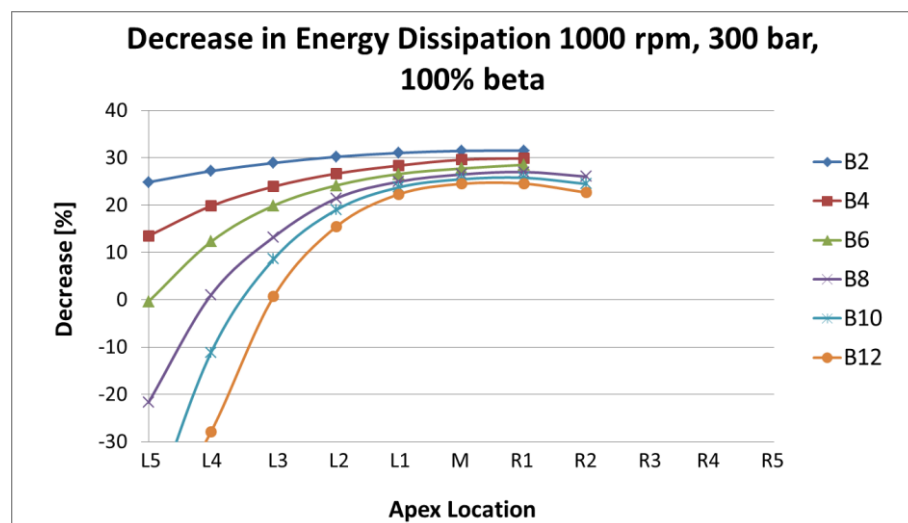


Figure 6.29. Decrease in energy dissipation due to the design parameters of the barrel piston surface profile – operating condition 2 - 1000 rpm, 300 bar, 100%.

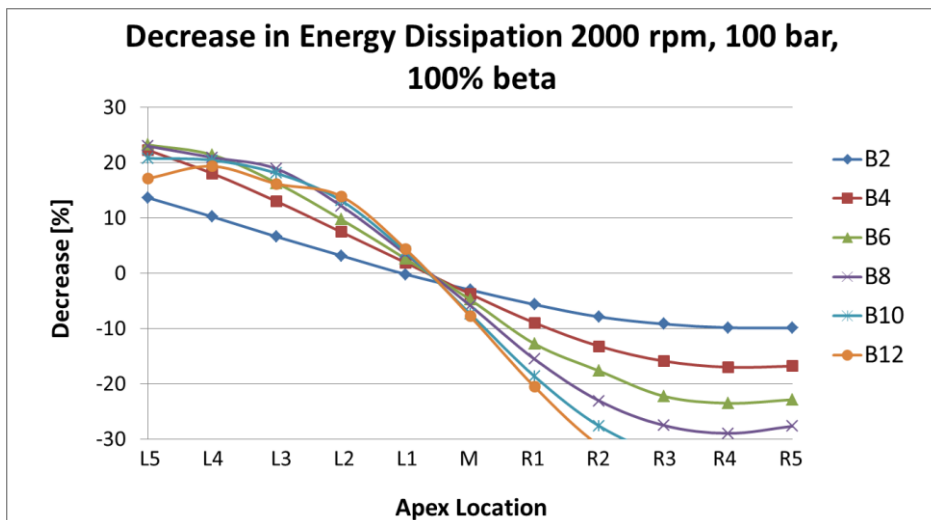


Figure 6.30. Decrease in energy dissipation due to varying the design parameters of the barrel piston surface profile – operating condition 3 - 2000 rpm, 100 bar, 100%.

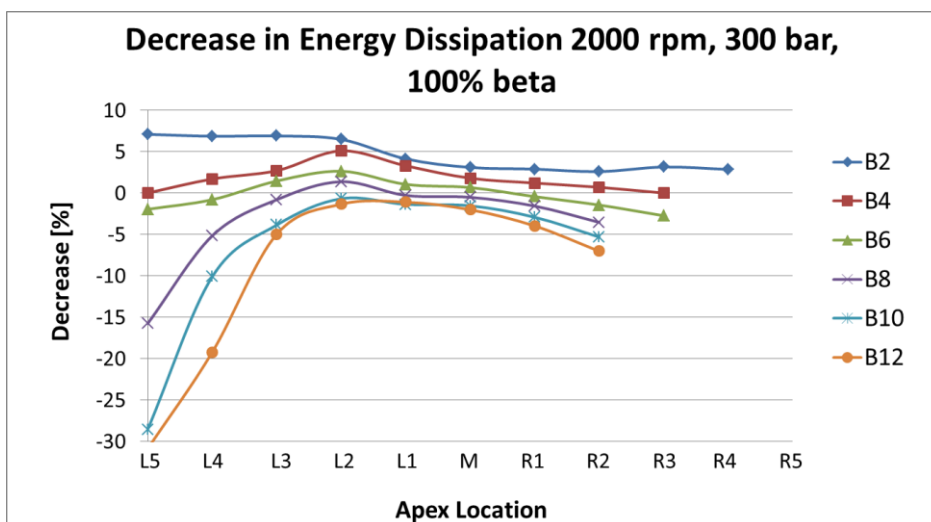


Figure 6.31. Decrease in energy dissipation due to varying the design parameters of the barrel piston surface profile; operating condition 4 - 2000 rpm, 300 bar, 100%.

For the high speed, high pressure common operating condition 4, the smaller the radii the better the decrease in energy dissipation; similar to operating condition 2 with the same pressure. In general, a middle shift is best (L2-R1), but for the B2 radii a left shift is best (L5-L2). Again at the higher pressure operating condition, as the barrel surface profile is shifted further to the right, especially for the larger radii, the areas of critical minimum gap height become too large for numerical convergence of the code. In

general at the higher pressure, the larger the radii of the barrel, the larger the impact that the shift has on the energy dissipation.

Overall for low pressure operating conditions larger radii are best with a left shift while for higher pressure operating conditions, smaller radii are best for a middle shift; speed does not have a large effect on the trends. In order to compromise among the low and high pressure operating conditions, a middle radii is chosen (B6) for a slightly left middle shift (L1). Among the operating conditions, it is shown that the radii of the barrel does not have as large of an impact at a middle shift. The largest difference between the chosen barrel profile and the best for each operating condition is around a 15% decrease in the energy dissipation which is acceptable since this barrel surface profile still improves the energy dissipation from the baseline for the operating conditions considered in this study.

The decrease in leakage from the baseline, Figure 6.32-Figure 6.35, is considered for the various radii and locations of the apex on the barrel piston surface profile for operating conditions 1-4.

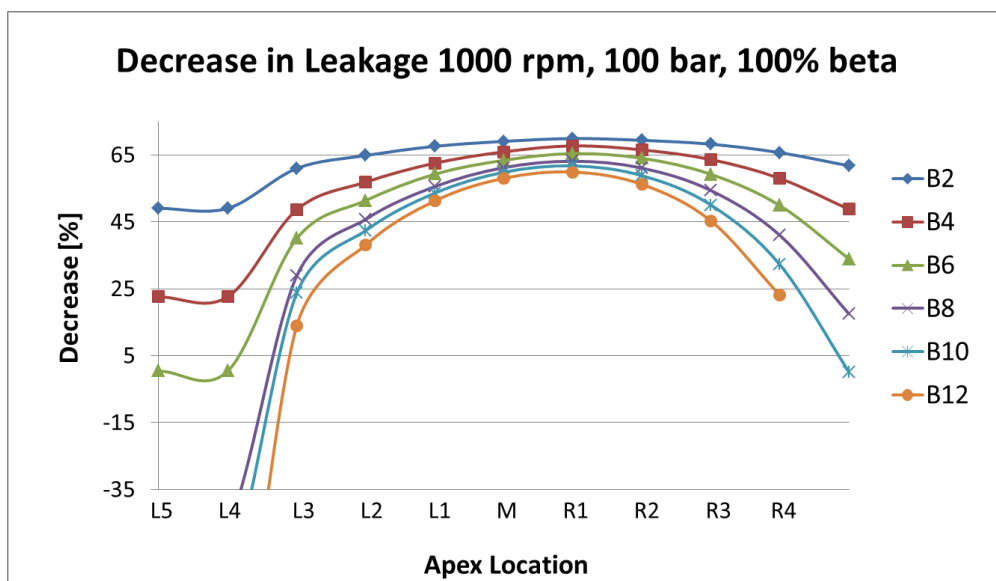


Figure 6.32. Decrease in leakage due to varying the design parameters of the barrel piston surface profile – operating condition 1 - 1000 rpm, 100 bar, 100%.

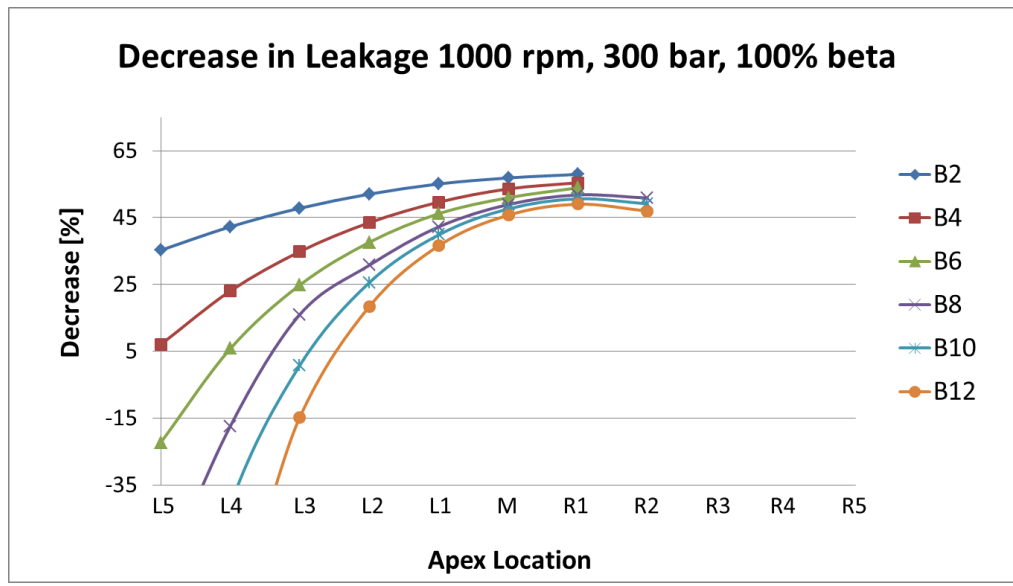


Figure 6.33. Decrease in leakage due to the design parameters of the barrel piston surface profile – operating condition 2 - 1000 rpm, 300 bar, 100%.

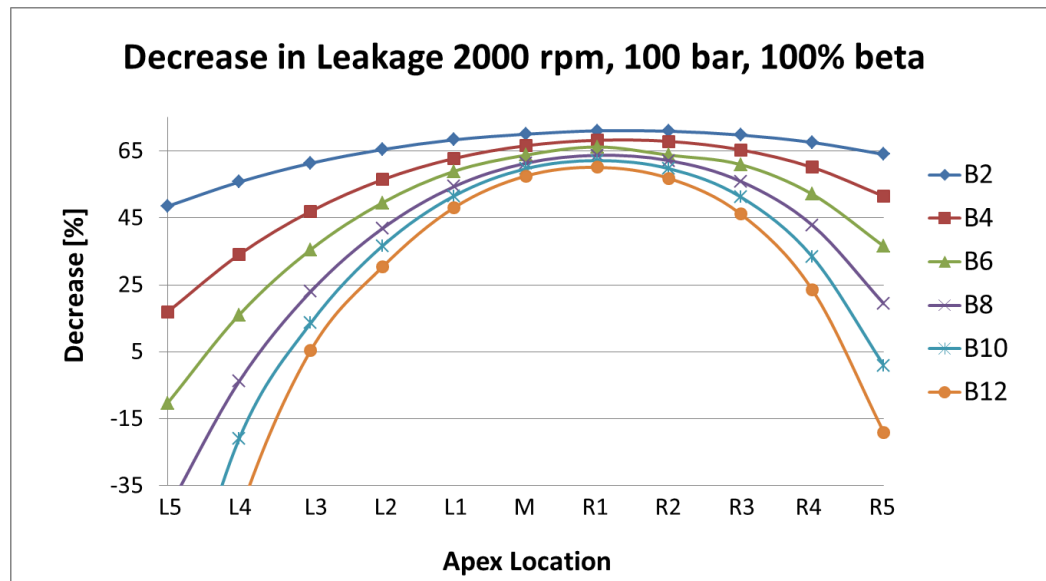


Figure 6.34. Decrease in leakage due to varying the design parameters of the barrel piston surface profile – operating condition 3 - 2000 rpm, 100 bar, 100%.

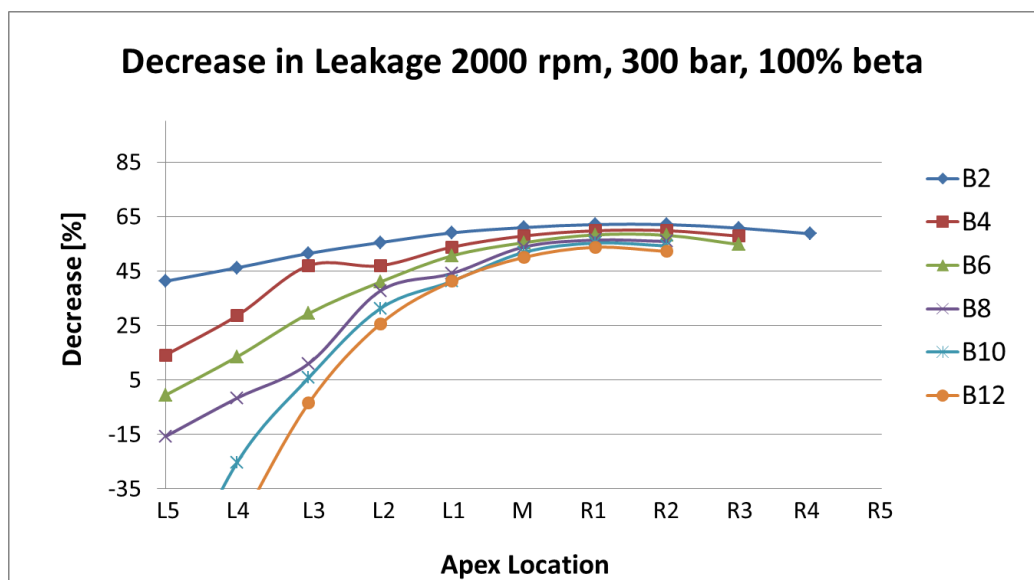


Figure 6.35. Decrease in leakage due to varying the design parameters of the barrel piston surface profile – operating condition 4 - 2000 rpm, 300 bar, 100%.

Among all of the operating conditions shown above, the decrease in leakage is largest the smaller the radii. The decrease is also largest in the middle shift (L1-R3) of the location of the apex of the barrel surface profile. This means that the higher operating pressure follow the same trend in energy dissipation as the leakages; the leakages have a large influence on the energy dissipation as the torque loss do not change much as the barrel changes. For the lower pressure operating conditions, the torque losses have a larger influence on the energy dissipation; as the leakages decrease, the torque increases. This is due to the fact that as the gap between the piston and the cylinder is decreased by the motion of the piston within the bore a seal is created decreasing the leakage, but simultaneously the torque is increased since the fluid pressure is not as able to support the load at such a low operating condition.

6.3.1 Vary Radius

In order to show the impact that varying the radius of the ends of the barrel surface profile, a constant shift was chosen. For the case shown below, a left shift of L5 was chosen at operating condition 4. At this shift, the effect that the radius has on the performance of the interface should be most apparent since at this shift there is a large difference in the energy dissipation as shown previously.

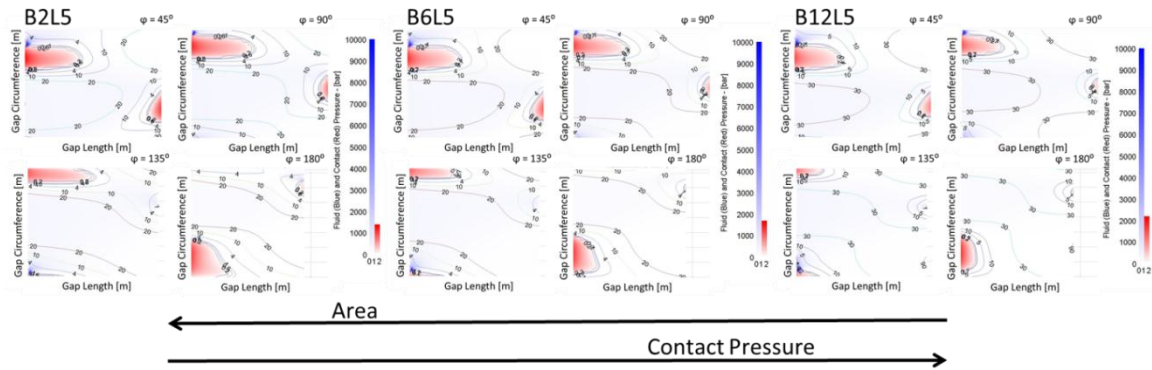


Figure 6.36. Varying radii of the barrel piston surface profile multi-plots, operating – condition 4; 2000 rpm, 300 bar, 100%.

As the radius increases for the ends of the barrel surface profile at this operating condition, it can be seen that the area of critical minimum fluid film thicknesses decreases, but the contact pressure of those areas increases. This means that as the radius increases there is more area for the fluid to leak from the gap in which an insufficient seal is created while the contact pressure is also slightly increasing resulting in a slight increase in the torque losses as well at this apex location. This is why there is such a large difference among the radii for the energy dissipation.

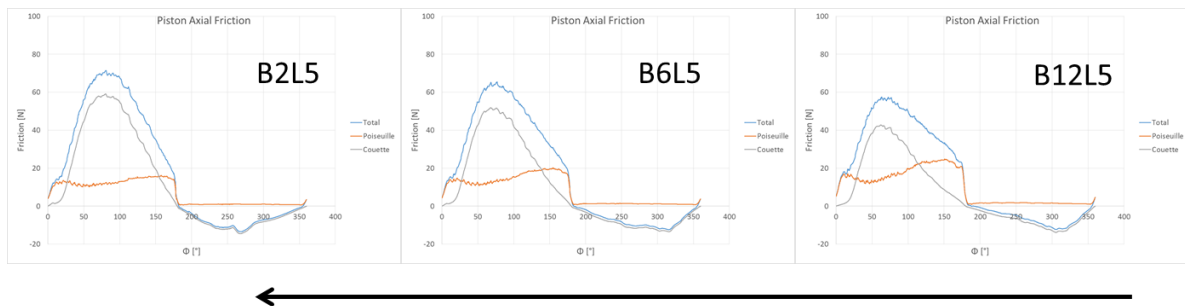


Figure 6.37. Varying radii of the barrel piston surface profile piston axial friction forces – operating condition 4; 2000 rpm, 300 bar, 100%.

The increase in the radii of the ends of the barrel surface profile actually decreases the piston axial friction forces. The reason for this is depicted in the multi-plots shown above. The areas of the critical fluid film thickness are larger at the lower radii and although the contact pressures increase with the larger radii, this is not considered in the

code, therefore the friction forces are calculated to be larger according to the larger areas of critical minimum fluid film.

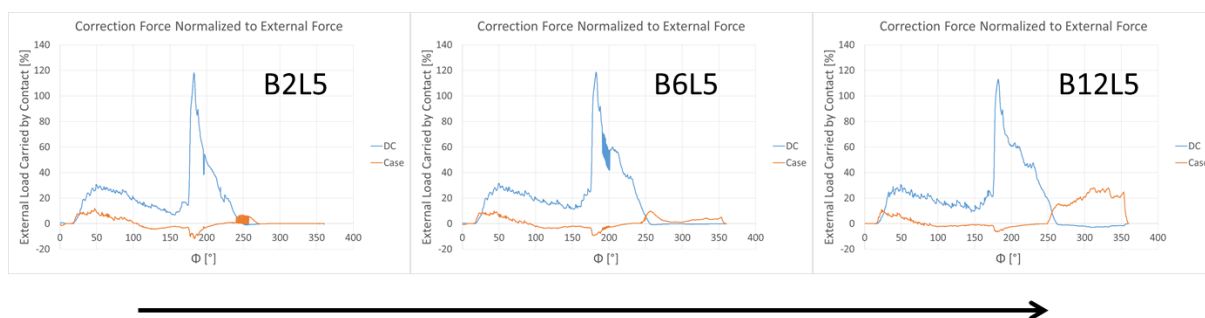


Figure 6.38. Varying radii of the barrel piston surface profile correction forces normalized to external force – operating condition 4; 2000 rpm, 300 bar, 100%.

When it comes to the correction force normalized to the external forces, it can be seen that as the end radii of the barrel increase, the load carried by the contact also slightly increases meaning that more critical minimum fluid film thickness is occurring which leads to a slight increase in torque. Along with the large increase in the leakages shown, this in turn results in the increase that was produced in the energy dissipation.

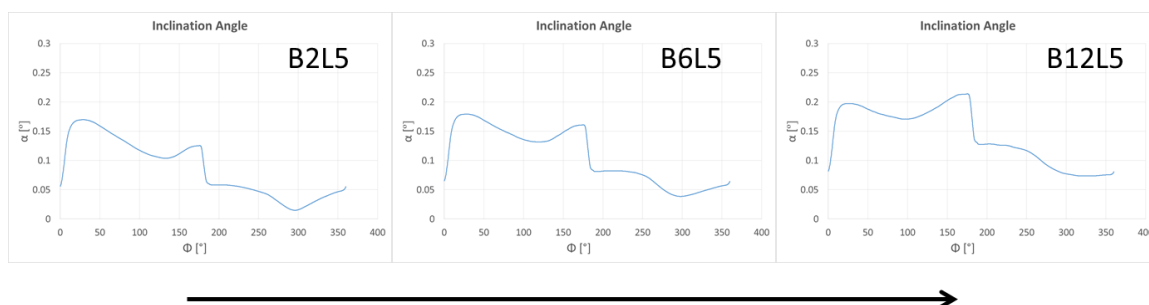


Figure 6.39. Varying radii of the barrel piston surface profile inclination angles – operating condition 4; 2000 rpm, 300 bar, 100%.

As expected, the inclination angle increases as the radius of the ends of the barrel increases. As the radii of the ends of the barrel increase, the piston can tilt more in the bore. Although, the angle does not increase as much as it possibly could and this is the reason that the leakage is better at the lower end radii; a better seal between the piston and the cylinder is created reducing the leakage in the gap.

6.3.2 Vary Apex Location

In order to show the impact that the location of the apex of the barrel surface profile has on the results, a constant radii was chosen. For the case shown below, a large radii B12 was chosen at operating condition 4. At this radii, the effect that the location of the apex has on the performance of the interface should be most apparent since it was previously shown that the larger the radii the larger the effect on the energy dissipation.

As the location of the apex shifts from the left to the right, the area of critical minimum fluid film thicknesses increases, but the contact pressure decreases. This means that with the shift of the apex, there is less area for the fluid to leak from the gap in which a better seal is created. The contact pressure slightly decreases from the left to the middle reducing the torque losses and then remains similar as further shifted right. This explains why the energy dissipation shows larger differences between the apex locations to the left. The effect the center and right apex location has on the energy dissipation mainly relies on the decrease in leakage.

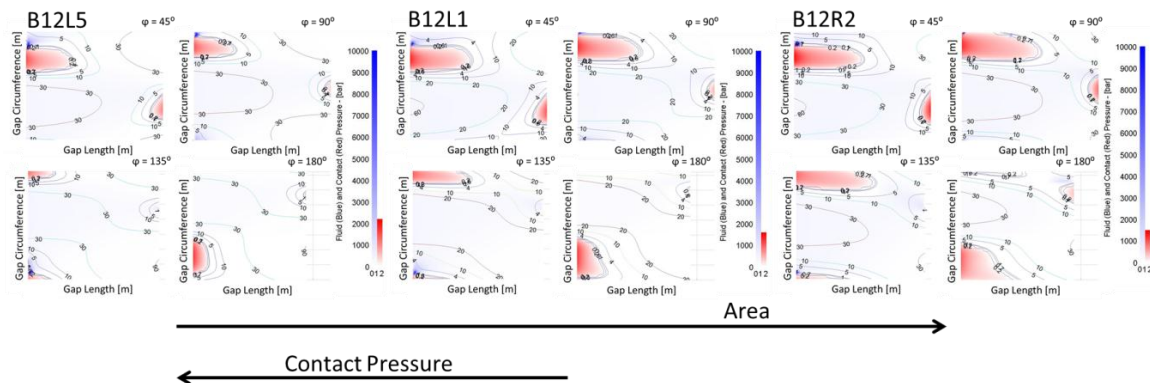


Figure 6.40. Varying apex location of the barrel piston surface profile multi-plots – operating condition 4; 2000 rpm, 300 bar, 100%.

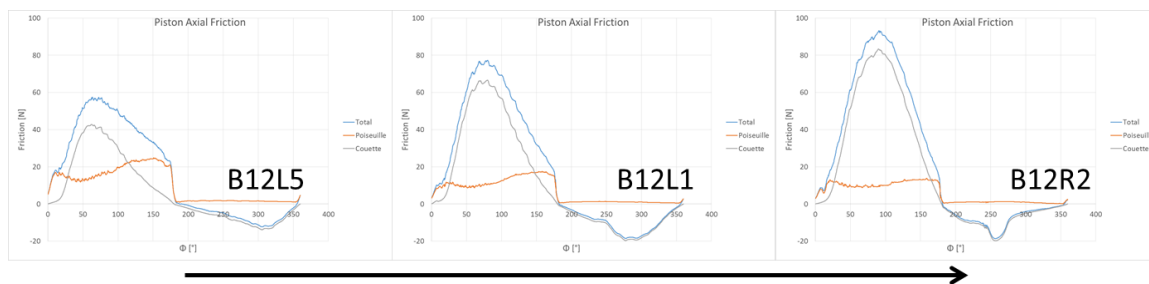


Figure 6.41. Varying apex location of the barrel piston surface profile piston axial friction forces – operating condition 4; 2000 rpm, 300 bar, 100%.

The shift of the location of the apex from the left to the right increases the piston axial friction forces. The reason for this is again depicted in the multi-plots shown above as the areas of the critical fluid film thickness also increase. Again, since the impact of the contact pressures are not considered in the code, the friction forces are calculated to be larger according to the larger areas of critical minimum fluid film.

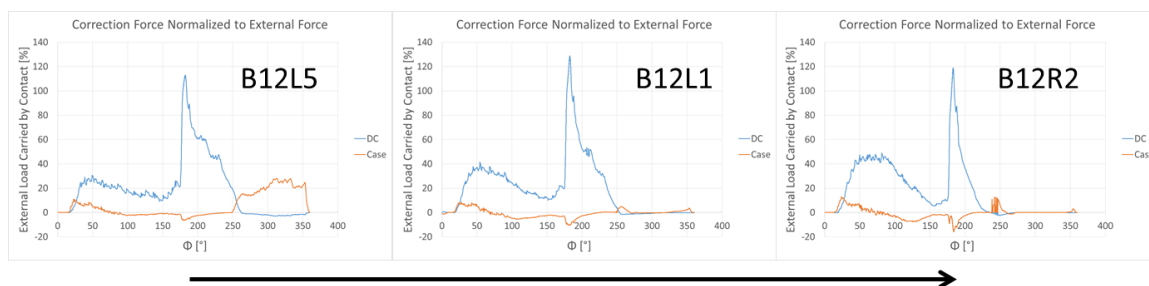


Figure 6.42. Varying apex location of the barrel piston surface profile correction forces normalized to external force – operating condition 4; 2000 rpm, 300 bar, 100%.

When it comes to the correction force normalized to the external forces, the piston must be corrected in order to prevent penetration of the bushing. Therefore as expected, the corrections based on contact are more as the areas of minimum fluid film thickness are increased.

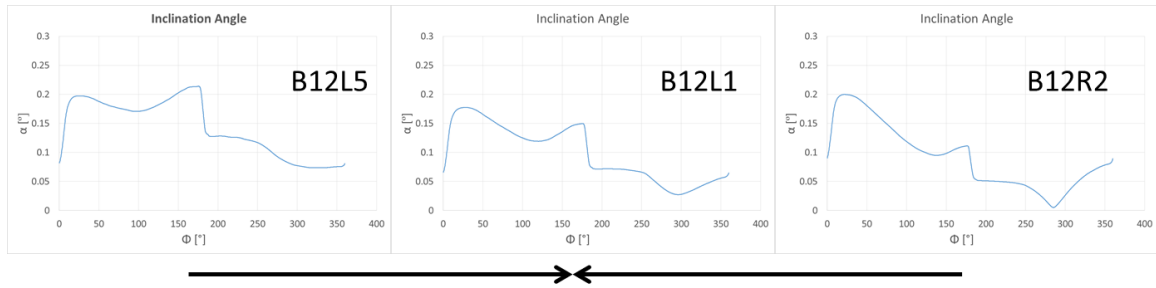


Figure 6.43. Varying apex location of the barrel piston surface profile inclination angles – operating condition 4; 2000 rpm, 300 bar, 100%.

As expected, the inclination angle increases as the location of the apex shifts towards the ends of the barrel. As the slope of the barrel increase at the ends, the piston can tilt more in the bore. It can also be seen that through the high pressure stroke the left shifted barrel surface profile (larger slope at the case end) remains tilted since there is very little minimum fluid film thickness to correct the piston to the center of the bore in which it then remains tilted throughout the low pressure stroke in which the fluid is pushed out with the motion of the piston. With this being the case, a seal is not created between the piston and the bushing causing a great deal of leakage. As for the more centered apex location (L1) the piston cannot tilt as the others considering that one end does not have a larger incline. For this reason, the piston tends to remain more centered in the bore although the slight tilt that the geometry allows for creates more of a seal reducing the leakages. As the piston is even further shifted to the right, the leakage is again further reduced as the piston tilts during the high pressure stroke and then as minimum fluid film thickness occurs is corrected to be more centered during the low pressure stroke creating a better seal in the gap and not pulling fluid out with its motion.

CHAPTER 7. INVESTIGATION OF PISTON MICRO-SURFACE SHAPING

In this section, a complete analysis of the effects that various micro-surface shapes of the piston have on the performance of the piston/cylinder interface are described; the overall decrease in power loss due to the surface shape along with the effect that the shaping has on the performance will be shown. For the following results shown, in addition to the micro-surface shaping of the piston, the relative clearance was also reduced from the baseline to 0.96. For this study, a larger range of operating conditions were considered as shown in Table 7.1; as previously stated these operating conditions were chosen based on the frequency of use at such conditions, the corner operating conditions of the machine, and for both modes of operation. The trends detailed below will be useful for future design of this lubricating interface.

Table 7.1. Investigation of piston micro-surface shaping operating conditions.

Operating Condition – Pumping ($\beta = 100\%$)	1	2	3	4	Unit
High Pressure	125	325	125	325	bar
Low Pressure	25	25	25	25	bar
Angular Speed	1000	1000	2000	2000	rpm
Swash Plate Angle	17	17	17	17	°

Operating Condition – Pumping ($\beta = 20\%$)	5	6	7	8	Unit
High Pressure	125	325	125	325	bar
Low Pressure	25	25	25	25	bar
Angular Speed	1000	1000	2000	2000	rpm
Swash Plate Angle	3.4	3.4	3.4	3.4	°

Table 7.1. Continued.

Operating Condition – Pumping ($\beta = 100\%$)	9	10	11	Unit
High Pressure	425	425	425	bar
Low Pressure	25	25	25	bar
Angular Speed	1000	2000	2800	rpm
Swash Plate Angle	17	17	17	°

Operating Condition – Motoring ($\beta = 100\%$)	12	13	14	15	Unit
High Pressure	150	275	150	275	bar
Low Pressure	50	50	50	50	bar
Angular Speed	1000	1000	2000	2000	rpm
Swash Plate Angle	17	17	17	17	°

The design parameters considered in this study are detailed in Table 7.2 below. The design parameter of the sine wave, flat, and barrel surface profiles were chosen based on the results in the previous section. The design parameters of the waved barrel were chosen as a combination of the best design parameters of the sine wave and the barrel surface profiles while maintaining the location of the apex since that was shown to have an effect on the results. For the circ sine wave surface profiles, the amplitude was chosen as the best in the sine wave design study while the number of waves was arbitrarily chosen.

Table 7.2. Investigation of piston micro-surface shaping design parameters.

Surface Profile	Design Parameter			
	Amplitude (μm)	Number of Waves	Shift	Radius
Sine Wave	3	2.5	-	-
Flat	3	-	-	-
Barrel	-	-	L1	B6
Waved Barrel	3	2.5	L1	B6
Circ Sine Wave	3	6	-	-

7.1 Pumping, Full Displacement

The decrease in energy dissipation from the baseline as described in Section 4.3.2, Figure 7.1 (pumping, full displacement) is considered for the six previously described micro-surface shapes on the piston that were shown in Figure 5.1 to Figure 5.6 and further described in Table 7.2. This simulation study was conducted for the various operating conditions shown in Table 7.1 (operating conditions 1-4, 9-11).

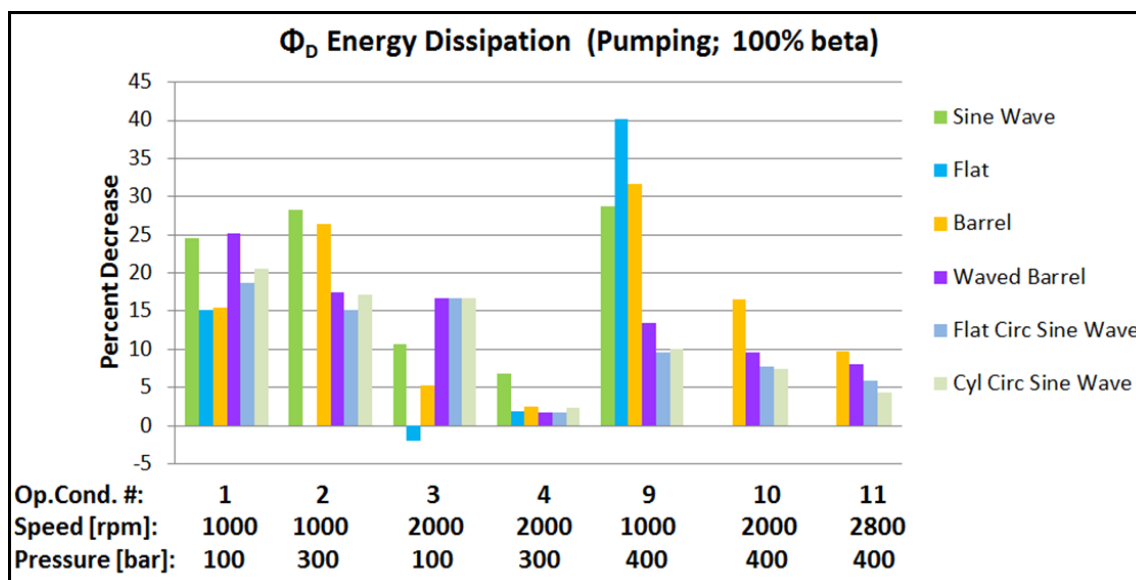


Figure 7.1. Decrease in energy dissipation due to micro-surface shaping of the piston; pumping, full displacement (operating conditions 1-4, 9-11).

The effect that each surface shape has on the energy dissipation in comparison to the baseline for pumping, full displacement is shown in Figure 7.1. This decrease can reach up to around 40% for the flat surface profile while the barrel can cause over a 30% reduction and the sine wave almost a 30% decrease as well. Overall the barrel surface profile results in the best decrease in energy dissipation among the operating conditions shown for pumping mode at full displacement, especially so at the higher operating pressures. The sine wave and flat surface profiles are shown to depend on the operating condition and actually fail to converge at the higher speed and higher pressure operating conditions (operating conditions 10 and 11). It is also apparent that the flat surface profiles also greatly depend on the operating speed; performing much better at the lower

speeds. The waved barrel along with the circ sine wave surface profiles also reduce the energy dissipation for pumping, full displacement even outperforming the barrel at lower pressures. Among the two circ sine wave profiles, the flat and the cylindrical tend to produce very similar results even further verifying that the amplitude at the ends has a very modest consequence on the results.

The decrease in leakage from the baseline for pumping, full displacement (operating conditions 1-4, 9-11) for the six micro-surface shapes on the piston is shown in Figure 7.2.

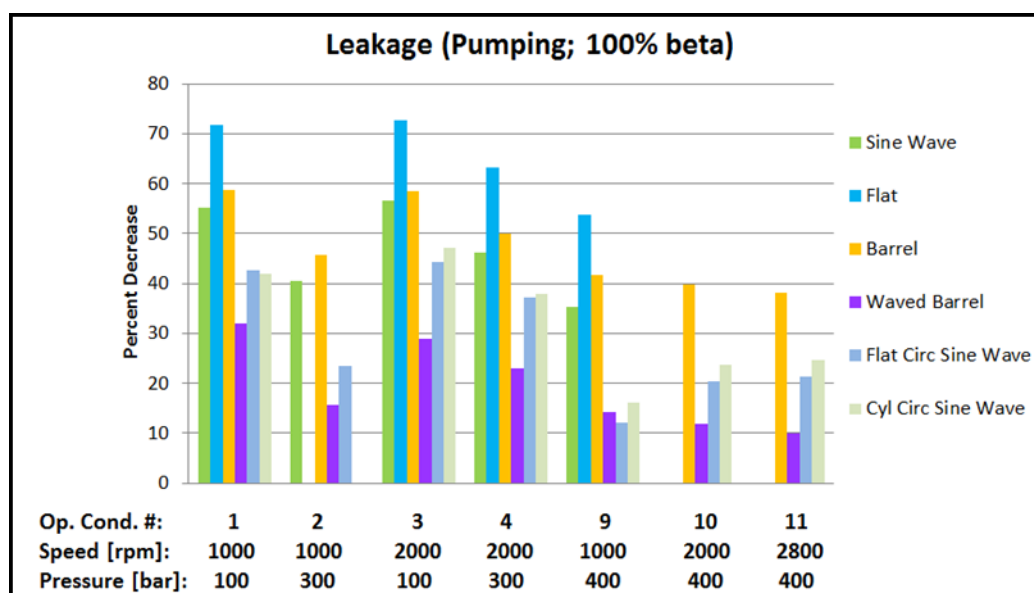


Figure 7.2. Decrease in leakage due to micro-surface shaping of the piston; pumping, full displacement (operating conditions 1-4, 9-11).

The effect that each surface shape has on the leakage in comparison to the baseline for full displacement is shown in Figure 7.2. This decrease can reach up to over 70% for the flat surface profile and is not dependent on the operating speed; the torque is greatly increased with the speed effecting the energy dissipation as shown in Figure 7.3 and Figure 7.5 below. Therefore, the reduction in leakage is entirely based on the 60% reduction in clearance from the baseline and even then would be difficult to achieve in manufacturing as the tolerances could not be maintained over the flat surface of the gap length on the piston. The next largest reduction in leakage shown for pumping at full

displacement is due to the introduction of the barrel surface shape, resulting in over a 60% reduction. In this case, since the barrel surface profile is also the best for decreasing energy dissipation over the operating conditions shown, not only are the leakages being greatly reduced due to the reduced clearance between the piston and the cylinder, but the torque is in turn not increasing largely as shown below in Figure 7.9. The circ sine surface profiles also result in larger leakage losses, around a 45% decrease while the waved barrel results in much smaller reductions among the operating conditions. Considering the energy dissipation is similar, this means that the waved barrel performs better in terms of reducing the friction, as shown in Figure 7.11, Figure 7.13 at the reduced clearance while both the waved barrel and the circ sine wave surface profiles rely more so on reduced friction forces at lower pressures, as shown in Figure 7.13. Overall, the addition of a surface profile allows for the reduction in clearance, but this decrease must be balanced between the leakage decreasing and the torque losses increasing as described.

Shown below are the piston axial friction forces, the deformations, and also corrections for various surface profiles at various operating speeds in order to support the claims made above while further validating the performance of the interface with the introduction of a surface profile on the piston.

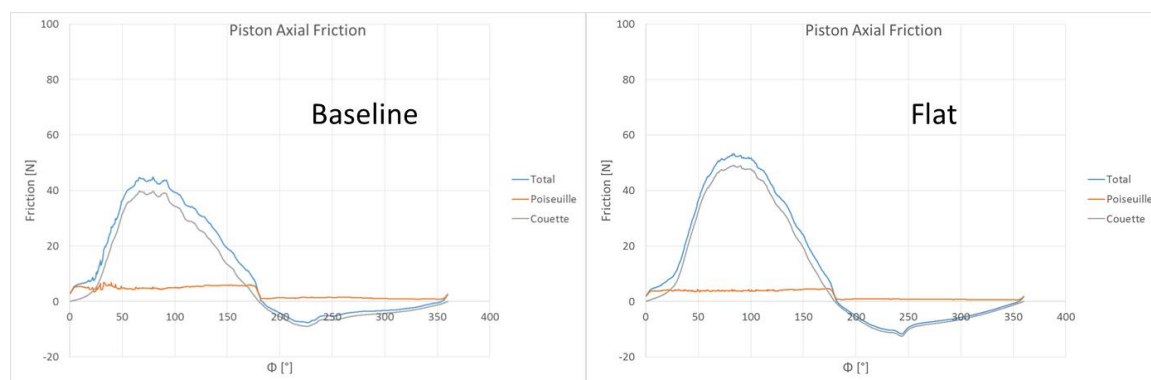


Figure 7.3. Flat vs. baseline piston axial friction, operating condition 3; pumping, 2000 rpm, 100 bar, 100%.

As can be seen, for the flat surface profile in comparison to the baseline, the friction forces are greatly increased and in turn the torque losses are increased accounting for the less of a decrease in energy dissipation at the higher operating speeds.

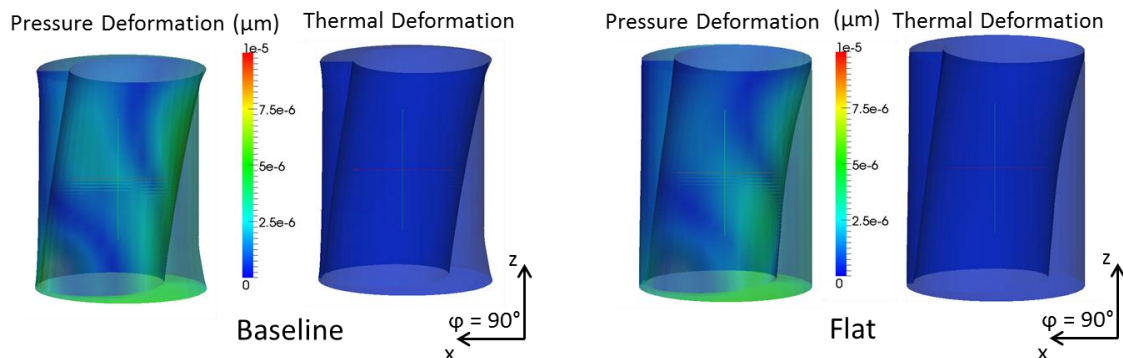


Figure 7.4. Flat vs. baseline deformations, operating condition 3; pumping, 2000 rpm, 100 bar, 100%.

The pressure and thermal deformations of the flat surface profile are very similar to that of the baseline. Note that the fluid thickness is slightly different based on the decrease in clearance between the two; the larger clearance between the piston and the cylinder for the baseline allows the piston to tilt more hence the larger fluid film thicknesses on the opposing circumferential sides of the piston at both ends.

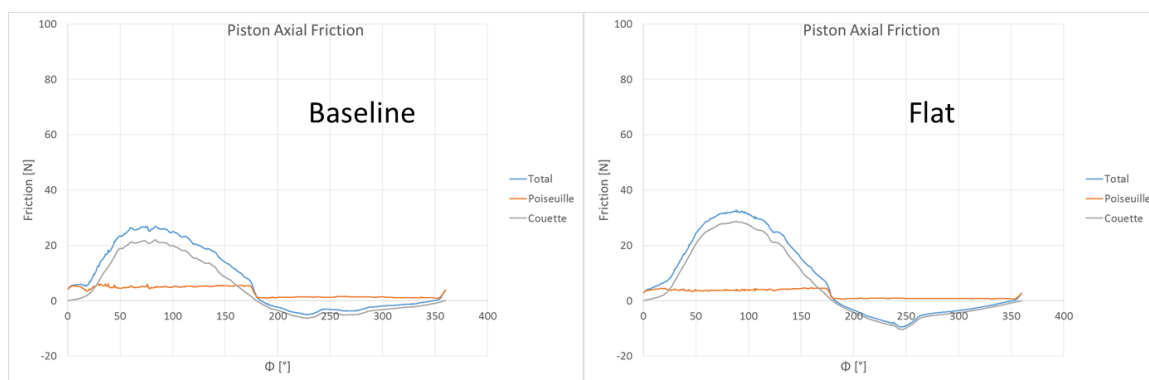


Figure 7.5. Flat vs. baseline piston axial friction, operating condition 1; pumping, 1000 rpm, 100 bar, 100%.

For the lower operating speed, the torque losses are also slightly increased as can be seen in the piston axial friction forces above, but in this case, it is not as detrimental and the decrease in energy dissipation still heavily relies on the large decrease in leakage.

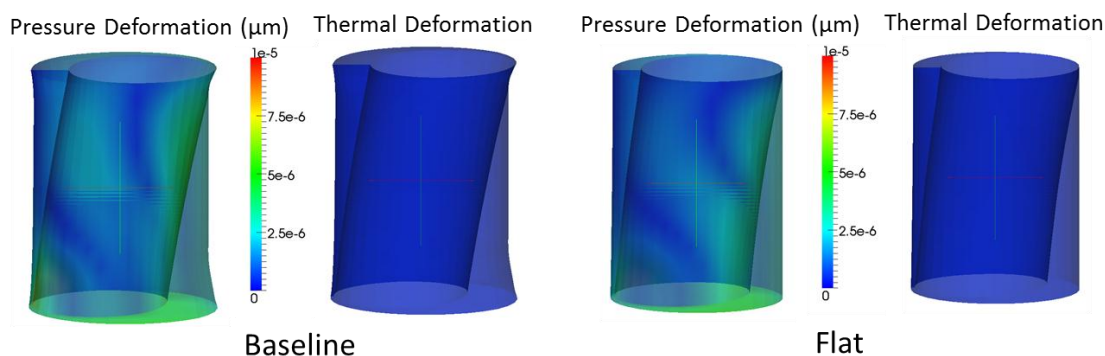


Figure 7.6. Flat vs. baseline deformations, operating condition 1; pumping, 1000 rpm, 100 bar, 100%.

Again, the deformations between the baseline, cylindrical piston and the flat surface profile piston are quite similar. The flat tends to deform slightly less throughout the high pressure stroke though, and this accounts for the smaller increase in the axial friction forces as the fluid film is more sufficient to support the load at the lower speeds.

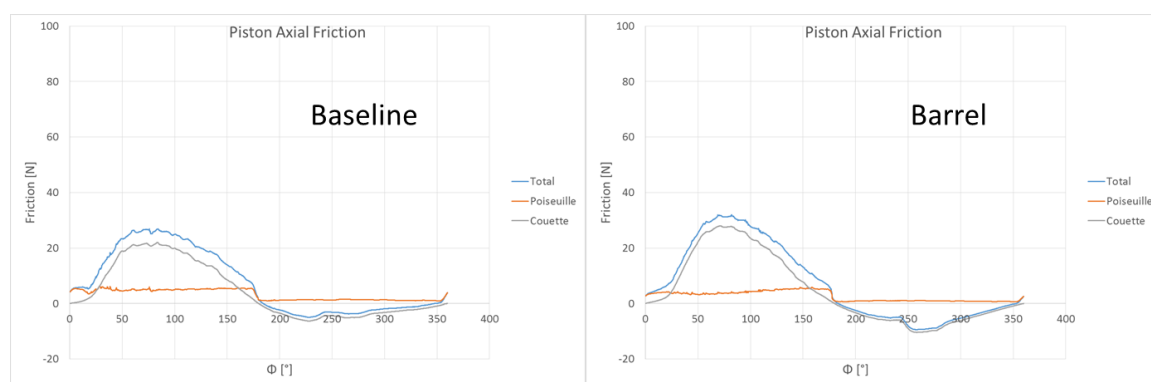


Figure 7.7. Barrel vs. baseline piston axial friction, operating condition 1; pumping, 1000 rpm, 100 bar, 100%.

The barrel surface friction profile in comparison to the baseline also slightly increases the friction forces at the lower operating conditions similar to that of the flat surface profile.

This in turn explains the similar reductions between the barrel and the flat surface profile for the lower operating conditions.

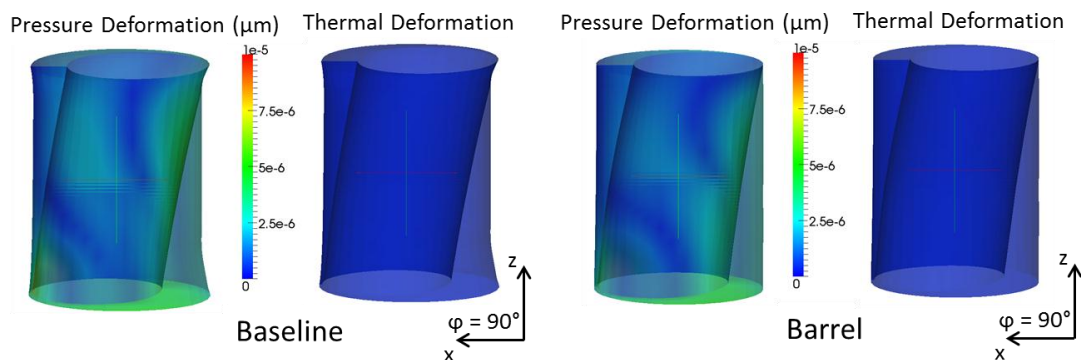


Figure 7.8. Barrel vs. baseline deformations, operating condition 1; pumping, 1000 rpm, 100 bar, 100%.

The deformations between the baseline and the barrel surface profile piston are quite similar although similarly to the flat tends to deform slightly less throughout the high pressure stroke of the lower pressure operating condition leading to comparable axial friction forces.

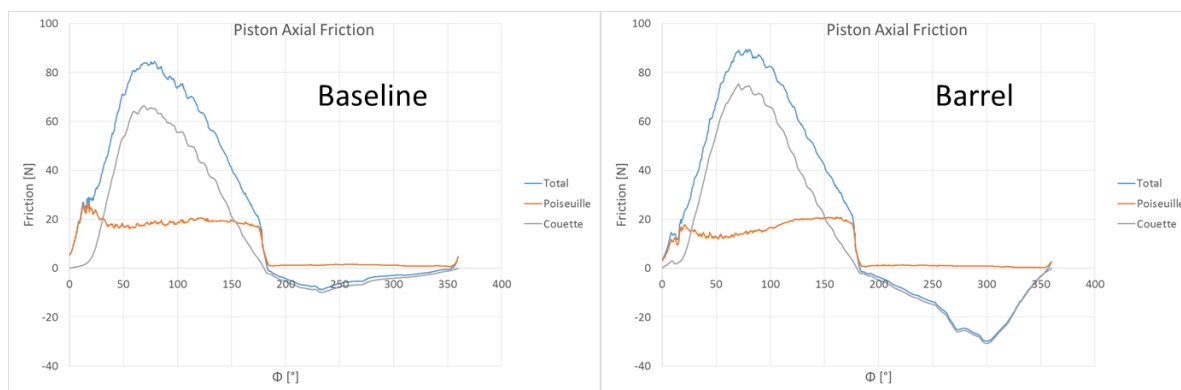


Figure 7.9. Barrel vs. baseline piston axial friction, operating condition 11; pumping, 2800 rpm, 400 bar, 100%.

For the higher operating conditions (high speed and high pressure), the torque losses are for the barrel surface profile are very similar to that of the baseline. This is why

that at the higher operating conditions, the barrel performs best; the leakage is greatly decreased while the friction forces are not increasing.

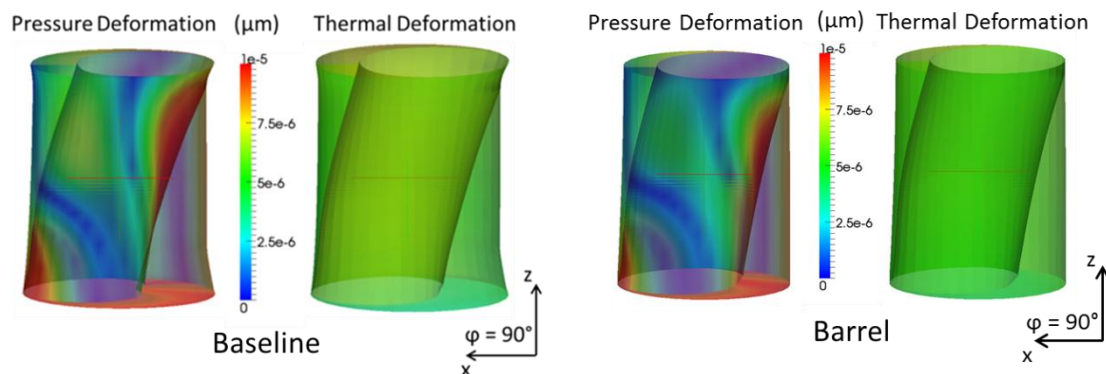


Figure 7.10. Barrel vs. baseline deformations, operating condition 11; pumping, 2800 rpm, 400 bar, 100%.

The location of the deformations are similar to those of the baseline with the introduction of a barrel surface profile, but again the magnitude of the deformations are slightly reduced.

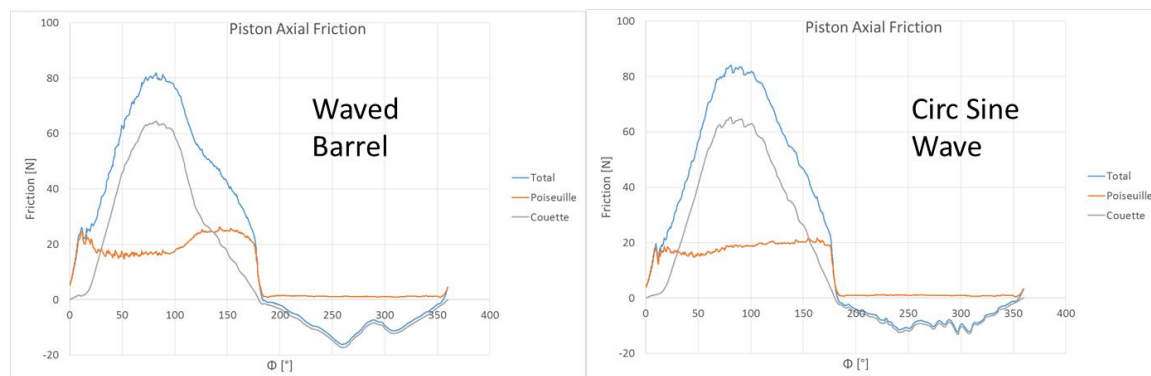


Figure 7.11. Waved barrel vs. circ sine wave piston axial friction, operating condition 11; pumping, 2800 rpm, 400 bar, 100%.

Waved barrel and circ sine wave result in similar piston axial friction forces in which the waved barrel is slightly less hence the larger decrease in energy dissipation seen throughout the pumping mode, full displacement operating conditions. These two surface profiles result in decreased piston axial friction forces in comparison to the baseline and the barrel surface profile. With this being the case, the wave barrel, circ sine,

and the barrel surface profile result in similar decreases in energy dissipation in combination with the smaller decreases in leakages resulting from the addition of a waved barrel or circ sine wave at high pressure operating conditions.

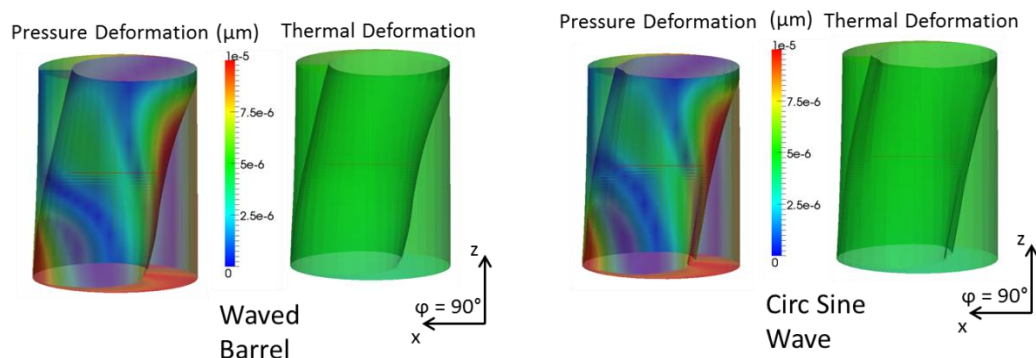


Figure 7.12. Waved barrel vs. circ sine wave deformations, operating condition 11; pumping, 2800 rpm, 400 bar, 100%.

The deformations for the waved barrel and the circ sine wave are very similar to that of the barrel surface profile, slightly reducing the deformations from the baseline.

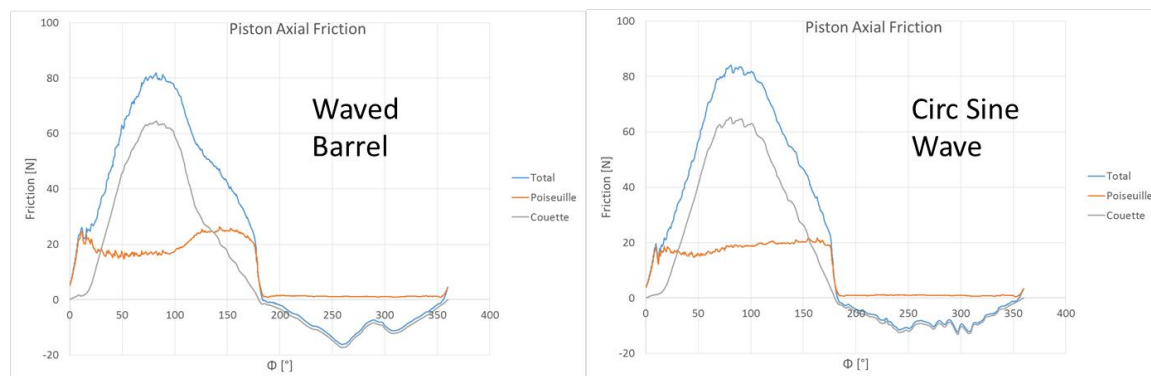


Figure 7.13. Waved barrel vs. barrel piston axial friction, operating condition 1; pumping, 1000 rpm, 100 bar, 100%.

As for lower pressure operating conditions, the waved barrel actually performs better than the barrel even though the decrease in leakages are less. As previously explained this is due to the larger decrease in piston axial friction forces with the addition of the waved barrel surface profile as shown above.

Shown below are the normalized contact forces between the piston and the cylinder over one shaft revolution. The normalized contact force is the correction forces applied in order to prevent penetration with respect to the external forces being exerted on the piston.

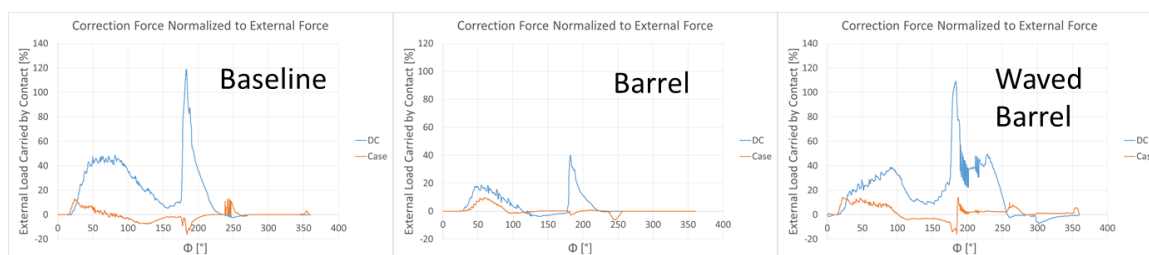


Figure 7.14. Waved barrel vs. barrel vs. corrections, operating condition 11; pumping, 2800 rpm, 400 bar, 100%.

Another important thing to note for the barrel surface profile is that it greatly reduces the corrections as compared to the baseline and the waved barrel. This in turn results that the load carried by the fluid is improved as the additional numerical correction force is not as necessary in preventing penetration of this piston through the bushing.

7.2 Pumping, Partial Displacement

The decrease in energy dissipation from the baseline as shown in Figure 7.15 is considered again for the six micro-surface shapes on the piston for partial displacement in pumping mode (operating conditions 5-8). Note that as previously stated, the 1000 rpm, 300 bar, 20% beta, operating condition 6, would not numerically converge with the code and therefore is not shown in the simulated results.

The effect that each surface shape has on the energy dissipation in comparison to the baseline for pumping, partial displacement is shown in Figure 7.15. This decrease can reach up to around 40% for the flat and the circ sine wave surface profiles which are the best performing surface profiles among the partial displacement operating conditions shown. The barrel surface profile also performs well for the partial displacements, up to nearly a 35% reduction. The waved barrel and the sine wave surface profiles tend to fall

short at the partial displacement operating conditions, especially at low pressures. The decrease in leakage from the baseline for pumping, partial displacement (operating conditions 5-8) due to the surface shaping of the piston is shown in Figure 7.16.

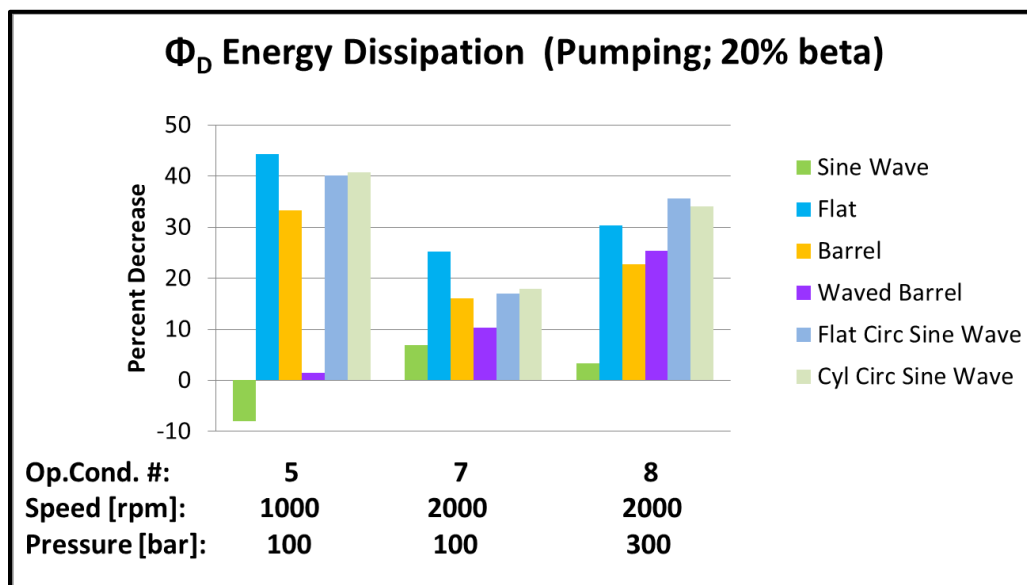


Figure 7.15. Decrease in energy dissipation due to micro-surface shaping of the piston; pumping, partial displacement (operating conditions 5-8).

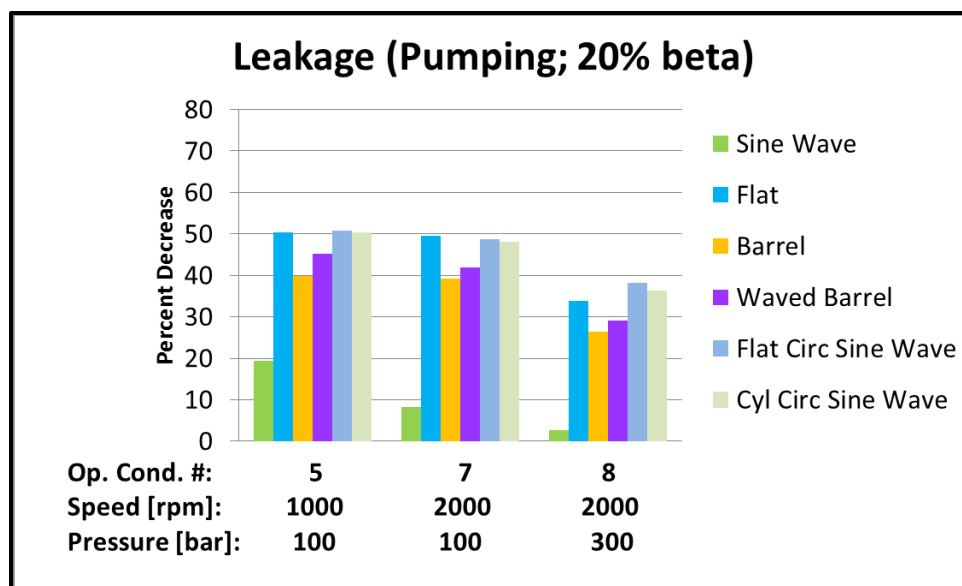


Figure 7.16. Decrease in leakage due to micro-surface shaping of the piston; pumping, partial displacement (operating conditions 5-8).

The effect that each surface shape has on the leakage in comparison to the baseline for partial displacement is shown in Figure 7.16. This decrease can reach up to around 50% for the flat surface profile and the circ sine wave profiles. This trend corresponds with the reduction in energy dissipation implicating that the torque losses have little effect on the overall energy dissipation, shown in Figure 7.17, as the clearance is reduced based on the decreased side loads at partial displacements, the motion of the piston further shown in Figure 7.18.

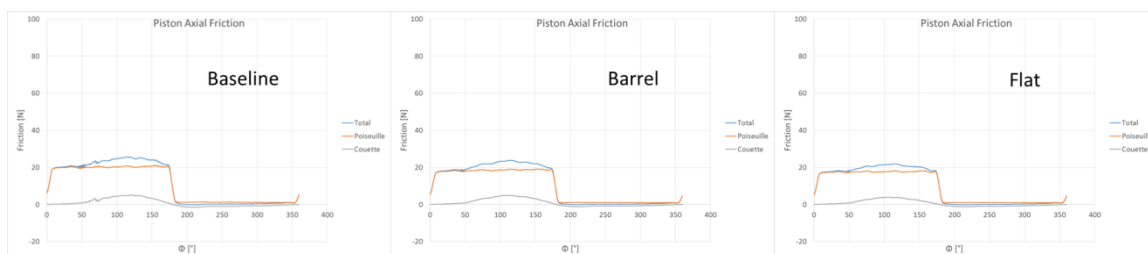


Figure 7.17. Baseline vs. barrel vs. flat piston axial friction, operating condition 8; pumping, 1000 rpm, 300 bar, 20%.

The piston axial friction is shown not to be effected by the addition of various surface profiles for partial displacement; the torque losses do not change therefore the reduction in energy dissipation is mainly reliant on the decrease in leakages due to the decreases clearance between the piston and the cylinder.

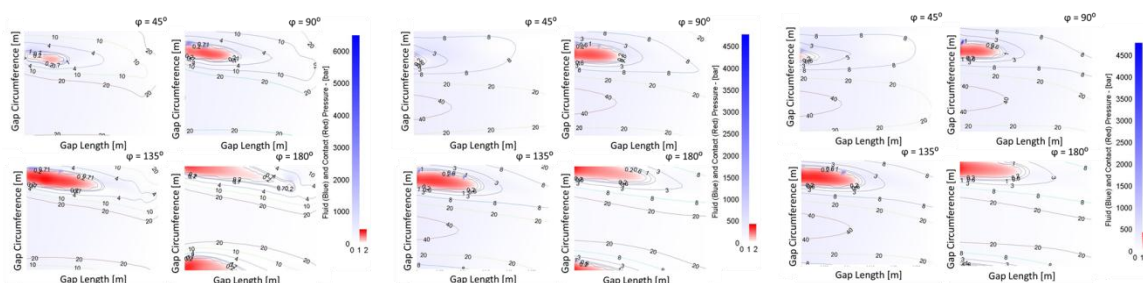


Figure 7.18. Baseline vs. barrel vs. flat multi-plots, operating condition 8; pumping, 1000 rpm, 300 bar, 20%.

The motion of the piston with and without a surface profile is shown to be the same in the multi-plots; critical minimum fluid film thickness occurs in similar locations

and areas. This is due to the reduced side load causing the piston to tilt less within the bushing in which it then tends to scrape along the bushing causing the areas shown as previously described for the baseline simulations.

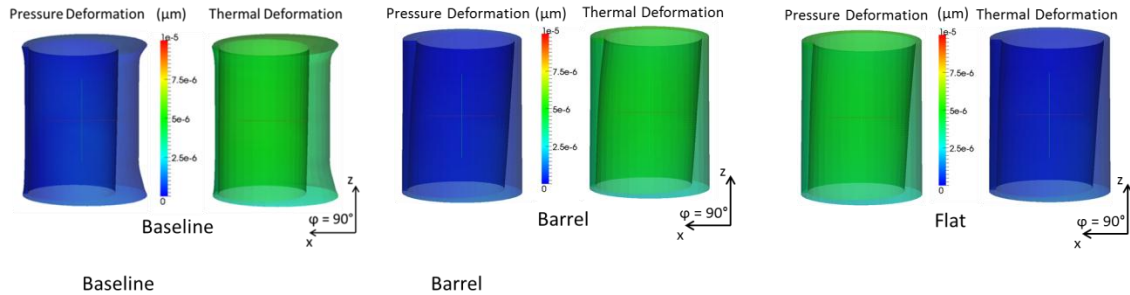


Figure 7.19. Baseline vs. barrel vs. flat deformations, operating condition 8; pumping, 1000 rpm, 300 bar, 20%.

The deformations of the solid bodies due to the thermal and pressure loading also remain very similar with the addition of a surface profile. An apparent difference is again the thicker fluid film of the baseline based on the larger clearance between the piston and the cylinder initially.

7.3 Motoring, Full Displacement

The effect that the six micro-surface shapes has on the energy dissipation for motoring mode, full displacement (operating conditions 12-15) is shown in Figure 7.20. The effect that each surface shape has on the energy dissipation in comparison to the baseline for motoring, full displacement is shown in Figure 7.20. This decrease can reach up to around 30% for the waved barrel surface profile and the circ sine wave surface profiles; the waved barrel outperforming the barrel in motoring mode for all operating conditions studied. The barrel, sine wave, and flat surface profiles show up to nearly a 25% reduction and although not the best in motoring mode still result in a decrease in energy dissipation overall.

The decrease in leakage due to the micro-surface shaping of the surface of the piston for motoring, full displacement (operating conditions 12-15) is shown in Figure 7.21.

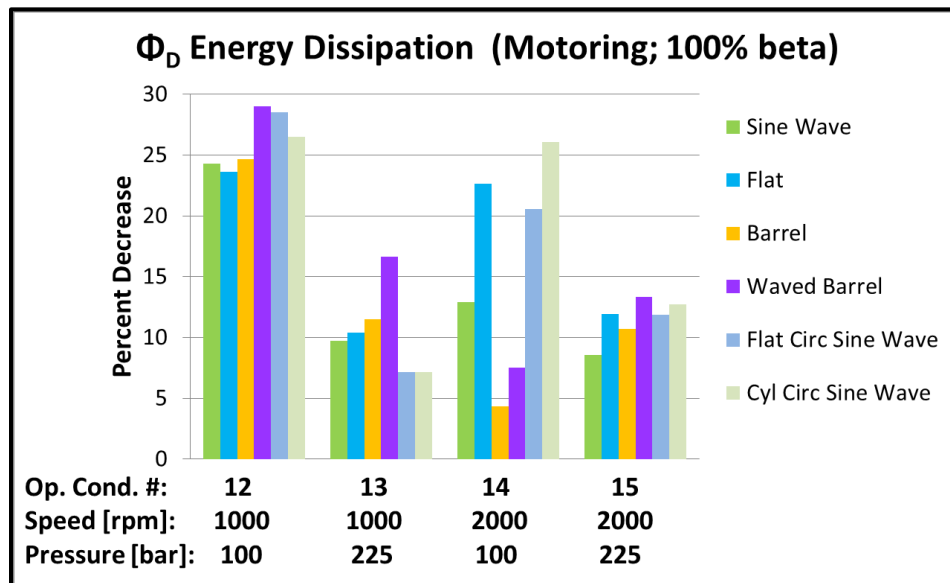


Figure 7.20. Decrease in energy dissipation due to micro-surface shaping of the piston; motoring, full displacement (operating conditions 12-15).

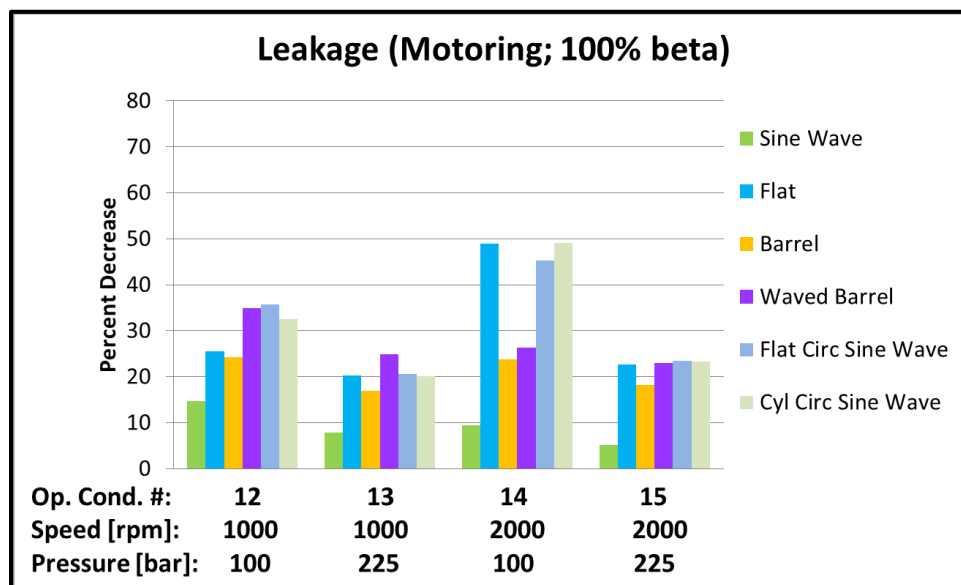


Figure 7.21. Decrease in leakage due to micro-surface shaping of the piston; motoring, full displacement (operating conditions 12-15).

The effect that each surface shape has on the leakage in comparison to the baseline for full displacement motoring mode is shown in Figure 7.21. This decrease can reach up to around 50% for the flat and the circ sine wave surface profiles at 2000 rpm, 100 bar. The waved barrel surface profile results in larger decreases in leakages also in motoring mode among the operating conditions shown. Again, it is the case that the energy dissipation strongly relies on the reduction in leakages while the torque losses seem to have little effect on the overall energy dissipation, as shown in Figure 7.22.

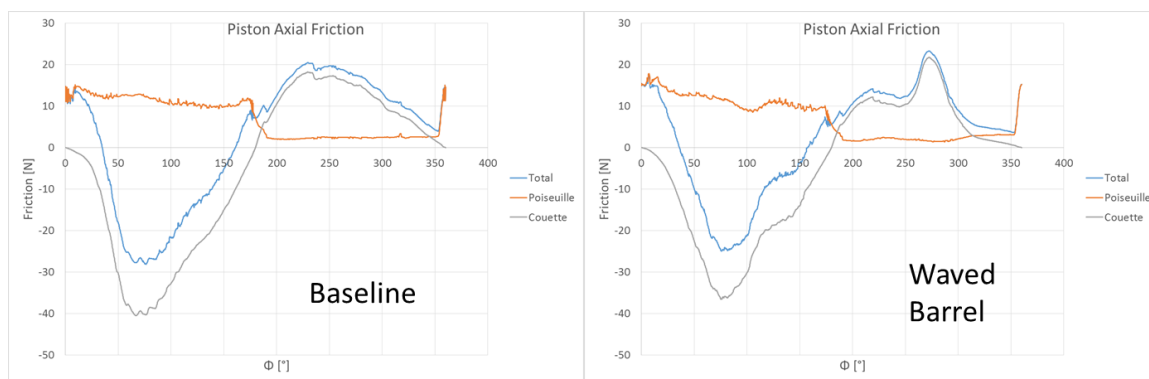


Figure 7.22. Baseline vs. waved barrel piston axial friction, operating condition 15; motoring, 2000 rpm, 225 bar, 100%.

The piston axial friction of the waved barrel surface profile concludes further that the addition of a surface profile in motoring mode does not greatly affect the torque losses as it only slightly decreases the friction forces; the overall decrease in energy dissipation resulting from the decrease in leakage due to the decreased clearance between the piston and the bushing. The deformations of the solid bodies due to the thermal and pressure loading also remain very similar in location with the addition of the waved barrel surface profile, although, the magnitude is again slightly reduced in correspondence with the slightly reduced axial friction forces.

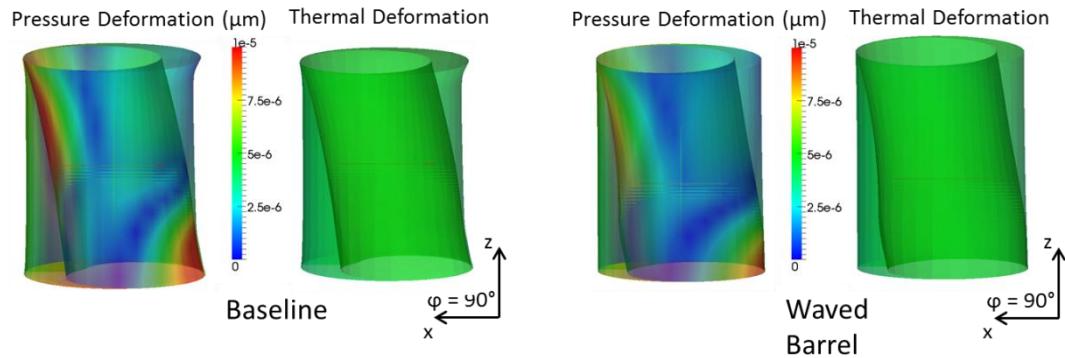


Figure 7.23. Baseline vs. waved barrel deformations, operating condition 15; motoring, 1000 rpm, 225 bar, 100%.

7.4 Conclusion

In conclusion to the investigation of the piston surface shaping, the barrel surface profile appears to be the best in terms of decreasing the energy dissipation from the baseline in reference to all of the operating conditions studied, especially so at the high pressure, high speed, full displacement, pumping operation. If the machine were to be used in just motoring mode, it was shown that the waved barrel actually outperforms the barrel in this mode of operation. As for partial displacement, although the barrel surface profile still performs well, the flat and the circ sine wave profiles perform slightly better. For full displacement, pumping mode, it was shown that the flat surface profile is dependent on the operating speed; at higher speeds the torque losses are greatly increased although the leakage is still reduced due to the reduced clearance. At these operating conditions, the barrel performs much better since the decrease in leakages based on the reduced clearance does not in turn result in greatly increased friction forces. The waved barrel and the circ sine profiles overall reduce the energy dissipation, but are dependent on the operating pressure; performing better at lower pressures. As for the partial displacement and the motoring mode of the machine, the decrease in energy dissipation is strongly reliant on the decrease in leakages.

CHAPTER 8. CONCLUSIONS

The micro-surface shaping of the piston for the piston/cylinder interface is shown through simulation study to improve the efficiency of the machine especially based on the decreased leakages in respect to a reduced clearance, overall improving the performance of the axial piston machine.

A baseline was established first in order to compare the simulated results of the micro-surface shaped piston profiles. Steady-state measurements were taken in order to ensure accurate temperature inputs into the model as well as measured wear profiles on the piston and the cylinder. The model was verified through comparison of simulations results to measurements on the tribo test rig.

An investigation of the various design parameters of the sine wave, the flat, and the barrel surface profiles was conducted. This study revealed that for the sine wave surface profile the best amplitude is the 3 μm amplitude in which the number of waves at this amplitude can vary between 2.5-10.5 waves (in increments of 1) without influencing the fluid film behavior. It was concluded that the number of waves has little effect on the results at smaller amplitudes while increasing the number of waves in conjunction with larger amplitudes increases the effects. As for the leakages, the decrease in leakage is larger the smaller the amplitude.

The investigation of the flat sinusoidal wave surface profile based on the amplitude of the ends concluded that the performance does not strongly depend on this design parameter especially since the clearance between the piston and the cylinder remains the same along the flat gap length of the piston. Although, for the leakage results, there is a slight increase with the increase of the end amplitude due to the larger area for the fluid to flow from the gap.

And finally, a design study for the barrel surface profile showed that for low pressure operating conditions larger radii are best with a left shift while for higher pressure operating conditions, smaller radii are best for a middle shift; speed does not have a large effect on the trends. A compromise between the two was considered where a middle radii is chosen (B6) for a slightly left middle shift (L1). At the higher operating pressure the leakages greatly affect the overall energy dissipation while for the lower pressure operating conditions the torque losses have a larger influence on the energy dissipation.

From the design study, 6 different piston surface profiles were chosen and simulated over a wider range of operating conditions in which the results were then compared. In conclusion to this investigation, if the machine were to be used over a wide range of operating conditions, the barrel surface profile appears to be the best (especially at high operating pressures for full displacement and pumping mode). More specifically, in motoring mode the waved barrel outperforms the barrel while for partial displacements, the the flat and the circ sine wave profiles perform slightly better. For full displacement, pumping mode, it was shown that the flat surface profile performs better at lower speeds in which the leakage overrules the torque losses. The barrel heavily relies on the reduction in leakages over all of the operating conditions since the torque losses are not greatly increasing from the baseline. The waved barrel and the circ sine profiles tend to be more dependent on the operating pressure; performing better at lower pressures. As for the partial displacement and the motoring mode of the machine, the decrease in energy dissipation is strongly reliant on the decrease in leakages.

LIST OF REFERENCES

LIST OF REFERENCES

- Baker, J. (2008). *Power losses in the lubricating gap between cylinder block and valve plate of swash plate type axial piston machines*. Purdue University, MS Thesis.
- Baker, J., & Ivantysynova, M. (2009). Advanced surface design for reducing power losses in axial piston machines. *International Conference on Fluid Power, 10*, pp. 15-30. Linköping, Sweden.
- Baker, J., & Ivantysynova, M. (2009). Power loss in the lubricating gap between cylinder block and valve plate of swash plate type axial piston machines. *International Journal of Fluid Power, 10*(2), 29-43.
- Bergada, J. M., Davies, D. L., Kumar, S., & Watton, J. (2011). The effect of oil pressure and temperature on barrel film thickness and barrel dynamics of an axial piston pump. *Meccanica, 639-654*.
- Bergada, J. M., Watton, J., & Kumar, S. (2008). Pressure, flow, force, and torque between the barrel and port plate in an axial piston pump. *Journal of Dynamic Systems, Measurement, and Control, 011011*.
- Deeken, M. (2003). Simulation of the tribological contacts in an axial piston machine. *O+ P Ölhydraulik und Pneumatik, 47*, 11-12.
- Franco, N. (1961). Pump design by force balance. *Hydraulic and Pneumatic, 14*(11), 101-107.
- Hargreaves, D. J. (1991). Surface waviness effects on the load-carrying capacity of rectangular slider bearings. *Wear, 145*, 137-151.
- Hibbert, G., Lindsay, D. V., Shute, N. A., & Turnbull, D. E. (1971). The balancing of piston and valveplate forces in axial piston pumps and motors. *Technical Report British Hydromechanics Research Association*.
- Huang, C., & Ivantysynova, M. (2003). A new approach to predict the load carrying ability of the gap between valve plate and cylinder block. *Proceedings of the Bath Workshop on Power Transmission and Motion Control PTMC, Bath, UK*, (pp. 225-239).

- Jacazio, G., & Vatta, F. (1981). The block-lift in axial piston hydraulic motors. *Proceedings of the ASME/ASCE Bioengineering, Fluids Engineering and Applied Mechanics Conference*, (pp. 1-7). Boulder, Colorado, USA.
- Jouini, N., & Ivantysynova, M. (2008). Valve plate surface temperature prediction in axial piston machines. *Proceedings of the 5th FPNI PhD Symposium*, (pp. 95-110). Cracow, Poland.
- Kim, J. K., & Jung, J. Y. (2003). Measurement of fluid film thickness on the valve plate in oil hydraulic axial piston pumps (Part I- bearing pad effects). *KSME International Journal*, 17(2), 246-253.
- Kim, J. K., Kim, H. E., & Oh, S. H. (2005). Measurement of fluid film thickness on the valve plate in oil hydraulic axial piston pumps (Part II- spherical design effects). *Journal of Mechanical Science and Technology*, 19(2), 655-663.
- Manring, N. D. (2000). Tipping the cylinder block of an axial piston swash-plate type hydrostatic machine. *Journal of Dynamic Systems Measurements and Control*, 216-221.
- Manring, N. D., Johnson, R. E., & Cheruki, H. P. (2002). The impact of linear deformations on stationary hydrostatic thrust bearings. *Journal of Tribology*, 124(4), 874-877.
- Matsumoto, K., & Ikeya, M. (1991). Friction and leakage characteristics between the valve plate and cylinder for starting and low speed conditions in a swashplate type axial piston motor. *Transactions of the Japan Society of Mechanical Engineers - Part C 57*, 2023-2028.
- Olems, L. (2000). Investigations of the temperature behaviour of the piston cylinder assembly in axial piston pumps. *International Journal of Fluid Power*, 1(1), 27-38.
- Pelosi, M., & Ivantysynova, M. (2011). The influence of pressure and thermal deformation on the piston/cylinder interface film thickness. *Proceedings of the 52nd National Conference on Fluid Power 2011, NCFP III-9.3*.
- Pelosi, M., & Ivantysynova, M. (n.d.). Surface deformation enables high pressure operation of axial piston pumps. *ASME/Bath Symposium on Fluid Power and Motion Control*. Arlington, Virginia, USA.
- Rasheed, H. (1998). Effect of surface waviness of the hydrodynamic lubrication of a plain cylindrical sliding element bearing. *Wear*, 223, 1-6.
- Shin, J. H., & Kim, K. W. (2014). Effect of surface non-flatness on the lubrication characteristics in the valve part of a swash-plate type axial piston pump. *Meccanica*, 49(5), 1275-1295.

- Wieczorek, U., & Ivatysynova, M. (2002). Computer aided optimization of bearing and sealing gaps in hydrostatic machines - the simulation tool CASPAR. *International Journal of Fluid Power*, 3(1), 7-20.
- Yamaguchi, A., Sekine, H., Shimizu, S., & Ishida, S. (1990). Bearing/seal characteristics of the oil film between a valve plate and a cylinder block of axial pumps. *JHPS*, 18(7), 543-550.
- Zecchi, M. (2013). *A novel fluid structure interaction and thermal model to predict the cylinder block/valve plate interface performance in swash plate type axial piston machines*. PhD Thesis, Purdue University.
- Zecchi, M., & Ivatysynova, M. (2012). An investigation of the impact of micro surface shaping on the cylinder block/valve plate interface performance through a novel thermo-elasto-hydrodynamic model. *The 7th FPNI PhD Symposium on Fluid Power*.
- Zecchi, M., & Ivatysynova, M. (2012). Cylinder block/valve plate interface - a novel approach to predict thermal surface loads. *Proceedings of the 8th IFK*. Dresden, Germany.
- Zecchi, M., & Ivatysynova, M. (n.d.). A novel fluid structure interaction model for the cylinder block / valve plate interface of axial piston machines. *Proceedings of the IFPE 2011*. Las Vegas, Nevada, USA.

APPENDICES

Appendix A: Material Properties

The material properties are important to consider in simulation in order to accurately predict results since the material properties directly affect the elastic deformations of the piston and the cylinder which leads to the alteration of the fluid film thickness and simultaneously affects the fluid film surface temperatures and the thermo-elastohydrodynamic fluid film pressure field. The material properties of the piston and bushing that were used in the baseline, steady-state condition measurements and simulations are shown in Table A.A1.

Table A.A1. Material properties.

Steel Piston		
Young's Modulus	2.1e11	Pa
Poisson Ratio	0.29	-
Density	7850	kg/m ³
Thermal Expansion Coefficient	1.3e-5	1/°C
Thermal Conductivity	43	W/mK
Bronze Bushing		
Young's Modulus	1.05e11	Pa
Poisson Ratio	0.34	-
Density	8600	kg/m ³
Thermal Expansion Coefficient	1.8e-5	1/°C
Thermal Conductivity	115	W/mK

Appendix B: Baseline Measurement Results

In this section, the complete set of measured parameters are shown from the baseline, steady-state measurements for all considered operating conditions

Table A.B1. Baseline pumping mode complete measured results – common operating conditions.

Operating Condition - Pumping ($\beta = 100\%$)	1	2	3	4	Unit
High Pressure	125	325	125	325	bar
Low Pressure	25	25	25	25	bar
Leakage Pressure	0.50	0.53	0.55	0.56	bar
Angular Speed	1000	1000	2000	2000	rpm
Case Temperature	50.81	57.10	56.96	64.60	°C
Temperature at High Pressure Port	53.66	56.80	53.43	56.30	°C
Temperature at Low Pressure Port	52.4	52.5	52.2	52.4	°C
Leakage Flow Rate	2.84	3.53	3.59	4.17	l/min
Flow Rate at High Pressure Port	71.00	66.52	145.49	139.39	l/min
Torque	131	371	135	377	Nm
Swash Plate Angle	17	17	17	17	°

Operating Condition - Pumping ($\beta = 20\%$)	5	6	7	8	Unit
High Pressure	125	325	125	325	bar
Low Pressure	25	25	25	25	bar
Leakage Pressure	0.33	0.63	0.38	0.72	bar
Angular Speed	1000	1000	2000	2000	rpm
Case Temperature	60.09	70.87	59.99	68.23	°C
Temperature at High Pressure Port	55.14	64.09	54.75	59.88	°C
Temperature at Low Pressure Port	52.2	52.1	52.3	52.3	°C
Leakage Flow Rate	2.40	5.07	2.63	5.45	l/min
Flow Rate at High Pressure Port	10.69	4.82	25.95	19.19	l/min
Torque	32	79	35	83	Nm
Swash Plate Angle	3.4	3.4	3.4	3.4	°

Table A.B2. Baseline pumping mode complete measured results –
high pressure operating conditions.

Operating Condition - Pumping ($\beta = 100\%$)	9	10	A	11	Unit
High Pressure	425	425	325	425	bar
Low Pressure	25	25	25	25	bar
Leakage Pressure	0.82	0.92	0.69	1.26	bar
Angular Speed	1000	2000	2800	2800	rpm
Case Temperature	70.20	73.00	75.00	76.37	°C
Temperature at High Pressure Port	59.40	58.60	57.29	58.69	°C
Temperature at Low Pressure Port	52.4	52.4	52.5	52.7	°C
Leakage Flow Rate	3.95	4.91	3.54	5.95	l/min
Flow Rate at High Pressure Port	62.37	133.37	194.15	188.74	l/min
Torque	489	495	382	495	Nm
Swash Plate Angle	17	17	17	17	°

Operating Condition - Pumping ($\beta=20\%$)	B	C	D	Unit
High Pressure	425	325	425	bar
Low Pressure	25	25	25	bar
Leakage Pressure	0.69	0.51	0.73	bar
Angular Speed	2000	2800	2800	rpm
Case Temperature	76.24	71.39	76.82	°C
Temperature at High Pressure Port	66.09	61.53	65.80	°C
Temperature at Low Pressure Port	52.4	52.6	52.4	°C
Leakage Flow Rate	10.23	6.76	10.89	l/min
Flow Rate at High Pressure Port	8.73	22.34	15.81	l/min
Torque	90	71	91	Nm
Swash Plate Angle	3.4	3.4	3.4	°

Table A.B3. Baseline motoring mode complete measured results.

Operating Condition - Motoring ($\beta = 100\%$)	12	13	14	15	Unit
High Pressure	150	275	150	275	bar
Low Pressure	50	50	50	50	bar
Leakage Pressure	0.67	0.24	0.21	0.27	bar
Angular Speed	1000	1000	2000	2000	rpm
Case Temperature	55.90	58.69	60.66	65.92	°C
Temperature at High Pressure Port	52.40	52.45	52.20	52.93	°C
Temperature at Low Pressure Port	51.4	50.9	51.4	51.3	°C
Leakage Flow Rate	0.67	1.26	1.19	1.87	l/min
Flow Rate at High Pressure Port	78.80	81.00	154.08	156.70	l/min
Torque	167	310	152	295	Nm
Swash Plate Angle	17	17	17	17	°

Operating Condition - Motoring ($\beta=20\%$)	E	F	G	H	Unit
High Pressure	100	275	100	275	bar
Low Pressure	0.2	25	8.5	50	bar
Angular Speed	1000	1000	2000	2000	rpm
Case Temperature	55.06	61.76	59.00	64.40	°C
Temperature at High Pressure Port	52.35	52.59	52.70	52.23	°C
Temperature at Low Pressure Port	52.2	53.2	52.7	52.2	°C
Leakage Flow Rate	1.39	2.64	2.05	3.13	l/min
Flow Rate at High Pressure Port	19.67	23.47	35.58	40.56	l/min
Torque	17	60	15	59	Nm
Swash Plate Angle	3.4	3.4	3.4	3.4	°

LIST OF PUBLICATIONS

LIST OF PUBLICATIONS

Wundergem, A. and Ivantysynova, M. (2014). The Impact of the Surface Shape of the Piston on Power Losses. *Proceedings of the 8th FPNI Ph.D Symposium on Fluid Power, Lappeenranta, Finland.*